

**UNCLASSIFIED**

**AD 428437**

**DEFENSE DOCUMENTATION CENTER**

**FOR**

**SCIENTIFIC AND TECHNICAL INFORMATION**

**CAMERON STATION, ALEXANDRIA, VIRGINIA**



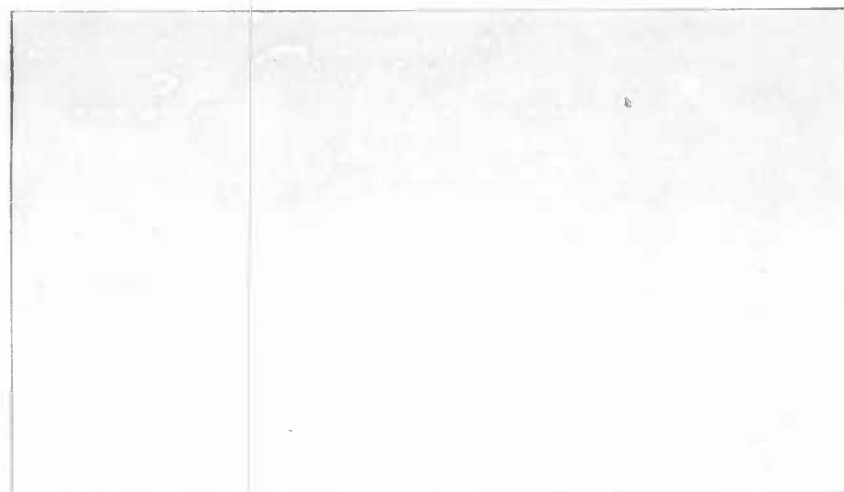
**UNCLASSIFIED**

NOTICE: When government or other drawings, specifications or other data are used for any purpose other than in connection with a definitely related government procurement operation, the U. S. Government thereby incurs no responsibility, nor any obligation whatsoever; and the fact that the Government may have formulated, furnished, or in any way supplied the said drawings, specifications, or other data is not to be regarded by implication or otherwise as in any manner licensing the holder or any other person or corporation, or conveying any rights or permission to manufacture, use or sell any patented invention that may in any way be related thereto.

N-64-8

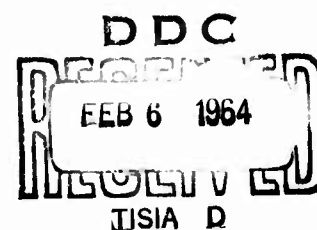
428437

CATALOGED BY DDC  
AS AD No. 428437



RESEARCH

DEVELOPMENT



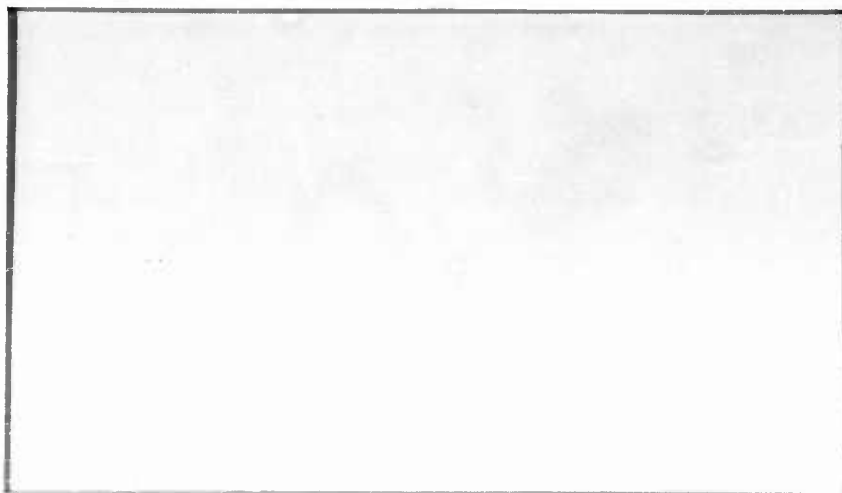
VIDYA

1450 PAGE MILL ROAD, PALO ALTO, CALIFORNIA

A DIVISION OF

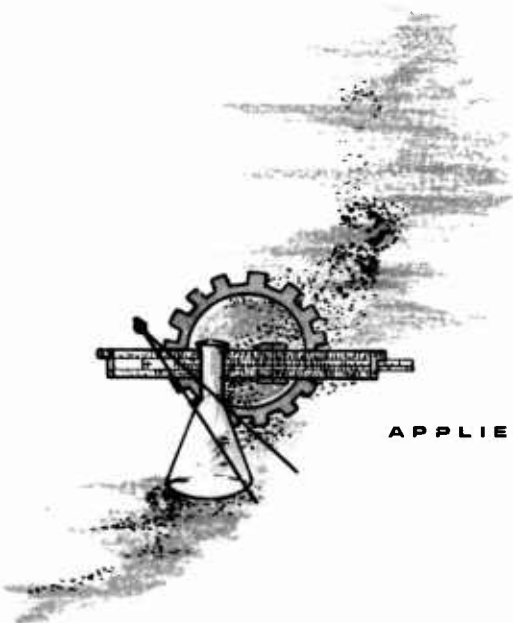
Itek

CORPORATION



# व VIDYA

*The word Vidya, taken from the Vedanta philosophy of the Hindus, means knowledge. The symbol used to denote the Vidya organization is the letter "V" from Sanskrit, the ancient language of India.*



APPLIED MECHANICS....PHYSICS....ANALYSES



**A STUDY OF SOLID-PROPELLANT ROCKET  
MOTOR EXPOSED MATERIALS BEHAVIOR**

Vidya Project No. 9061

**SECOND QUARTERLY PROGRESS REPORT**  
for the period from  
1 September 1963 through 30 November 1963

by

**Peter A. McCuen  
Raymond E. Lundberg  
John W. Schaefer**

for

**AIR FORCE FLIGHT TEST CENTER  
EDWARDS AIR FORCE BASE, CALIFORNIA**

Contract No. AF 04(611)-9073  
Air Force Program Structure No. 750 G  
AFSC Project No. 3059  
AFSC Task Nos. 305907 and 305913

Approved: Robert M. Kendall  
Robert M. Kendall, Head  
Propulsion Section

Approved: Morris W. Rubesin  
Morris W. Rubesin, Head  
Thermodynamics Department



**VIDYA**

A DIVISION OF



CORPORATION

**1450 PAGE MILL ROAD • PALO ALTO, CALIFORNIA**  
**TEL: DAVENPORT 1-2455 TWX: 415 492-9270**

## ACKNOWLEDGMENTS

The authors express their appreciation to the many Vidya staff members and others who have materially contributed to the study. In particular, the efforts of M. W. Rubesin, R. M. Kendall, D. T. Flood, R. W. Higgins, and H. Aroeste are gratefully acknowledged.

## SUMMARY

This report describes the work performed under Contract AF 04(611)-9073 during the second quarter of the contract period, beginning September 1963. The objectives of the study are:

(a) To develop design tools, in the form of digital computer programs, for the nozzle designers to use for calculating the behavior of materials exposed to a solid-propellant rocket-exhaust environment.

(b) To marshall existing theoretical methods, and to extend these or develop new methods where necessary, to gain a better understanding of the fundamental mechanisms associated with exposed materials behavior in a rocket nozzle environment.

The work during this quarter has been directed toward the development of a digital computer program applicable to materials such as tungsten and graphite, that, in general, do not erode appreciably or that erode with one moving boundary. This has required effort in the areas of convective heat transfer, transient conduction, equilibrium chemistry, reaction kinetics, and mass transport, as applied to the solid-propellant rocket problem, and this work is discussed in detail. Further, a plasma-generator rocket simulation-test program has been formulated to complement the theoretical studies, and the test program and some firing results are described.

# TABLE OF CONTENTS

	<u>Page No.</u>
ACKNOWLEDGMENTS	ii
SUMMARY	iii
LIST OF TABLES	vi
LIST OF FIGURES	vii
LIST OF SYMBOLS	ix
1. INTRODUCTION	1
2. THEORETICAL STUDIES	2
2.1 Introduction	2
2.2 Boundary-Layer Transfer Coefficients	3
2.2.1 Nonablating nozzle wall convective heat transfer	4
2.2.1.1 The Ambrok-Rubessin-Mayer method	4
2.2.1.2 Comparison of the Ambrok-Rubessin-Mayer results with experimental data	13
2.3 Surface Chemical Reactions at a Graphite Wall	15
2.3.1 Method of analysis	15
2.3.2 Reaction kinetics	22
2.3.3 Surface recession of a graphite wall	24
2.3.4 Graphite ablation in Mixture 4	29
2.4 Internal Material Thermal Behavior	31
2.4.1 The heat equation with a moving boundary	31
2.4.2 Ablating surface boundary condition	33
2.4.3 Program verification	37
2.4.4 Future effort	38
3. EXPERIMENTAL STUDIES	39
3.1 Introduction	39
3.2 Properties of Test Gas Mixtures	40
3.3 Chemical Erosion Test Program	43
3.3.1 Introduction	43
3.3.2 Program outline	45
3.3.3 Test facility modifications and checkout	46
3.3.4 Test sections	48

	<u>Page No.</u>
3.3.4.1 Calibration nozzles	48
3.3.4.2 Ablative-material nozzles	50
3.3.5 Test results	53
3.3.5.1 Pressure distribution tests	54
3.3.5.2 Chemical erosion test	56
3.4 Particle Impact Test Program	61
REFERENCES	65
TABLES I THROUGH IV	
FIGURES 1 THROUGH 33	
APPENDIX A - DISCUSSION OF A STABILITY CRITERION FOR THE FINITE DIFFERENCE FORMULATION OF THE HEAT EQUATION	
ERRATA TO FIRST QUARTERLY PROGRESS REPORT	
DISTRIBUTION	

## LIST OF TABLES

- 1.- PROPELLANT COMPOSITION AND PRODUCT SPECIES FOR WALL EROSION CALCULATION.
- 2.- CHEMICAL EROSION OF GRAPHITE IN H, C, N, O, AND Cl EXHAUST.
- 3.- COMPOSITION OF TEST GAS MIXTURES. (a) Elemental composition. (b) Molecular composition; temperature, 3500° K; pressure 20 atm. (c) Molecular composition; temperature 3500° K; pressure, 10 atm. (d) Molecular composition; temperature, 2500° K; pressure 10 atm.
- 4.- CHEMICAL EROSION PROGRAM TEST CONDITIONS.

## LIST OF FIGURES

- 1.- Program flow chart.
- 2.- Flow diagram of wall erosion calculation.
- 3.- Flow and instrumentation diagram (from Ref. 8).
- 4.- Measured wall temperature axial distribution, JPL Test 218.
- 5.- Measured wall pressure axial distribution, JPL Test 218.
- 6.- Calculated energy thickness axial distribution.
- 7.- Calculated wall heat flux axial distribution.
- 8.- Comparison of results with experimental data, JPL Test 218.
- 9.- Calculated enthalpy heat-transfer coefficient axial distribution.
- 10.- Calculated Stanton Number axial distribution.
- 11.- Reaction rate data for hydrogen on graphite.
- 12.- Predicted graphite wall erosion in H, C, N, O, and Cl exhaust.
- 13.- Pressure and mass-transfer effects on predicted chemical erosion of graphite in H, C, N, O, and Cl exhaust.
- 14.- Surface temperature for transient heat conduction in a slab.
- 15.- Transient conduction in the hollow cylinder, back-wall insulated,  $r_s/r_o = 0.6$ .
- 16.- Temperature enthalpy variation for test gas mixtures.  
(a) Mixture 1. (b) Mixture 2. (c) Mixture 3. (d) Mixture 4.  
(e) Mixture 5.
- 17.- Master thermodynamic charts for test gas mixtures.  
(a) Mixture 1. (b) Mixture 2. (c) Mixture 3. (d) Mixture 4.  
(e) Mixture 5.
- 18.- Thermodynamic charts for Mixture 3. (a) Isentropic exponent, (b) Molecular weight, (c) Thermodynamic properties.
- 19.- Gas feed and metering systems.
- 20.- Test setup for arc-plasma generator calibration.

- 21.- Comparison of gas enthalpy by energy balance, calorimeter and mass-discharge methods for nitrogen gas.
- 22.- Pressure distribution calibration test setup.
- 23.- Pressure-tap locations in calibration nozzles.
- 24.- Heat-transfer calibration nozzle.
- 25.- Test nozzle - 0.3-inch throat diameter.
- 26.- Thermocouple installation in test nozzle.
- 27.- Thermocouple probe.
- 28.- Thermocouple locations and analytic temperature distributions in test nozzles. (a) Graphite, (b) Silica phenolic. (c) Graphite phenolic.
- 29.- Pressure-distribution test results. (a) 0.3-inch diameter throat, (b) 0.4-inch diameter throat.
- 30.- Pre- and Post-test wall profile; Test No. 795.
- 31.- Surface recession as determined from plenum pressure; Test No. 795. (a) Plenum pressure. (b) Surface recession. (c) Surface-recession rate.
- 32.- Nozzle firing, ATJ Graphite; Test No. 795.
- 33.- Test nozzle after firing, ATJ Graphite; Test No. 795.



# LIST OF SYMBOLS

a	multiplying factor, defined where used
A	flow area
B'	nondimensional blowing rate, $\frac{(\rho v)_w}{\rho_e u_e C_M}$
c	specific heat
$c_p$	specific heat at constant pressure
$C_n$	nozzle coefficient
$C_F$	friction factor defined by $\tau_w = C_F \rho_e u_e^2$
$C_H$	heat-transfer coefficient defined by $q = \rho_e u_e C_H \Delta H$
$C_M$	mass-transfer coefficient defined by $\rho_e u_e C_M \Delta K_j = -\rho D_{jm} \left( \frac{\partial K_j}{\partial y} \right)_w$
D	nozzle diameter
$D_{jm}$	diffusion coefficient of species j through the mixture
$\Delta E$	activation energy change
H	static enthalpy
$H_t$	total enthalpy
$H_r$	recovery enthalpy
h	heat-transfer coefficient defined by $q = h \Delta t$
k	thermal conductivity
$k_f, k_r, k_1, k_2$	reaction rate constants
$K_F$	equilibrium constant

$K_j$	mass fraction of molecular species; in the gas phase
$\tilde{K}_i$	mass fraction of elemental species $i$ in the gas phase
$m$	exponent in the boundary-layer equations, index in difference equations
$\dot{m}_v$	erosion rate of virgin wall material
$M$	molecular weight
$p$	pressure, partial pressure when subscripted
$P$	power
$Pr$	Prandtl number
$q$	heat flux, that is, energy per unit area
$r$	radius, radial coordinate
$r_c$	radius of curvature of nozzle contour
$r_s$	surface radius
$r_o$	back wall radius
$R$	recovery factor, universal gas constant
$Re$	Reynolds number
$s$	number of sites
$S$	entropy
$T$	absolute temperature
$u_e$	velocity at the boundary-layer edge
$u$	velocity component parallel to the surface
$v$	velocity component normal to the surface
$V$	repulsive potential
$\dot{w}_i$	net rate of production of the $i$ th species

$x$	transformed coordinate in the heat equation, coordinate parallel to the surface in the boundary- layer equations
$x_j$	mole fraction of $j$ th species
$y$	coordinate normal to the surface
$z$	axial coordinate in a nozzle
$\alpha$	thermal diffusivity
$\gamma$	isentropic exponent
$\delta$	boundary-layer thickness
$\delta^*$	boundary-layer-displacement thickness
$\Delta$	difference
$\eta$	fraction of covered site
$\zeta$	$\zeta = e^{-(v/RT)}$
$\theta$	time
$\theta$	momentum thickness
$\mu$	absolute viscosity
$\rho$	mass density
$\sigma$	surface recession
$\phi$	enthalpy thickness $\phi = \int_0^\delta \frac{\rho u}{\rho_e u_e} \frac{H_e - H}{H_e - H_w} dy$
$\bar{\phi}$	modified energy thickness $\bar{\phi} = \int_0^\delta \frac{\rho u}{\rho_e u_e} \frac{H_e - H}{H_r - H_w} dy$
$\tau_w$	shearing stress

#### Subscripts

$e$	evaluated at the edge of the boundary layer
$i, j$	identifies species $i$ or $j$

i initial values on boundary-layer parameters  
o evaluated at total or stagnation conditions  
r evaluated at recovery conditions  
v refers to unablated or virgin material  
w evaluated at the wall conditions  
\* evaluated at the nozzle throat

Superscript

\* denotes condensed phase  
' evaluated at reference condition, value at the end of a time step.

## A STUDY OF SOLID-PROPELLANT ROCKET MOTOR EXPOSED MATERIALS BEHAVIOR

### 1. INTRODUCTION

During the past several years, significant theoretical techniques have been developed by various investigators for characterizing many of the complex individual phenomena occurring in the ablation process of solid-propellant rocket wall materials. These techniques have been used to gain a better understanding of ablation phenomena under simplified conditions and to guide, to a certain extent, the design of aft-closures and nozzles. The proven utility of the theoretical approach in this area has made meaningful the possibility of developing an integrated, more general, analytical technique for the design of solid-propellant rocket wall materials and configurations. The need for such a technique is becoming more urgent as motors increase in size, and thus render the traditional cut-and-try approach more costly and time-consuming.

Recognizing this need, the objectives of this study are two-fold:

(1) To develop design tools for the nozzle designer to use for calculating the behavior of materials exposed to a solid-propellant rocket-exhaust environment. These design tools will be in the form of digital computer programs.

(2) To marshal existing theoretical methods, and to extend these or develop new methods where necessary, to gain a better understanding of the fundamental mechanisms associated with exposed materials behavior in a rocket nozzle environment. This second objective is, of course, coupled with the first in that an appreciation of the fundamental ablation mechanisms is required to calculate their effects.

Both theoretical and experimental studies are being conducted to accomplish the objectives of the program. The relations characterizing the ablation process are being formulated largely from theoretical considerations, but also draw on experimental work in

those areas not amenable to theoretical treatment. Existing test data are being used where available, and small-scale laboratory tests are being conducted as a part of this program to provide information in several areas where it is required. The flow chart of Figure 1 indicates how the various areas of investigations are interrelated.

As indicated in Figure 1, the theoretical studies are divided into two major categories, the first having to do with materials that erode with one "moving boundary" such as graphite (nonablating refractories are a special case of this category), and the second with materials such as the reinforced plastics, or composites, whose ablation can be characterized by two moving boundaries. The experimental studies are being carried out in the Vidya 1-megawatt plasma-generator facility; they consist of graphite and composite-nozzle ablation tests and metallic-oxide particle-impaction tests.

During the second quarter of the program, the theoretical effort continued in the following areas: convective heat transfer, thermal behavior of a nonmelting, noncharring nozzle insert, nozzle wall chemical erosion, and reaction kinetics. The accomplishments here are reported in Section 2. The experimental effort during the quarter consisted of facility modification and checkout for the required operating conditions, test section fabrication, calibration firings, and an ATJ graphite nozzle firing. This work is discussed in Section 3.

## 2. THEORETICAL STUDIES

### 2.1 Introduction

For the purpose of classification, all engineering effort on the program that does not directly involve an experimental test program is called "theoretical." This is actually a misnomer, since the effort is based largely on proven physical and mathematical

relations, and is of a very practical and applied nature. That is, the effort is directed toward the construction of a calculation tool for characterizing the phenomena occurring at an ablating nozzle wall. Because many physical relations are needed for this characterization, and because the interactions between them are quite complex, an analysis flow diagram was prepared (Fig. 2) to help clarify the role of each area of study.

Figure 2 is itself necessarily complex, but it is hoped that it will be helpful in placing each phase of the effort discussed herein in proper perspective. The row of boxes at the top of the figure represents the various inputs required to perform nozzle wall erosion calculations; except for the erosion effects of particle impact, none of these specific data are being sought experimentally under the present contract. The program emphasis, rather, is on the "calculation" area of the figure, to provide a technique for determining nozzle erosion rates and wall temperature from the input data.

The work reported in this section is in the areas of transfer coefficients, surface chemical reactions, and internal material behavior. As the reader reviews the work, it is recommended that he refer to Figure 2 occasionally to review the role of each study.

## 2.2 Boundary-Layer Transfer Coefficients

The boundary-layer transfer coefficients required for the calculation of nozzle wall recession rate are those of heat,  $C_H$ , mass,  $C_M$ , and momentum  $C_F$ . These three coefficients are actually interrelated, and their exact determination would follow from a simultaneous solution of the boundary-layer energy, diffusion, and momentum equations. It has become common practice, however, to employ in their determination rather simple approximate relations. Along this line, the approach used herein is to calculate  $C_H$  independently of  $C_M$  and  $C_F$ , then to estimate  $C_M$  from it using the

Chilton-Colburn relation (although the validity of this requires examination for the multi-component boundary-layer situation). The momentum transport coefficient,  $C_F$ , is not required, except when dealing with materials susceptible to mechanical erosion due to wall shear; in these cases, it should be adequate to determine  $C_F$  from  $C_H$  with Reynolds' analogy. Hence, the major effort to date has been in the selection of a technique to calculate  $C_H$ .

#### 2.2.1 Nonablating nozzle wall convective heat transfer

Calculation of the convective heat-transfer coefficient for a nonablating nozzle wall is an important first step in the determination of nozzle ablation characteristics, since this value, after correction for the blowing reduction (a small correction in this case), is an integral part of the wall ablation relations as shown in the First Quarterly Progress Report, Reference 1. A survey discussion of the several convective computational methods was presented in that report, and it was pointed out that the ARM method (after Ambrok, Rubesin, and Mayer) appeared to offer the advantages of reasonable accuracy and simplicity of utilization. During the past quarter the ARM method was compared with experimental data obtained at the Jet Propulsion Laboratory, and the results were indeed encouraging. Although more checks will have to be made (particularly with rocket data) before the method can be given an unqualified recommendation, it appears at this juncture that it is superior to others in common use. Hence, its development is given in detail herein, and a comparison of its results with experimental data is presented.

##### 2.2.1.1 The Ambrok-Rubesin-Mayer Method

The essence of the ARM method is the assumption that the flat-plate relationship between the local boundary-layer energy thickness,  $\phi$ , and the Stanton number,  $C_H$ , is valid also for



flows with a streamwise pressure gradient. This assumption permits solution of the pressure gradient boundary-layer energy integral equation for  $\phi$ , and then employed again, permits calculation of the pressure gradient Stanton number,  $C_H$ , from  $\phi$ . This is explained in greater detail later in the section. For comparative purposes, the alternate approach in most common usage today should also be mentioned. It is the use of the boundary-layer momentum integral equation, wherein the flat-plate relation between momentum thickness,  $\theta$ , and friction factor,  $C_F$ , is assumed, along with two additional assumptions: (1) velocity profile, to permit calculation of the shape factor  $\delta^*/\theta$  (appearing in the momentum equation), and (2) Reynolds analogy, to permit calculation of  $C_H$  from the resulting  $C_F$ .

The historical development of the ARM method is of some interest, inasmuch as it provides some further insight to its validity. To the best of the writer's knowledge, the basis of the idea developed first in this country in the early 1950's when Rubesin (Ref. 2) at the Ames Research Center of the NACA discovered that convective heat-transfer measurements could be correlated quite well with the local boundary-layer energy thickness. Later, at Vidya, Rubesin used this knowledge to derive the present method, and first published it in Reference 3. The application of interest at that time was aerodynamic heating, and it has been in use at Vidya for 3 years for that purpose. Its results have been compared favorably with re-entry body and X-15 convective heating.

Independently, Ambrok suggested the essence of the same technique (Ref. 4), but his paper was not noted by the workers at Vidya until Mayer (Ref. 5) presented an application of it to the rocket-nozzle situation. Since it is felt that the contributions of all three investigators are important, the appellation "ARM" is used for the method herein.

The derivation of the ARM method follows from the integral form of the boundary-layer energy equation (with no blowing):

$$\frac{d\bar{\phi}}{dx} + \frac{\bar{\phi}}{r\rho_e u_e} \frac{d}{dx} (r\rho_e u_e) + \frac{\bar{\phi}}{(H_r - H_w)} \frac{d}{dx} (H_r - H_w) = c_H' \frac{\rho'}{\rho_e} \quad (1)$$

where

$$c_H' \equiv \frac{q_w}{\rho' u_e (H_r - H_w)} \quad (2)$$

and

$$\bar{\phi} \equiv \int_0^\delta \frac{\rho u}{\rho_e u_e} \frac{H_{te} - H_t}{H_r - H_w} dy \quad (3)$$

Note that this latter definition differs from the conventional energy thickness definition in which  $H_t$  is used in place of  $H_r$ ; this modification is required here to prevent an unnatural singularity in the resulting equations in the case of  $H_w = H_{te}$ . The relation between  $\bar{\phi}$  and  $\phi$  is

$$\bar{\phi} = \phi \left( \frac{H_{te} - H_w}{H_r - H_w} \right) \quad (4)$$

The primes in Equations (2) and (3) indicate properties evaluated at the local reference enthalpy, given by the expressions (Refs. 6 and 7)

$$H' = 0.23 H_e + 0.19 H_r + 0.58 H_w \text{ (laminar)} \quad (5)$$

$$H' = 0.36 H_e + 0.19 H_r + 0.45 H_w \text{ (turbulent)} \quad (6)$$

where

$$H_r = H_e + R \frac{u_e^2}{2}$$

and

$$R = (Pr')^{1/2} \quad (\text{laminar}) \quad (7)$$

$$R = (Pr')^{1/3} \quad (\text{turbulent}) \quad (8)$$

The first step in the solution of Equation (1) consists of determining an expression for the right-hand side, that is, the Stanton number. To do this, we find the relation existing between  $\bar{\phi}$  and  $C_H$  in the flat-plate case, and then assume that this relation also holds for the body of revolution in a pressure gradient.

For the flat-plate case the following relations are known to hold:

$$C_H' = \frac{a}{(Pr')^{2/3} \left( \frac{\rho' u_e x}{\mu'} \right)^m} \quad (9)$$

where for laminar flow

$$a = 0.332$$

$$m = 0.5$$

and for turbulent flow in the Reynolds number range of interest for rocket nozzle application

$$a = 0.0296$$

$$m = 0.2$$

Combining Equations (2) and (9), there results for the flat-plate case

$$\frac{q_w}{\rho_e u_e (H_r - H_w)} = \frac{a (\rho')^{1-m} (\mu')^m}{\rho_e u_e^m x^m (Pr')^{2/3}} \quad (10)$$

Now for the flat plate, the energy integral equation (1) reduces to

$$\frac{d\bar{\phi}}{dx} + \frac{\bar{\phi}}{(H_r - H_w)} \frac{d}{dx} (H_r - H_w) = c_H' \frac{\rho'}{\rho_e} \quad (11)$$

and if the wall is nearly isothermal this becomes simply

$$\frac{d\bar{\phi}}{dx} = c_H' \frac{\rho'}{\rho_e} = \frac{q_w}{\rho_e u_e (H_r - H_w)} \quad (12)$$

So a combination of this and Equation (10) yields

$$\frac{d\bar{\phi}}{dx} = \frac{a(\rho'/\rho_e)}{(Pr')^{2/3} \left( \frac{\rho' u_e}{\mu'} \right)^m x^m} \quad (13)$$

for the flat plate. Now, for small axial variations of  $H_w$  in comparison with  $H_r - H_w$ , the terms on the right-hand side of Equation (13), other than  $x^m$ , are independent of  $x$ . Thus, a direction integration is possible.

$$\bar{\phi} - \bar{\phi}_i = \frac{a(\rho'/\rho_e)}{(Pr')^{2/3} \left( \frac{\rho' u_e}{\mu'} \right)^m} \frac{x^{1-m}}{1-m} \Big|_{x_i}^x \quad (14)$$

Since Equation (9) applies only when the boundary layer begins at  $x = 0$ ,

$$\bar{\phi}_i = 0 \text{ when } x_i = 0 \quad (15)$$

Thus,

$$\bar{\phi} = \frac{a(\rho'/\rho_e)}{(Pr')^{2/3} \left( \frac{\rho' u_e}{\mu'} \right)^m} \frac{x^{1-m}}{1-m} \quad (16)$$

Inverting the equation, there results

$$x^m = \left[ \frac{(Pr')^{2/3} \left( \frac{\rho' u_e}{\mu'} \right)^m (1-m) \bar{\phi}}{a(\rho'/\rho_e)} \right]^{\frac{m}{1-m}} \quad (17)$$

Combining Equation (17) with (10) yields an expression for the heat flux term that does not contain  $x$  explicitly.

$$\frac{q_w}{\rho_e u_e (H_r - H_w)} = \left[ \frac{a(\rho'/\rho_e)}{(Pr')^{2/3} \left( \frac{\rho' u_e \bar{\phi}}{\mu'} \right)^m (1-m)^m} \right]^{\frac{1}{1-m}} = c_H' \frac{\rho'}{\rho_e} \quad (18)$$

It is now assumed that Equation (18), which was derived for the case of the flat plate, also holds for the body of revolution in an axial pressure gradient. We are saying that the energy thickness and the heat flux are related in the same manner in the two cases. Thus, combining Equation (18) with (1), there results for the body of revolution:

$$\begin{aligned} \frac{d\bar{\phi}}{dx} + \left[ \frac{1}{r\rho_e u_e} \frac{d}{dx} (r\rho_e u_e) + \frac{1}{(H_r - H_w)} \frac{d}{dx} (H_r - H_w) \right] \bar{\phi} \\ = \left[ \frac{a(\rho'/\rho_e)}{(Pr')^{2/3} \left( \frac{\rho' u_e}{\mu'} \right)^m (1-m)^m} \right]^{\frac{1}{1-m}} \bar{\phi}^{-\frac{m}{1-m}} \quad (19) \end{aligned}$$

Or, rewritten,

$$\frac{d\bar{\phi}}{dx} + \frac{\bar{\phi}}{r\rho_e u_e (H_r - H_w)} \frac{d}{dx} \left[ r\rho_e u_e (H_r - H_w) \right] = \left[ \frac{a(\rho'/\rho_e)}{(Pr')^{2/3} \left( \frac{\rho' u_e}{\mu'} \right)^m (1-m)^m} \right]^{\frac{1}{1-m}} \bar{\phi}^{-\frac{m}{1-m}} \quad (20)$$

This is a first-order differential equation of the Bernoulli type, and can be solved by transforming the dependent variable,  $\bar{\phi}$ .

Let

$$\bar{\phi} = p^{1-m} \quad (21)$$

Then

$$(1-m)p^{-m} \frac{dp}{dx} + \frac{1}{r\rho_e u_e (H_r - H_w)} \frac{d}{dx} \left[ r\rho_e u_e (H_r - H_w) \right] p^{1-m} = gp^{-m} \quad (22)$$

where  $g$  represents the bracketed term on the right-hand side of Equation (20).

Equation (22) then simplifies to

$$dp + \frac{1}{(1-m)r\rho_e u_e (H_r - H_w)} \frac{d}{dx} \left[ r\rho_e u_e (H_r - H_w) \right] p \, dx = \frac{g}{1-m} \, dx \quad (23)$$

The integrating factor for this equation is

$$\begin{aligned} \int_e \frac{1}{(1-m)r\rho_e u_e (H_r - H_w)} d \left[ r\rho_e u_e (H_r - H_w) \right] \\ = e^{\frac{1}{1-m} \ln \left[ r\rho_e u_e (H_r - H_w) \right]} = \left[ r\rho_e u_e (H_r - H_w) \right]^{\frac{1}{1-m}} \end{aligned} \quad (24)$$

Hence, Equation (23) becomes

$$\left[ r \rho_e u_e (H_r - H_w) \right]_{x_i}^{\frac{1}{1-m}} p \left[ \begin{array}{c} x \\ x_i \end{array} \right] = \int_{x_i}^x \frac{q}{1-m} \left[ r \rho_e u_e (H_r - H_w) \right]_{\frac{1}{1-m}} d\lambda \quad (25)$$

where  $\lambda$  is a dummy length variable along the surface. Recalling that

$$\bar{\phi} = p^{1-m}$$

Equation (25) becomes

$$\begin{aligned} & \left[ r \rho_e u_e \bar{\phi} (H_r - H_w) \right]_{\frac{1}{1-m}} - \left[ r \rho_e u_e \bar{\phi} (H_r - H_w) \right]_i^{\frac{1}{1-m}} \\ &= \int_{x_i}^x \left[ \frac{a(\rho'/\rho_e) r \rho_e u_e (H_r - H_w)}{(Pr')^{2/3} \left( \frac{\rho' u_e}{\mu'} \right)^m (1-m)^m} \right]^{\frac{1}{1-m}} \frac{d\lambda}{1-m} \quad (26) \end{aligned}$$

Hence,

$$\begin{aligned} \bar{\phi}^{\frac{1}{1-m}} &= \left\{ \frac{\left[ r \rho_e u_e (H_r - H_w) \right]_i}{r \rho_e u_e (H_r - H_w)} \bar{\phi}_i \right\}^{\frac{1}{1-m}} \\ &+ \frac{1}{\left[ r \rho_e u_e (H_r - H_w) \right]^{\frac{1}{1-m}}} \int_{x_i}^x \left[ \frac{a(\rho'/\rho_e) r \rho_e u_e (H_r - H_w)}{(Pr')^{2/3} \left( \frac{\rho' u_e}{\mu'} \right)^m (1-m)^m} \right]^{\frac{1}{1-m}} \frac{d\lambda}{1-m} \quad (27) \end{aligned}$$

And now Equation (27), in conjunction with Equation (18), is used to calculate the wall convective heat flux or Stanton number on or in an axisymmetric body in compressible flow. The relations are also applicable to two-dimensional flow if  $r$  is replaced by unity throughout. The integral in Equation (27) must be evaluated numerically, but it is a simple quadrature and can be handled quite well with Simpson's rule. The wall temperature must be known before the calculation can proceed, since the reference properties and  $H_w$  are dependent on it. Unfortunately, the wall temperature is often precisely what we are trying to calculate, so an iterative procedure is called for. A trial wall temperature distribution is assumed,  $C_H'$  is calculated, then  $q_w$ , then  $T_w$  (with a wall conduction program), etc. Normally  $C_H'$  is not strongly dependent on  $T_w$ , so convergence is rapid.

Another quantity required to initiate the calculation is  $\bar{\phi}_i$ . If no other information is available for estimating  $\bar{\phi}_i$  in any given application, it is recommended that it be calculated by equating a form of the simple Bartz equation and Equation (18) at the nozzle entrance. The simple Bartz equation form is

$$C_H' = \frac{a \left( \frac{D}{r_c} \right)_*^{0.1}}{\left( \frac{u_e D \rho'}{\mu'} \right)^m (Pr')^{2/3}} \quad (28)$$

Equating Equation (28) with (18), and rearranging, yields

$$\bar{\phi}_i = \frac{a D_i \left( \frac{\rho'}{\rho_e} \right)_i}{\left( \frac{u_e D \rho'}{\mu'} \right)_i^m (1 - m) (Pr')^{2/3} \left( \frac{D}{r_c} \right)_*^{\frac{0.1}{m}}} \quad (29)$$



2.2.1.2 Comparison of the Ambrok-Rubessin-Mayer results with experimental data

The data used to check the ARM method were obtained at the Jet Propulsion Laboratory and are reported in Reference 8. The experimental apparatus used is shown in Figure 3, taken from Reference 8. Air was heated by lean combustion of methanol in a region far removed from the nozzle test section and separated by baffles, screens, and a long duct. The nozzle used has a throat diameter of 1.803 inches, a length of 5.925 inches, a contraction area ratio 7.75 to 1, an expansion area ratio of 2.68 to 1, a convergent half-angle of  $30^\circ$ , and a divergent half-angle of  $15^\circ$ . It was fabricated of 502-type stainless steel, and has embedded thermocouples for measuring local heat flux, and wall static pressure taps. The heat flux is obtained from the temperature drop in the stainless wall during steady state water jacket cooling.

The particular test for which sufficient data was reported to permit comparison was test number 218. In this test the stagnation pressure was 75.2 psia, and the stagnation temperature was  $1518^\circ$  R. The experimental uncertainty in the measured heat fluxes was estimated to be  $\pm 11$  percent at the throat, and possibly larger at other regions.

The nozzle wall axial temperature distribution was reduced from a temperature profile plot given in Reference 8, and is presented here in Figure 4. The measured wall pressure distribution is shown in Figure 5. It differs significantly from that calculated from one-dimensional flow considerations, indicating significant two-dimensional effects in this small nozzle. The measured pressures, and the corresponding velocities (assuming isentropic expansion), were used in the calculations.

The air specific heat at constant pressure varied over the temperature range of interest, so a curve-fit expression was used to relate temperature and enthalpy.

$$H = 14.6 + 0.2122T + 16.93 \times 10^{-6} T^2 - 2668.7 T^{-1}$$

where  $H$  is given in Btu/lb and  $T$  in  $^{\circ}\text{R}$ .

Since the combustion mixture was lean, the Sutherland relation for air was used to calculate the viscosity.

$$\mu = 7.30 \times 10^{-7} \frac{T^{1.5}}{T + 198.6}$$

where  $\mu$  is given in lb/sec-ft and  $T$  in  $^{\circ}\text{R}$ .

Since the boundary-layer displacement thickness at the nozzle entrance,  $\delta_i^*$ , was measured during the JPL tests, this value, rather than Equation (29), was used to estimate  $\bar{\phi}_i$ . The measured value of  $\delta_i^*$  was 0.041 inch, and the tables of Reference 9 lead to an estimated value of  $(\delta^*/\bar{\phi})_i$  of 0.529. Hence

$$\bar{\phi}_i = 0.00645 \text{ ft.}$$

The corresponding value resulting from Equation (29) is 0.00182 ft. The significance of this discrepancy will be discussed after the presentation of computed results.

Equation (27) was solved numerically for several values of  $\bar{\phi}_i$ , including the "best estimate" of 0.00645 ft, and the results are shown in Figure 6. The effect of the kink in the pressure distribution at  $x/L = 0.7$  can clearly be seen. Equation (18) was then used to calculate  $q_w$ , and these results are presented in Figure 7, also for several values of  $\bar{\phi}_i$ . Again, the effect of the pressure kink can be seen. Especially significant is the strong effect of the initial energy thickness,  $\bar{\phi}_i$ .

Figure 8 presents the comparison of the calculated  $q_w$  ( $\bar{\phi}_i = 0.00645 \text{ ft}$ ) with the JPL experimental results. Included on the figure is the heat-flux distribution obtained from the Bartz Equation, (28). It can be seen that the Bartz equation results

are some 40 percent above the ARM results and the experimental data. Figures 9 and 10 show the calculated enthalpy convective heat-transfer coefficient and Stanton number, respectively.

It can be concluded from Figure 8 that for the experimental conditions considered the ARM method does a much better job of predicting the data than does the Bartz equation. However, in view of the great dependence of the ARM results on  $\bar{\phi}_i$ , as shown by Figure 7, the superiority of the method can logically be questioned in cases where  $\bar{\phi}_i$  is unknown. As discussed earlier, when Equation (29) is used to estimate  $\bar{\phi}_i$  for the case at hand, the resulting value is 0.00182 feet rather than 0.00645 feet. This leads to a calculated  $q_w$  about 25 percent above the data (see Figs. 7 and 8).

It is probable that Equation (29) will do a better job of estimating  $\bar{\phi}_i$  in cases where the wall is not as highly cooled (solid rocket nozzles), since the wall cooling increases the energy thickness; however, if this is the case, the Bartz and ARM  $q_w$  results would also be closer together. Thus, an unqualified recommendation of the ARM method will have to await comparison with experimental data taken under various conditions of  $T_o/T_w$ . This will be done during the next quarter.

## 2.3 Surface Chemical Reactions at a Graphite Wall

### 2.3.1 Method of analysis

With a knowledge of the transfer coefficients, we seek to generate the boundary conditions which are needed for the solution of the temperature history of the wall material. Two specific items are sought:

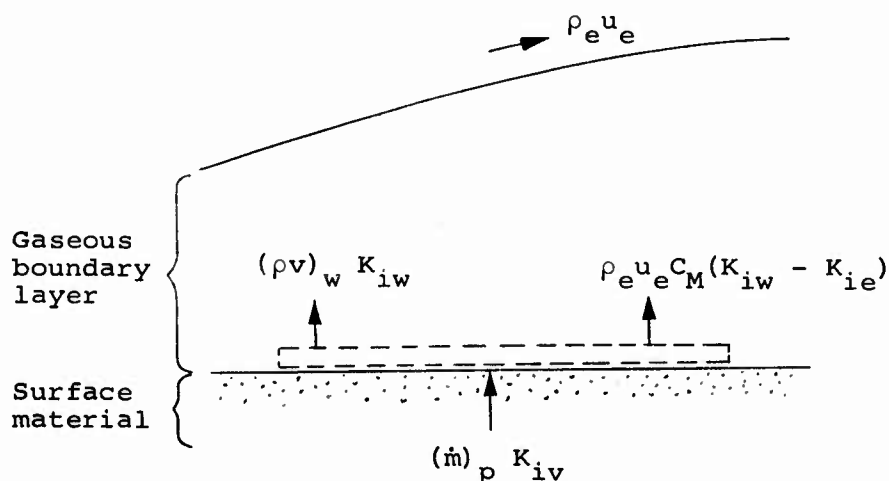
- (1) The net heat flux to the surface.
- (2) The wall erosion rate.

Both these quantities are in general found as a function of wall surface temperature, and thus are not tied down for any specific application until the resulting relations are coupled with the

wall temperature history calculation discussed in Section 2.4. To calculate the first quantity we will need to know the second and the enthalpy of the gas mixture at the surface. The wall erosion rate enters into the energy balance and the gaseous products modify the heat-transfer coefficient. To calculate these we turn to an analysis of the chemical reactions occurring at the exposed surface.

The exposed surface of a nozzle liner material is the scene of intense chemical activity. For example, for a graphite wall in a typical H, C, O, N, Cl exhaust there are about a dozen molecular species which appear in significant quantities during the course of a firing. Hence, there is a large number of chemical reactions which can (and undoubtedly do) occur. The task of analyzing these reactions is further complicated by the fact that not all of them achieve equilibrium under the conditions of interest.

To illustrate the implications of "non-equilibrium" in a flow system which, nevertheless, can be essentially steady state, consider the control volume shown in the following sketch:



The lower boundary of the control volume is taken right at the surface of the material exposed to the exhaust stream. The control volume is presumed to be only infinitesimally thick. Assuming steady state, that is, no mass storage in the control volume, a mass balance for any molecular species can be written as follows:

$$(\rho v)_w K_{iw} + \rho_e u_e C_{M_i} (K_{iw} - K_{ie}) = \dot{m}_v K_{iv} + \dot{w}_i \quad (30)$$

where

$(\rho v)_w$	net convection mass velocity normal to the surface
$K_{iw}$	mass fraction of species $i$ in the surface gas mixture
$C_{M_i}$	mass-transfer coefficient of species $i$ through the mixture
$K_{ie}$	mass fraction of species $i$ on the free stream
$\dot{m}_v$	erosion rate of virgin wall material
$K_{iv}$	mass fraction of species $i$ in the wall material
$\dot{w}_i$	net rate of production of species $i$ due to chemical reactions

The use of the convective mass-transfer term in Equation (30), and in particular the use of the difference in molecular (rather than atomic) concentration as the potential for mass transfer merits some discussion. Strictly speaking, this expression should apply only to a nonreacting boundary layer, and it is not unreasonable here to impose the assumption that the boundary layer is frozen. It may not, however, be necessary to make this assumption. Kulgein (Ref. 27) measured mass-transfer rates for methane with burning in the boundary layer. He found that the wall to stream

partial-pressure difference correlated his results both with and without reaction. Thus, the possibility exists that a less restrictive assumption than that of a frozen boundary layer will still permit Equation (30) to be valid, and this will be explored further during the coming quarter.

The chemical production term in Equation (30) can be eliminated by converting to an elemental mass balance; this is done by summing the mass-balance equations (appropriately weighted) of all the molecular species which contain a given element. The result is a set of equations relating the elemental mass fractions at the wall,  $\tilde{K}_{iw}$ , to the composition of the free stream with the erosion rate and mass-transfer coefficients as parameters.<sup>1</sup> However, in order to relate erosion rate to temperature and pressure, and to enable evaluation of the wall-gas enthalpy, we need to know the molecular composition, that is, the  $K_{iw}$ . To do this we must write Equation (30) for all the species of interest and solve the set of equations simultaneously.

The nature of the chemical production term is best illustrated by a specific example. For the reaction



rate data indicate that the production of  $C_2H_2$  at the surface can be written as

$$\left( \dot{w}_{C_2H_2} \right)_{\text{production}} = k_f p_{H_2} \quad (32)$$

where

$k_f$  reaction rate constant

$p_{H_2}$  partial pressure of  $H_2$  at the surface

---

<sup>1</sup>This is discussed in detail in Reference 1.

If we assume that the reverse reaction can be written as

$$\left( \dot{w}_{C_2H_2} \right)_{\text{consumption}} = k_r P_{C_2H_2}$$

then the definition of equilibrium provides us with

$$k_r = \frac{k_f}{K_p} \quad (33)$$

where  $K_p$  is the equilibrium constant for the reaction given by Equation (31), and is, of course, a function of temperature. Hence, the net production rate is given by

$$\dot{w}_{C_2H_2} = k_f \left( P_{H_2} - \frac{P_{C_2H_2}}{K_p} \right) \quad (34)$$

For a closed system, that is, a system consisting of a mixture in a box, regardless of the value of  $k_f$ , equilibrium is obtained, if one is patient enough, and  $\dot{w}$  vanishes. The control volume shown in the previous sketch is an open system in the sense that mass crosses the boundaries. For such an open system equilibrium is never attained, it is only approached. Further, the approach to equilibrium occurs when the reaction rates are large, that is, when  $k_f \rightarrow \infty$ . As a result of this  $\dot{w}$  remains finite as equilibrium is approached in the open system. In fact,  $\dot{w}$  vanishes only for  $k_f \rightarrow 0$ , that is, when no reactions occur.

To illustrate the behavior of Equation (30) as  $k_f \rightarrow \infty$ , substitute Equation (34) into Equation (30) and rearrange somewhat. We have then<sup>2</sup>

$$p_{H_2} - \frac{p_{C_2H_2}}{K_p} = \frac{\rho_e u_e C_M}{k_f} \left[ \left( K_{C_2H_2} \right)_w - \left( K_{C_2H_2} \right)_e \right] + \frac{(\rho v)_w}{k_f} \left( K_{C_2H_2} \right)_w \quad (35)$$

As  $k_f$  becomes very large the right-hand side of Equation (35) approaches zero, which results in

$$p_{H_2} = \frac{p_{C_2H_2}}{K_p} \quad (36)$$

This is exactly the equilibrium relation between the partial pressures of the species involved in the reaction of Equation (31). Then as the reaction rates become large, the mass-balance equations, Equation (30), reduce to the equilibrium relations among the product species. Notice that this same result will obtain even if the system behaves non-ideally, that is, the order of the reaction is not given by the stoichiometric coefficient.

If sufficient rate data are available the system of equations can be set up and solved. Let us review the steps involved in such a calculation.

(a) Specify problem parameters:

$$T_w, p_w, \rho_e u_e C_{M_i}, \tilde{K}_{ie}, K_{ie}, k_{fi}$$

---

<sup>2</sup>Note that  $\left( K_{C_2H_2} \right)_v \equiv 0$ .



(b) Assume  $(pv)_w$  and calculate  $\tilde{K}_{iw}$  using the elemental mass balance equations resulting from the weighted sums of Equation (30).<sup>3</sup>

(c) Calculate the  $K_{iw}$  using the set of equations resulting from Equation (30), and the expression for conservation of elemental species,

$$\tilde{K}_{iw} = \sum_j \alpha_{ij} K_{jw} \quad (37)$$

where  $\alpha_{ij}$  is the mass fraction of element  $i$  in molecule  $j$ .

Steps (b) and (c) are repeated in an iterative manner until the system closes, that is, until all of the equations resulting from Equation (30) and Equation (37), are satisfied. The result is a unique value for  $(pv)_w$  and since the  $K_{iw}$  are known the wall-gas enthalpy can be calculated.

We have then in principal solved the system and generated the desired boundary conditions for the wall temperature calculation. There are, however, a number of difficulties which merit discussion. They are:

(1) Rate data for many of the reactions of interest are either non-existent or are singularly unreliable.

(2) Even if perfectly reliable data were available the problem involves many parameters and a concise general description of the solutions is not possible.

(3) The mass-transfer coefficients in a reacting system are not well-established experimentally although recent work has shed light on this subject.

Items (1) and (2) will be discussed here, item (3) will be considered in a later report.

---

<sup>3</sup>Details of this step are presented in Reference 1.

### 2.3.2 Reaction kinetics

The determination of reaction rates for heterogeneous reactions, particularly at high temperatures, is at best a difficult task. As temperature is increased, the mixture approaches an equilibrium composition at the reacting surface and becomes rate limited by the transport of reactant to the surface (diffusion control). As can be seen from Equation (35) the degree of approach to equilibrium depends in part on the magnitude of the mass-transfer coefficient. Since the mass-transfer coefficients obtained in rocket nozzles are very high, the onset of diffusion control is delayed and the desired data are in a range unobtainable by most conventional rate experiments. Further difficulties in determination of reaction rates are posed by the fact that the physical character of the reacting surface can have a considerable influence on the reaction rates and that the accurate measurement of surface temperature is difficult, particularly at high temperatures.

The combination of these factors causes what data that do exist to be suspect and often contradictory. An illuminating discussion of existing rate data for the reaction



is given by Scala, Reference 10. In summarizing the data of numerous workers, Scala points out that the order of the reaction is variously reported as lying between zero and one, the activation energy resulting from assuming a standard Arrhenius form varies from 8 to 60 Kcal/mole and the pre-exponential factor varies over several orders of magnitude.

An insidious complication in heterogeneous reactions is the fact that in order to react, a molecule must get to the surface. In a mixture of gases, such as a rocket exhaust, there is competition among the various reacting species and indeed among molecules of the same species for available surface sites. In fact, even an

inert diluent can, if strongly adsorbed, inhibit surface reactions. The net result is that reaction rates in a mixture of gases can be slower than rates measured singly or at very low pressures.

Some methods of correcting for this interaction effect have been summarized by Trapnell (Ref. 11), both for mobile and immobile layers. For example, assuming a mobile layer, that is, one in which the molecules may move easily from site to site, the effect results in a change in activation energy of the reaction given by

$$\Delta E = asV \left\{ 1 - \frac{1 - 2\eta}{[1 - 4(1 - \zeta)\eta(1 - \eta)]^{1/2}} \right\} \quad (39)$$

where

- s     number of neighboring sites
- V     repulsive potential
- $\eta$      fraction of sites covered
- $\zeta$       $e^{-V/RT}$
- a     multiplying factor; unity if the reaction requires two surface sites, one-half if only one is needed

As an upper limit  $\eta \rightarrow 1$ , and with  $s = 4$  and  $a = 1$ , (which would represent a two site reaction on graphite), Equation (39) reduces to

$$\Delta E = 8V$$

As an estimate of this effect, Roberts (Ref. 12) gives  $\Delta E$  as 27 Kcal for the adsorption of hydrogen molecules on tungsten.

A more severe interference with reaction occurs if the surface is wholly covered by species which act as poisons and must be removed before reaction can occur. Following Glasstone, Laidler, and Eyring (Ref. 13), one can express the reaction rate in such a situation as

$$(\dot{w})_f = \frac{k_f p_j}{\sum_{i=j} p_i} \quad (40)$$

where

$(\dot{w})_f$  a uni-directional or forward rate

$p_i$  partial pressures of poisons

$p_j$  partial pressure of reactant

The rate constant  $k_f$  involves a pre-exponential factor that may be estimated theoretically, but the activation energy requires experimental determination.

These considerations indicate further the difficulty in obtaining heterogeneous rate data. One never has pure reactant at the surface, the inhibiting effect of the product species must always be considered, and dissociation at high temperatures may add other molecular species to the mix at the surface.

### 2.3.3 Surface recession of a graphite wall

A series of calculations was performed for a pure graphite wall in a typical exhaust stream excluding, however, all  $Al_2O_3$ . The purpose of these calculations was two-fold, first to assess the contribution of the various surface reactions to the erosion of the wall by chemical reactions, and second, to evaluate the importance of the various parameters affecting the calculation.

In the absence of alumina particles there are three principal combustion products which attack the wall chemically. The basic reactions are (determined from equilibrium chemistry calculations):





It should be noted that reaction, Equation (43), is not the only hydrogen-carbon reaction occurring; a number of hydrocarbon molecules appear in detectable quantities. However, at these temperatures<sup>4</sup>, equilibrium predicts acetylene as the principal constituent.

Reaction (41) was presumed to reach equilibrium; reactions (42) and (43) were handled variously for comparison purposes.

Three different possibilities were considered for the water-gas reaction, Equation (42):

- (1) It proceeds to equilibrium.
- (2) It does not occur.
- (3) It occurs at a finite rate.

As discussed in Reference 1, the rate for the reaction, Equation (42), was obtained by an extrapolation of the data of Binford and Eyring (Ref. 14)<sup>5</sup>. Their data relates to the consumption of  $H_2O$  and hence

$$\dot{w}_{H_2O} = - \left( k_1 p_{H_2O} + k_2 \right) \quad (44)$$

The rate constants  $k_1$  and  $k_2$  were assumed to follow a standard Arrhenius form as follows:

$$k_1 = 19.95 e^{-\left(\frac{2.157 \times 10^4}{T}\right)} \text{ lb/ft}^2\text{-sec-Atmos} \quad (45)$$

$$k_2 = 4.189 \times 10^4 e^{-\left(\frac{4.080 \times 10^4}{T}\right)} \text{ lb/ft}^2\text{-sec} \quad (46)$$

<sup>4</sup>That is, below 3300 K.

<sup>5</sup>More recent data and a new interpretation thereof have been given by Blyholder and Eyring (Ref. 15). This work will be considered in the next quarter.

The same set of possibilities were considered for reaction (43). The rate data were extrapolated from measurements made by the Union Carbide Research Institute (Refs. 16 and 17). An Arrhenius plot of these data is shown as Figure 11. The equation for the forward reaction rate constant was taken as

$$k_f = 4.525 \times 10^8 e^{-\left(\frac{8.12 \times 10^4}{T}\right)} \text{ lb/ft}^2\text{-sec-Atmos} \quad (47)$$

where  $T$  is in  $^{\circ}\text{K}$ . It should be noted that the reliability of the surface temperature measurement (which was a "brightness" temperature measured by a pyrometer) is difficult to assess.

For each of the three possibilities for reactions (42) and (43), comparison calculations were made to obtain the dimensionless wall recession rate

$$B' = \frac{(\rho v)_w}{\rho_e u_e C_M} \quad (48)$$

as a function of wall temperature for the following conditions

$$p = 10 \text{ atmospheres}$$

$$\rho_e u_e C_M = 1 \text{ (and is the same for all species)}$$

$$\left(K_{\text{H}_2\text{O}}\right)_e = 0.1178$$

$$\left(K_{\text{C}_2\text{H}_2}\right)_e = 0$$

The rate constants were calculated from Equations (45), (46), and (47). The effect of the reverse reactions was ignored, however, the forward reaction was constrained so as not to proceed beyond equilibrium. Under this assumption equilibrium is approached more rapidly than it should be. An estimate for the effect of

interaction of competing species was made by increasing the activation energies by 24 Kcal/mole (a change of this order would be indicated for an immobile layer). Because there is some hydrogen dissociation, particularly at the high end of the temperature range considered, the possibility exists that the reaction



proceeds more rapidly than reaction (43). Accordingly, the rate constant for reaction (49) was arbitrarily taken as 10 times that given by Equation (47).

In addition to  $C_2H_2$ , the following hydrocarbon molecules were considered;  $CH_4$ ,  $CH_2$ ,  $C_2H$ ,  $C_3H$ ,  $C_4H$ ,  $C_6H$ ,  $C_4H_2$ , and  $C_3H_2$ . The methane was assumed to be in equilibrium with the graphite and the hydrogen present at the surface (very little methane remains above  $2500^\circ K$  anyway), while the other C-H molecules were assumed to be in equilibrium with graphite and  $C_2H_2$ , thus tying their rate of production to that of acetylene. The latter assumption is somewhat artificial and highly questionable. Incomplete information reported in Reference 17 indicates that the molecular fragments considered may form much more slowly than the rate required to equilibrate with  $C_2H_2$ .

The remaining molecular species were allowed to distribute according to the dictates of chemical equilibrium. The propellant composition and a complete list of product species considered are shown in Table I. These calculations were made by a digital computer program prepared for Vidya's IBM 1620.

Figure 12 is a plot of  $B'$  versus temperature for some of the possible alternative situations. It is readily apparent that rate assumptions regarding just these two reactions can profoundly affect the prediction of wall chemical erosion rate. At  $3000^\circ K$ , for instance, the assumption that neither Equation (42) nor (43) occur, reduces  $B'$  to 1/5 of the value predicted by equilibrium.

If the rate data given here are realistic,  $B'$  is only 0.4 to 0.5 of the value predicted by equilibrium. Thus, it is clear that there is a real need for more complete and carefully acquired fundamental rate data.

Assuming kinetic control of reactions (42) and (43), the rate constants given by Equations (45), (46), and (47), together with the same assumptions made above, a series of calculations was made to study the effects of temperature, pressure, and mass-transfer coefficient. These results are presented as Table II. The evaluation of these results is still in progress, but Figure 13 illustrates the magnitude of the effects which may be encountered. The range of variables considered was as follows:

$$5.0 \leq p \leq 50.0 \text{ (atmospheres)}$$

$$1500 \leq T \leq 3600 \text{ (}^\circ\text{K)}$$

$$0.1 \leq \rho_e u_e C_M \leq 2.0 \text{ (lbs/ft}^2\text{-sec)}$$

At any given temperature both the system pressure and the mass-transfer coefficient can significantly affect  $B'$ . For example, at  $3000^\circ\text{K}$  increasing pressure from 5 to 50 atmospheres increases  $B'$  by about 1/3. At the same temperature an increase in  $\rho_e u_e C_M$  of from 0.1 to 1 decreases  $B'$  by a factor of 2. It should be noted, however, that since  $B'$  contains the factor  $\rho_e u_e C_M$  in the denominator this really represents an increase in wall erosion by a factor of 5.

An effect not illustrated by these calculations is the sensitivity of  $B'$  to  $\left(K_{\text{H}_2\text{O}}\right)_e$ . If the rate of reaction (42) is zero, increasing the mass fraction of water in the free stream from 0.1178 to 0.13 (as can occur with a shift in stream temperature) decreases  $B'$  from 0.027 to 0.016. This reduction occurs because both the oxygen and the hydrogen present in the exhaust



gas as water vapor are prevented from reacting with the wall. This effect is, of course, less pronounced as reaction (42) nears completion, since the amount of remaining water vapor in equilibrium at the wall is small. It is fortunate that if the exhaust stream is in equilibrium (or near it) the value of  $\left(K_{C_2H_2}\right)_e$  is nearly zero, because a similar dependence of  $B'$  on the acetylene fraction exists.

Figure 13 together with the last remarks indicate the difficulty in providing the wall boundary conditions for the conduction solution, in that pressure, the mass-transfer coefficient, and the amount of free stream  $H_2O$  will vary both with position in the nozzle and with time. Two approaches are being explored:

- (1) Include the calculation of the surface chemical reactions as a subroutine to the transient conduction program.
- (2) Develop approximate correlations so that a reasonable table look-up routine can be used.

#### 2.3.4 Graphite ablation in Mixture 4

As discussed in detail in Section 3, the test firings of a graphite nozzle using an  $He, N_2, O_2$  mixture, Mixture 4, have already begun. If we accept the premise of equal mass-transfer coefficients for all species and assume that the reaction (38) achieves equilibrium under the test conditions, the wall erosion rate assumes a particularly simple form.

In the approximate wall temperature range  $2000^\circ K$  to  $3300^\circ K$ , equilibrium predicts that the only significant molecular species at the wall are  $He, N_2$ , and  $CO$  while the main stream contains only  $He, N_2, O_2$ , and  $O$ . Then the oxygen balance can be written as<sup>e</sup>

$$\left(\tilde{K}_O\right)_w = \frac{\left(\tilde{K}_O\right)_e}{1 + B'} \quad (50)$$

and the carbon balance as

---

<sup>e</sup>See Reference 1 for a derivation of this form.

$$\left( \tilde{K}_C \right)_w = \frac{B'}{1 + B'} \quad (51)$$

But since

$$\left( \tilde{K}_C \right)_w = \frac{12}{28} \left( K_{CO} \right)_w$$

and

$$\begin{aligned} \left( \tilde{K}_C \right)_w &= \frac{16}{28} \left( K_{CO} \right)_w \\ \left( \tilde{K}_C \right)_w &= \frac{3}{4} \left( \tilde{K}_O \right)_w = \frac{B'}{1 + B'} \end{aligned} \quad (52)$$

Substituting Equation (52) into (50) and solving yields

$$B' = \frac{3}{4} \left( \tilde{K}_O \right)_e \quad (53)$$

so that in order to estimate the wall recession rate we need only to know the composition of the gas mixture and the local mass-transfer coefficient. It should be emphasized that this expression is for chemical equilibrium with a graphite wall and applies only for Mixture 4 at wall temperatures between  $2000^\circ \text{ K}$  and  $3300^\circ \text{ K}$ . Its simplicity is due to the fact that only the oxygen is chemically reactive in this temperature range. The erosion rate for chemical equilibrium is then essentially independent of wall temperature for this special case.

### 2.3.5 Future effort

An immediate task is to make modifications to the program for calculating the chemical erosion rate of graphite. The effect of reverse reaction will be included. It is also intended to relax the equilibrium assumption for reaction (41). Further consideration

will be given to the phenomena of interaction and poisoning on the surface. In addition, the problem of providing the results of the chemical-erosion calculation in an optimum form for use in the conduction program will be pursued.

Considerable effort will be placed on an analysis of the results of the chemical erosion tests being conducted in the Vidya plasma facility. It may be possible to obtain reaction rate data directly from these tests and they will certainly provide considerable guidance for the selection of data.

The next major task of the program, the analysis of char producing ablators, will begin during the next quarter.

#### 2.4 Internal Material Thermal Behavior

As indicated in Figure 2, the determination of the internal material thermal behavior is an integral part of the overall wall-recession calculation, in that it provides the wall surface temperature input for the surface chemical reaction evaluation. This wall response is calculated with a transient conduction computer program which was discussed in some detail in the First Quarterly Progress Report. Further work on this computer program is presented in this section.

##### 2.4.1 The heat equation with a moving boundary

To facilitate the numerical solution of the heat equation when one boundary surface is receding due to ablation, the equation for conduction of heat, in cylindrical coordinates, can be transformed as follows. If we set

$$x = r - r_s(z, \theta)$$

$$z' = z$$

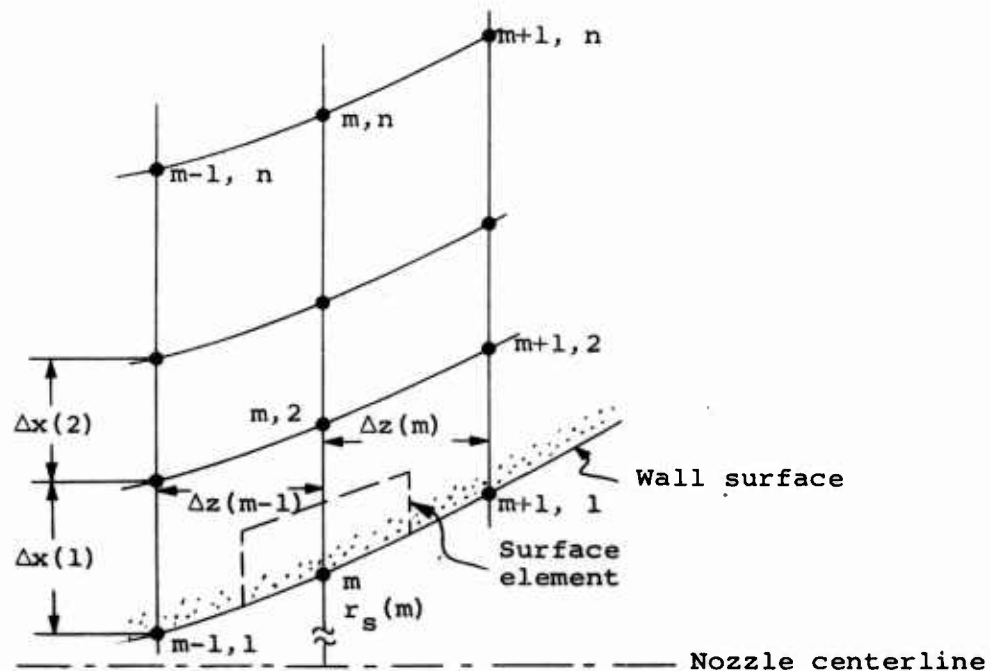
$$\theta' = \theta$$

the heat equation becomes

$$\begin{aligned} \rho c \left[ \frac{\partial T}{\partial \theta} - \left( \frac{\partial r_s}{\partial \theta} \right) \frac{\partial T}{\partial x} \right] = & \frac{\partial}{\partial x} \left( k \frac{\partial T}{\partial x} \right) + \frac{k}{r_s + x} \frac{\partial T}{\partial x} + \frac{\partial}{\partial x} \left( k \frac{\partial T}{\partial z} \right) \\ & + \left( \frac{\partial r_s}{\partial z} \right)^2 \frac{\partial}{\partial x} \left( k \frac{\partial T}{\partial x} \right) - \left( \frac{\partial r_s}{\partial z} \right) \\ & \left[ \frac{\partial}{\partial x} \left( k \frac{\partial T}{\partial z} \right) + \frac{\partial}{\partial z} \left( k \frac{\partial T}{\partial x} \right) \right] - \left( \frac{\partial^2 r_s}{\partial z^2} \right) k \frac{\partial T}{\partial x} \end{aligned} \quad (54)$$

The motives for the selection of this form are discussed in detail in Reference 1.

For computation, the various derivatives appearing in Equation (54) are expressed in finite difference form. The nodal network is illustrated in the following sketch.



Since the problem is axisymmetric, the wall section shown is actually a section of a body of revolution. The coordinate system used poses some restrictions on the placement of nodes. A row of nodes always appears on the surface.  $\Delta z(m)$  can be unequal to  $\Delta z(m-1)$  but  $\Delta z(m)$  is a constant for all  $n$ . Similarly  $\Delta x(n)$  need not equal  $\Delta x(n-1)$  but  $\Delta x(n)$  is a constant for all  $n$ .

The particular finite difference forms of the various derivatives in Equation (54) are lengthy and are not included in this report.

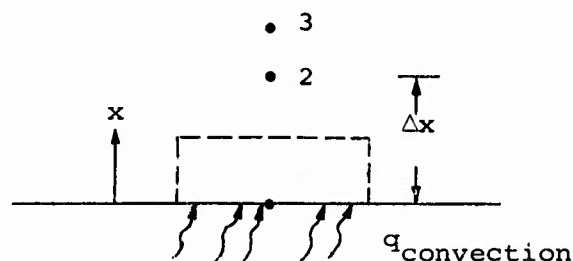
As discussed in Reference 1, the formulation of the difference equation representing Equation (54) can be either explicit or implicit. The program for the solution of Equation (54) utilizing the explicit formulation has been completed and checked out.

#### 2.4.2 Ablating surface boundary condition

The temperatures for nodes not located on (or near) a boundary are calculated from the difference equation representing Equation (54). Special considerations are required for those points located at the ablation surface and there is some latitude in the method used to calculate surface temperatures. Two different methods can be used: (a) heat-flux balance at the surface, (b) energy quantity balance on a finite region surrounding a surface node.

To develop some quantitative experience for the relative merits of the two methods, the one-dimensional heat conduction equation was programmed in finite difference form utilizing a simple convective (constant  $h$ ) boundary condition and constant material properties. A further objective in constructing the simple program was to permit an evaluation of the size of the finite difference net required to provide a good approximation to the differential equation.

Referring to the representation of the one dimensional geometry shown below,



the boundary condition given by the heat-flux balance takes the form

$$q_{\text{convection}} = h(T_a - T_1) = -k \left( \frac{\partial T}{\partial x} \right)_{x=0} \quad (55)$$

If the temperature gradient at the surface is obtained from Taylor's series expansions from which the second derivative terms have been eliminated, one obtains the finite difference form:

$$h(T_a - T_1) = \Delta x \left( \frac{3}{2} T_1 + \frac{T_3}{2} - 2T_2 \right) \quad (56)$$

which may be solved for  $T_1$  directly.

The alternative form results from an energy balance on the dashed box shown in the above sketch. We have then

$$\rho c \frac{\Delta x}{2} \frac{\partial T}{\partial \theta} = q_{\text{convection}} + k \left( \frac{\partial T}{\partial x} \right)_{x=\frac{\Delta x}{2}} \quad (57)$$

Again, if one obtains  $(\partial T / \partial x)$  from Taylor's series expansions, and eliminates the second order terms, there results

$$\rho c \frac{\Delta x}{2} \frac{T_1' - T_1}{\Delta \theta} = h(T_a - T_1) + k \frac{(T_2 - T_1)}{\Delta x} \quad (58)$$

where the prime denotes temperature at the end of the time interval,  $\Delta\theta$ .

Since the form given by Equation (56) does not contain a term relating to energy storage it is a relationship that applies at any instant in time. Then, after the calculation of the "new" temperatures for all the interior points, Equation (56) can be written in terms of the end of time interval values,  $T_1'$ ,  $T_2'$ , and  $T_3'$  and solved for  $T_1'$  directly.

For the more general convective-boundary condition, the net convection heat-flux is written in terms of enthalpy driving potentials and contains a correction due to surface off-gassing. In this case, an iterative procedure will be required to solve for  $T_1'$  and it becomes sensible to consider the use of  $T_1$  on the left-hand side of Equation (55) while retaining  $T_1'$  on the right. This simplification, however, again raises the problem of "stability" of the finite difference form. This is best illustrated by carrying out this simplification as follows. The expression for  $T_1'$  becomes:

$$\frac{k}{\Delta x} \frac{3}{2} T_1' = h(T_a - T_1) + \frac{k}{\Delta x} \left( 2T_2' - \frac{T_3'}{2} \right) \quad (59)$$

If the explicit expression for  $T_2'$  is substituted into Equation (59), we have

$$\begin{aligned} \frac{3}{2} \frac{k}{\Delta x} T_1' = hT_a + \left( \frac{2\alpha\Delta\theta k}{\Delta x^3} - h \right) T_1 + \frac{2k}{\Delta x} \left[ \frac{\alpha\Delta\theta}{\Delta x^2} T_3 + \left( 1 - \frac{2\alpha\Delta\theta}{\Delta x^2} \right) T_2 \right] \\ - \frac{k}{\Delta x} \frac{T_3'}{2} \end{aligned} \quad (59a)$$

The general condition of stability requires that the coefficient on  $T_1$  appearing in Equation (59a) must be positive (see Appendix A). Thus, the inequality

$$\frac{\alpha \Delta \theta k}{\Delta x^3 h} > \frac{1}{2} \quad (60)$$

must be satisfied to yield a meaningful solution for surface temperature. It is further evident that if the convection heat-flux term is written in terms of  $T_1'$ , Equation (56) is unconditionally stable for all values of  $\Delta \theta$  and  $\Delta x$  because the term containing  $\Delta \theta$  and  $T_1'$  which enters via  $T_2'$  is positive. Trial solutions in which the condition given by (60) was violated were attempted and did, in fact, prove troublesome.

A similar decision with regard to the application of Equation (58) must be made. If the formulation is explicit (that is,  $T_1'$  appears only on the left-hand side of (58)), then we have the familiar condition that

$$\frac{\alpha \Delta \theta}{\Delta x^2} \left[ 1 + \frac{h}{(k/\Delta k)} \right] < \frac{1}{2} \quad (61)$$

while the implicit expression is, again, unconditionally stable.

Figure 14 is a comparison of the calculated surface temperatures resulting from the finite difference scheme for each of the two boundary conditions (56) and (58), (using, in both cases, the stable forms) with the values given by the analytical solution. Both methods give results somewhat in error near the beginning of the problem and both seem to approach the correct solution at about the same time (for comparable difference mesh size). An examination of Equation (56) reveals the fact that at the end of the first time-step the same result is obtained regardless of the value of  $\Delta \theta$ . Hence, reducing the size of  $\Delta \theta$  may make the solution worse for short times. Equation (58) does not have this disadvantage in that reducing  $\Delta \theta$  always brings one closer to the correct solution. On this basis, Equation (58) has been used in setting up the axisymmetric program, but the situation is not completely settled.



In order to derive the form equivalent to Equation (58) for the transformed axisymmetric coordinate system, we must include the extra terms resulting in the skewed and moving system. An energy balance on the surface element shown in the sketch on page 32, yields (assuming  $\Delta x$  and  $\Delta z$  to be differentials):

$$\begin{aligned} & \left(1 + \frac{dx}{2r_s}\right) \left\{ K \left( \frac{\partial T}{\partial x} \right) + \frac{\partial r_s}{\partial \theta} \rho c T - \left( \frac{\partial r_s}{\partial z} \right) K \left[ \left( \frac{\partial T}{\partial z} \right) - \frac{\partial r_s}{\partial z} \left( \frac{\partial T}{\partial x} \right) \right] \right\}_{x=\frac{dx}{2}} \\ & + \frac{dx}{2} \left[ \frac{\partial}{\partial z} \left( K \frac{\partial T}{\partial z} \right) - \left( \frac{\partial^2 r_s}{\partial z^2} \right) K \left( \frac{\partial T}{\partial x} \right) - \frac{\partial r_s}{\partial z} \frac{\partial}{\partial z} \left( K \frac{\partial T}{\partial x} \right) \right] \\ & = \rho c \left( \frac{dx}{2} \right) \frac{\partial T}{\partial \theta} + \rho c \frac{\partial r_s}{\partial \theta} \left( \frac{dx}{2r_s} \right) T - q_{net} \sqrt{1 + \left( \frac{\partial r_s}{\partial z} \right)^2} \quad (62) \end{aligned}$$

where the terms inside the braces are understood to be evaluated at  $x = dx/2$  rather than at the surface.

#### 2.4.3 Program verification

Equation (54) together with the boundary condition expressed by Equation (62) have been programed in an explicit difference formulation. To verify the internal logic, this program was used to solve the problem of the hollow cylinder (in the absence of ablation) having constant properties and a simple convective boundary condition. The results of the numerical solution are compared with the analytical solution, taken from Schneider (Ref. 18), in Figure 15. As can be seen, the comparison is very favorable. The problem parameters were:

$$\Delta x = 0.00833 \text{ feet}$$

$$\Delta = 0.1 \text{ sec}$$

$$r_s = 0.125 \text{ feet}$$

$$r_b = 0.20833 \text{ feet}$$

$$\left. \begin{aligned} h &= 0.36 \text{ Btu/ft}^2\text{-sec-}^\circ\text{R} \\ k &= 0.0075 \text{ Btu/ft-sec-}^\circ\text{R} \\ \rho c &= 59.8 \text{ Btu/ft}^3\text{-}^\circ\text{R} \end{aligned} \right\} \text{ typical of graphite}$$

After one second of problem time, the surface temperatures are within 1 percent of the correct values.

The next step in program checkout is the construction of an ablating wall solution from the non-ablating wall solution. This is done as follows. Once the complete solution of the non-moving wall problem is at hand, any arbitrary surface recession rate can be specified. Then, since the position of the surface as a function of time is known, the temperature of the surface can be specified as that temperature which existed at that position at that time in the non-ablating body. As a result of this, the portion of the body which remains must respond exactly as if no ablation had occurred and, for example, the back wall temperatures must be identical in the two cases. This comparison test is still in progress.

#### 2.4.4 Future effort

The most immediate task is the ablating wall comparison just discussed. The addition of the more general boundary conditions is the next following task. These two items would complete the transient temperature package in its explicit formulation.

Because of the mixed derivative terms appearing in the transformed heat equation, Equation (54), the finite difference expression for the temperature at any nodal point  $m, n$  involves the array of temperatures existing at the point  $m, n$  and the eight surrounding points. In preparing the coefficient matrix for the implicit solution, the existence of nine non-zero coefficients in each row results in some additional complexity, for example, the dominant terms must be located and moved to the diagonal. Efforts to overcome these difficulties look hopeful and the implicit formulation will be continued.

The internal behavior of a charring ablator is characterized by two moving boundaries. The analysis of these types of materials will be started in the next quarter.

### 3. EXPERIMENTAL STUDIES

#### 3.1 Introduction

The choice of a rocket-nozzle liner material requires a knowledge of the behavior of appropriate materials in the combustion product environment. This knowledge must be supplied by both an analytic treatment of the materials response and experimental materials testing. As indicated in Figure 2, the analytic treatment requires appropriate input of basic data for a successful and accurate solution, and some of this input must be determined experimentally. Hence, in the experimental phase of this program, several areas in which data are currently lacking are being investigated. These areas include chemical reactions and particle impact as they affect ablation. The experimental effort is conveniently divided into two separate programs:

- (1) The chemical erosion program; the investigation of chemical effects in the ablation process and the development of a simple materials testing technique.

- (2) The particle impact program; the investigation of the effects of particle impingement on ablation.

As indicated above, a secondary purpose of the chemical erosion program is to investigate a relatively simple materials testing technique. The usual materials testing techniques have taken three general forms: full-scale rocket tests, small-scale rocket tests, and splash tests on materials samples. The last technique must be regarded as only qualitative since only a rough comparison between the performance of different materials is possible. With the advent of large rocket motors, full-scale rocket tests for materials evaluation become prohibitive. Small-scale rocket tests do not permit the flexibility of varying test

parameters independently and are also relatively expensive. A flexible, inexpensive yet quantitative experimental materials evaluation technique is therefore desirable, and its development is the subject of one part of the experimental effort.

The presentation which follows covers the areas of experimental activity during the second quarter of the project. The properties of the gas mixtures being used in both programs were calculated, and the results are given in tabular and graphical form. Progress on the chemical erosion program is discussed in detail; this includes plasma generator facility modification, test section fabrication, and several firings. The particle impact program is still in the planning stage, and the status of these plans is presented.

### 3.2 Properties of Test Gas Mixtures

The chemical erosion test program, the experimental investigation of specific chemical reactions as they affect the erosion of nozzle wall materials, requires a series of gas mixtures that will "isolate" the chemical reactions of interest and, for direct application to rocket technology, that will also simulate the solid-propellant rocket environment. The requirements for satisfying these conditions were developed and discussed in Reference 1. In summary, these requirements were the duplication of the temperature-enthalpy variation of the rocket exhaust gases, duplication of the mass fractions of the chemically reactive species of interest, and duplication of the heat, mass, and momentum fluxes at the surface of the ablating material.

Five gas mixtures were selected for the investigation and are summarized below:

- (1) The actual combustion products (with no aluminum compounds).
- (2) The combustion products composition except for hydrogen chloride which is replaced by an inert gas.

(3) The mass fractions of hydrogen and oxygen in the actual products that are capable of reacting with nozzle wall materials and appropriate amounts of inert gases (the hydrogen and oxygen tied up in HCl and CO, respectively, are essentially inert).

(4) The mass fraction of oxygen that is capable of reacting with nozzle wall materials and appropriate amounts of inert gases (the oxygen tied up in CO is essentially inert).

(5) All inert gases.

In order to set test conditions and evaluate test data, the thermodynamic properties and composition of the test gas mixtures must be known for the complete range of test conditions. Estimates of the elemental composition and thermodynamic properties were presented in Reference 1. During this report period, detailed calculations of thermodynamic properties and molecular composition were made for each gas mixture from computer programs developed for the Vidya IBM 1620 computer. Calculations were performed for a complete net of points to allow construction of thermodynamic property charts. The data calculated at each temperature and pressure were enthalpy, entropy, frozen specific heat, equilibrium specific heat, isentropic exponent, molecular weight, mole fractions, and mass fractions.

The elemental and molecular compositions at selected temperatures and pressures are presented in Table III for each gas mixture in terms of the mole and mass fractions. In Mixtures 2 and 3, the original estimates of elemental composition (Ref. 1) were changed somewhat to yield better agreement in the temperature-enthalpy variation and to reduce the experimental complexity of operating with these mixtures. In Mixture 2, nitrogen was used as the inert instead of argon as originally anticipated. In Mixture 3, helium was eliminated, leaving only nitrogen as the inert. Each mixture and its relation to the others is discussed in a following section.

The temperature-enthalpy variation for each gas mixture is presented in Figures 16(a) through (e). The variation for Mixture 1 is included in each figure for comparison; this mixture is the actual products of combustion for a typical solid propellant (with no aluminum compounds). In each case the enthalpy base was arbitrarily assigned as  $H = 0$  at  $2500^{\circ}$  K and 20 atmospheres to facilitate comparison. As shown in the figures, the agreement of Mixtures 2 and 3 with Mixture 1 is excellent. The agreement is good for Mixture 4 which departs somewhat at both high and low temperatures. Mixture 5 disagrees substantially at higher temperatures, above about  $3200^{\circ}$  K. This is due to the essentially constant specific heat caused by the absence of chemical reaction. The only reaction possible, the dissociation of nitrogen, does not occur to any significant degree in the temperature range of interest.

For convenience in data reduction and in setting arc-plasma generator operating conditions, thermodynamic property charts were prepared for each gas mixture. Master charts covering the entire range of temperature and pressure were made; these are presented in Figures 17(a) through (e). Plots of molecular weight and isentropic exponent and charts magnifying the primary area of interest on the master charts were also made for each gas mixture. An example of these plots, for Mixture 3, is presented in Figures 18(a) through (c) (the master chart for Mixture 3 is Fig. 17(c)).

Transport property data are also required for the calculation of heat-transfer parameters. Estimates have been made for the particular gas mixtures of interest from the available data on the individual gases which make up the mixtures (e.g., Ref. 19). A computer program capable of calculating transport properties for multicomponent gas mixtures will also be available shortly.

The utilization of and information obtainable from the five gas mixtures will be discussed in the following section, Chemical Erosion Test Program. One or more of these gas mixtures will also be utilized in the Particle Impact Program which is discussed in Section 3.4.

### 3.3 Chemical Erosion Test Program

#### 3.3.1 Introduction

The primary objective of the chemical erosion test program is the determination of the effects of specific chemical reactions on the erosion of rocket materials. The results obtained, in addition to being of general importance will provide necessary guidance to the theoretical phase of the subject contract. A secondary objective is the definition of an inexpensive technique for the quantitative, as opposed to qualitative, evaluation of candidate materials for rocket nozzles. The technique is expected to be a powerful tool for the material fabricator and the nozzle designer.

The program, in brief, consists of an appropriate series of tests on ablative materials utilizing the five gas mixtures discussed in the previous section. The Vidya arc plasma generator supplies the energy input to the gas mixtures for simulation of the rocket environment. The test materials are graphite, silica phenolic, and graphite phenolic. An axisymmetric nozzle configuration is used for all tests. The heat transfer and pressure distribution for a nonablating wall of the same geometry as the test nozzle is determined with sets of heat-transfer calibration nozzles and pressure distribution calibration nozzles.

In order to increase the effectiveness of the chemical erosion program, the originally proposed program has been extended somewhat. This was a result of the analytical work conducted early in the program in which it was found that wall recession rates are affected in a major way by several chemical reactions. The number of test gases was therefore increased from three to

five, the test configuration was changed from mostly channel tests to all nozzle tests, and the total number of tests was increased from 36 to 56. Channel tests were eliminated because of the edge effects that occur at the side walls of the channel and because of the "gouging" which occurs in the test material at the junction between the test material section and the water-cooled inlet transition section. Also, the nozzle configuration is directly compatible with the axisymmetric computer program being developed.

The activities during the report period that were directly related to the chemical erosion program included the following:

- (1) Calculation of the thermodynamic properties and composition of the test gas mixtures.
- (2) Completion of the necessary test facility changes and additions.
- (3) Checkout of arc-plasma generator operation with the test gas mixtures, particularly Mixtures 4 and 5.
- (4) Fabrication of the pressure distribution calibration nozzles.
- (5) Redesign and fabrication of the heat-transfer calibration nozzles.
- (6) Procurement of graphite and silica phenolic nozzle test section materials.
- (7) Fabrication of six graphite nozzle test sections.
- (8) Determination of thermocouple instrumentation technique for the test nozzles.
- (9) Performance of a pressure distribution calibration test series.
- (10) Performance of a graphite nozzle firing.

The Vidya sponsored calibration of the arc-plasma generator was also completed during the report period. These activities are discussed in following sections.

The originally anticipated testing schedule for the report period was not met because of the delay in completing the facility



calibration, the time required to effect the necessary changes and additions to the facility, and problems in achieving the desired arc-plasma generator operating conditions. These difficulties, discussed in a following section, were resolved late in the period and testing was begun. Pressure distribution tests were run with Mixtures 4 and 5 and a graphite nozzle firing was performed with Mixture 4. The results of these tests are presented in a following section. The chemical-erosion program testing will be completed during the next quarter.

### 3.3.2 Program outline

The program test matrix is presented in Table IV. The test variables are the test gas mixture, the test section material, and the operating (plenum) conditions. The variation of plenum pressure is accomplished by changing the nozzle throat diameter. A complete set of tests is not run with Mixture 1 since little or no difference is anticipated between it and Mixture 2 and because of the hydrogen chloride in Mixture 1 presents a hazard to both equipment and personnel. Three total temperatures are considered since chemical reaction rates are strongly dependent on temperature. The emphasis is on  $3500^{\circ}$  K, however, since this is the approximate total temperature for burning of many solid propellants. Since reaction rates are somewhat pressure-dependent, four tests at moderate pressure, 175 psia, are being run. The majority of tests are being run at 300 psia initial plenum pressure, however. This value was chosen as the upper limit for testing in order to avoid an unreasonably small nozzle throat diameter and because high pressure aggravates the electrode oxidation problem. The test section throat diameter for the 300 psia test condition is 0.3 inch and for 175 psia, 0.4 inch. For each gas mixture except Mixture 1, two tests are conducted at one test point - graphite,  $3500^{\circ}$  K, and 300 psia - to check reproducibility. Seven tests have been left open to allow

addition of conditions found desirable from the other tests and to allow rechecks of other results as necessary.

The chemical reaction information obtainable from the test program may be discussed conveniently by referring to the molecular compositions of Table III. The influence of hydrogen chloride on the wall material erosion is obtainable from comparison of results from Mixtures 1 and 2. As mentioned previously, HCl is expected to act as an inert with the wall materials. In going from Mixture 2 to Mixture 3, the carbon compounds, CO and CO<sub>2</sub>, are eliminated. The effect of their removal on wall erosion is assessed here. The major change is that the available oxygen in the form of CO<sub>2</sub> in Mixture 2 is found in the form of water in Mixture 3. The CO is expected to act as an inert and therefore its removal may not have an affect on the wall erosion.

In going from Mixture 3 to Mixture 4, hydrogen is eliminated. The oxygen is in the form of O<sub>2</sub>, O, and NO rather than as mostly H<sub>2</sub>O as in Mixture 3. This shift in the form of oxygen and the possible affect of atomic hydrogen recombination on the corrosion of the wall material will be studied here. Mixture 5 will serve to determine the ablation in the absence of chemical reaction with the free stream. In this case, the mechanical properties and thermal degradation characteristics of the material will determine the surface recession.

### 3.3.3 Test facility modifications and checkout

A number of changes and additions to the plasma generator facility were required to accommodate the chemical erosion test program. These modifications were primarily associated with the large number of gases being used and the safety and operating problems associated with some of them. Separate gas feed and metering systems were built for hydrogen, carbon dioxide, and hydrogen chloride, which must be introduced into the plasma generator separately. Another system was built for the mixtures of the

other gases that are to be introduced as the primary plasma-generator gas. A schematic of the gas system is presented in Figure 19. The necessary safety precautions were observed in building up each system. A gas collection and exhaust system was also installed close to the exit of the plasma generator to evacuate the sometimes toxic and explosive exhaust gases from the laboratory.

An electrically heated water bath was constructed to heat the condensable gases ( $\text{CO}_2$  and  $\text{HCl}$ ) in order to eliminate severe gas bottle-pressure drops and condensation problems when drawing from these bottles. A temperature of approximately  $110^\circ \text{F}$  is maintained in the bath.

Checkout tests were run on the arc-plasma generator to determine the operating characteristics and conditions for the gases of interest. Because of the low molecular weights of the primary gas mixtures (the gases which are arc heated), arc instability problems were encountered. The combination of low molecular weight, high pressure, and the relatively low enthalpy, required high-operating voltage which was incompatible with the power supply. Instability and eventual blow-out of the arc occurred. The problem was alleviated by bypassing some of the primary gas and introducing it downstream of the arc. The resultant decrease in gas-flow rate through the arc and in arc voltage resulted in stable and smooth operation. Further tests were run to determine the required preset conditions to achieve the desired test conditions for Mixtures 4 and 5.

The Vidya sponsored calibration of the arc-plasma generator was also completed during the report period. The results are presented in Reference 20 and are discussed briefly here. A compact heat-exchanger calorimeter, schematically shown in Figure 20, was connected to the exit of the plasma generator to remove the energy in the exit gas stream. The energy input to the arc-heated gas as calculated by the conventional energy-balance method ( $P_{\text{gas}} = P_{\text{arc}} - P_{\text{cooling water}}$ ) was compared with

that absorbed by the calorimeter. The results are presented in Figure 21; almost all test points fall within a  $\pm 15$  percent band. The results of this program indicate that test conditions calculated by the energy balance method are reasonably accurate and that the test results are reproducible.

### 3.3.4 Test sections

#### 3.3.4.1 Calibration nozzles

Pressure distribution and heat-transfer calibration nozzles were fabricated to determine the nonablating wall-pressure distribution and heat transfer for a nozzle geometry identical to that of the material nozzle configurations. The data obtained from tests with these nozzles are required for the analysis and interpretation of the data obtained in the material nozzle firings.

As discussed in Reference 1, the pressure distribution nozzles are uncooled; the heat-sink capabilities of the copper bodies allow sufficient run times to obtain a steady-state pressure distribution. A photograph of one of the nozzles installed on the plasma generator is shown in Figure 22. The pressure-tap locations are presented in Figure 23. The pressure distribution is measured with a high-pressure manometer and pressure-gauge board in which the pressure readings are "trapped" by simultaneously closing a series of quick-acting valves after steady-state is reached. The board is then read and data recorded after the test. The board is visible on the right in Figure 22.

The set of calibration nozzles consists of three units of different throat diameter, 0.3, 0.4, and 0.5 inch. This range is required to cover both the pressure conditions at which tests are being run (see Table IV) and to provide information on the pressure distribution in the ablative-material nozzles as the throat diameter increases during each test.

Because of a fabrication problem, the original design of the heat-transfer calibration nozzles (Ref. 1) was changed.

Briefly, the fabrication technique was the electroforming of a copper-nozzle insert which contained thermocouple instrumentation for determination of the heat-flux and surface-wall temperature. The thermocouples were set in position before electroforming was begun and were therefore an integral part of the nozzle insert. However, no thermocouple insulation or protective coating was found that would holdup under the many hours of immersion in the electrolyte during the plating process. Also, due to the difference in the thermal conductivity of constantan and copper, heat conduction normal to the surface could cause significant errors in the measured surface temperatures. The original design was therefore discarded in favor of a steady-state calorimetric measurement of heat transfer, a method which has been used successfully in the past (e.g. Refs. 21 and 22).

The nozzle configuration is presented in Figure 24. It is made up of individually water-cooled segments which are stacked together to form the nozzle. The throat region is, of course, the region of most interest and therefore contains the most segments. The nozzle wall-material is copper. A 0.002-inch gap between segments (Fig. 24) serves as an insulator between the heat-transfer surfaces of adjacent segments. The water-flow rates in each segment are monitored by rotameters and the thermocouple outputs are recorded on an oscillograph. The set of three calorimeter nozzles have throat diameters of 0.3, 0.4, and 0.5 inch, the same as the pressure-distribution nozzles.

The heat-flux for each segment is determined from its measured water-flow rate and temperature rise. With the heat input to the cooling water calculated from these measurements and the known heated-surface area for each segment, the local average heat-flux is then calculated. This heat-flux is due to both convective and radiative heating. The convective heat-flux is expected to be the greater of the two in all regions of the nozzle. The radiative-flux is due to radiation interchange

between the gas stream and the nozzle wall and between the arc and the wall. This contribution to the total heat-flux is expected to be small in the absence of particles. The experimental results will be compared with theoretical predictions for convective heating (i.e., Bartz, ARM). Estimates of the radiative-flux will also be made.

#### 3.3.4.2 Ablative-material nozzles

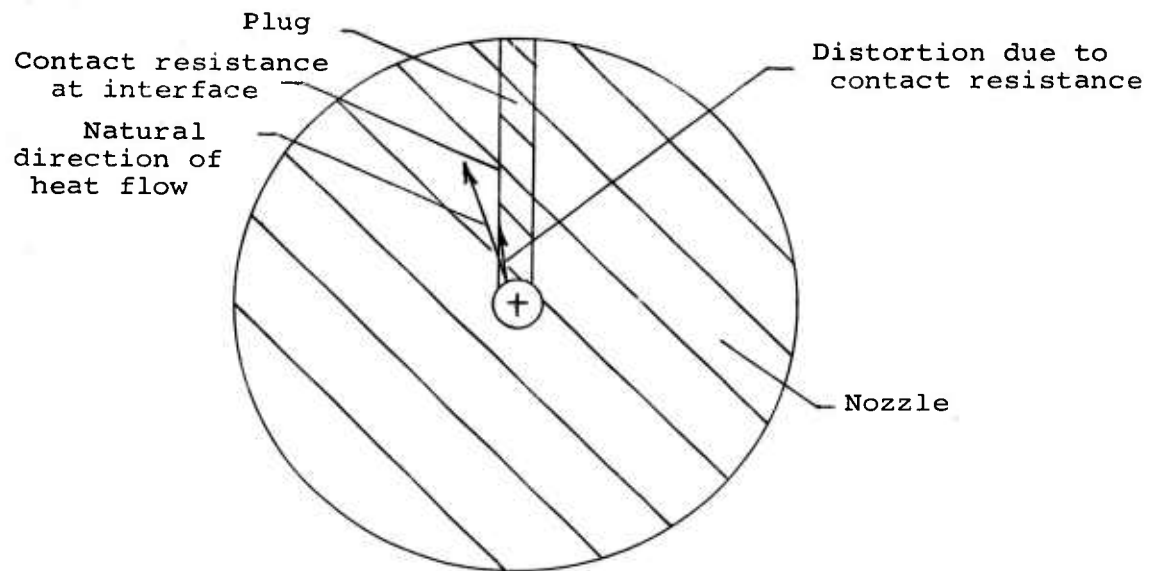
The nozzle firing phase of the program was discussed in some detail in Reference 1. In brief, the test section materials are graphite, silica phenolic, and graphite phenolic. The configuration of the 0.3-inch throat diameter nozzle is presented in Figure 25 for convenient reference. The internal wall-temperature distribution is measured as a function of time to allow determination of hot-side wall temperature. The determination of surface recession is made throughout the entire nozzle from pre- and post-test measurement of the internal-wall profile and at the throat, (the downstream end of the region of minimum cross-sectional area, as discussed in Section 3.3.5.1), from calculations based on the measured time variation of plenum pressure.

Because of its widespread usage, ATJ graphite was chosen as the graphite-nozzle material. Some of its shortcomings for this application have become apparent in the meantime however. After test, the wall surface in the throat region of the first graphite nozzle was quite rough and pitted. The low density and therefore high porosity of ATJ graphite is felt to be at least the partial cause of this surface condition. The condition could be the result of spalling or may be due to nonuniformities in porosity which cause nonuniform material removal by mechanical and/or chemical action. The high porosity could allow the material to absorb significant amounts of moisture or other gases. When the material is heated at high heat-flux, these gases may cause

spalling due to the rapid expansion of the gases. A further consequence of the high porosity is that the surface condition, microscopically, is quite rough and therefore offers a larger exposed surface area than the actual planer surface and a large number of active sites for chemical reaction.

Because of these problems, other higher-density graphites were investigated. Graph-i-tite, grade GX, was determined to be a reasonable possibility; it has a high density (Sp. gr. 1.90 as compared to 1.73 for ATJ), good thermal-shock characteristics, and is reasonably isotropic. A length of this graphite was therefore procured and a preliminary test will be run to check its performance. A decision will then be made on the graphite type to be used for all following tests.

The internal-temperature distributions of the test nozzles are being determined in order to allow calculation of the wall-surface temperature desired for the interpretation of test results. (Data reduction will be accomplished with the internal conduction program.) Originally, a plug technique was chosen as the method of thermocouple instrumentation to measure these distributions. Problems in fabrication and possible difficulties in data interpretation dictated a change in this decision. The machining of small tapered or threaded holes and the machining of the plugs themselves was found to be extremely difficult and time consuming for the phenolic test sections. The data-interpretation problem was due to the unknown effect of contact resistance at the interface between the plug and nozzle body. The plug configuration does not coincide with the material radial-direction of heat-flux and therefore any contact resistance at the nozzle body - plug interface, results in a distortion of the heat flux (see following sketch). A reliable estimate of this contact resistance for use in correcting for this effect is difficult, if not impossible. Hence, other thermocouple instrumentation techniques were investigated.



A prime requirement in thermocouple instrumentation, of course, is that the sensor does not disturb the heat flow at the point of measurement. To satisfy this requirement, the sensor should be as small as practical and the thermocouple leads in the vicinity of the junction should be placed along an isotherm. This last consideration is particularly important in low conductivity materials and is impressively illustrated in Reference 23. Also, the thermocouple junction must be in intimate contact with the material in order to eliminate errors due to contact resistance. Another obvious requirement is that the location of the junction be precisely known. After considering these requirements and the practical aspects of fabrication, the thermocouple installation scheme shown in Figure 26 was selected. A photograph of one of the thermocouple probes is presented in Figure 27. The probes are inserted into the test nozzle so that they are tangent to an isotherm at their junction. The diameter of the ceramic insulator which encloses the thermocouple wires is 0.035 inch and therefore offers a minimum disturbance to the heat flux. The thermocouples



are spring loaded against the bottom of the thermocouple probe hole to insure good contact of the thermocouple junction with the wall. The thermocouple wires are 36 gauge (0.005-inch-diameter). Chromel-Alumel thermocouples are used where temperatures are not expected to exceed  $2500^{\circ}$  F. Thermocouples of tungsten 5 percent rhenium and tungsten 26 percent rhenium are used for higher temperature locations. The small gauge of the wires further reduces the possibility of error due to conduction along the wires. The locations of the thermocouple junctions are determined by x-ray photography. The requirements for obtaining accurate data, discussed above, are therefore closely satisfied.

The thermocouple instrumentation is located at three axial positions in the tubular throat as shown in Figure 25. A typical installation at one of these positions is illustrated in Figure 26. The thermocouple radial locations and the analytically predicted temperature distributions for test nozzles of each material are presented in Figures 28(a) - (c). The distributions are idealized in that room temperature thermal properties were used, no ablation was assumed, and, for the phenolics, no allowance was made for char formation. The temperature distributions are for the throat region of a 0.3-inch diameter nozzle and were obtained from the tabulated solutions of Reference 24 for convective heating of a hollow cylinder. The results are for the highest heat-flux test condition ( $T_o = 3500^{\circ}$  K,  $p_o = 300$  psia). The thermocouple locations were chosen from consideration of these temperature distributions and the expected ablation rates.

### 3.3.5 Test results

Testing during the report period that was a direct part of the chemical erosion program consisted of a series of pressure distribution calibration tests and an ATJ graphite nozzle firing. The pressure distribution tests were performed with Mixtures 4 and 5 at the high-temperature test conditions and with the 0.3-inch

and 0.4-inch throat diameter nozzles. These conditions correspond to Test Points 28-31, 32, 39-42, and 43 (see Table 4). The nozzle firing was performed at Test Point 28 - Mixture 4 at the nominal conditions  $3500^{\circ}$  K total temperature and 300 psia initial plenum pressure. No thermocouple instrumentation was included in this test because of its preliminary nature as the first graphite nozzle firing.

### 3.3.5.1 Pressure distribution tests

The pressure distribution results are presented in Figures 29(a) and (b) and are discussed below. The test conditions for each test are indicated on the figures. In the tests with Mixture 5, the enthalpy and therefore temperature were inadvertently run higher than planned.

The circumferential variation of pressure was measured at the central section of the throat with four pressure taps  $90^{\circ}$  apart. In all tests, the variation was less than 2 psi which corresponds to a variation of less than 1 percent of the stagnation pressure. A fifth test, not presented in the figures, was run with Mixture 4 on the 0.4-inch diameter throat nozzle to check reproducibility. The points for this test fell almost identically on the appropriate points of Figure 29(b).

The theoretical pressure distribution for an idealized one-dimensional isentropic expansion in the nozzle are also presented in Figures 29. In a constant diameter tubular throat, the theoretical pressure in the absence of friction and heat transfer is constant. Actually however, boundary-layer effects will cause a pressure drop. The boundary layer would be expected to grow with increasing distance down the throat and therefore a decreasing effective flow area would result. The sonic point, the point of minimum area, would then be at the throat exit. If the tubular throat diameter were not exactly constant throughout due to machining nonuniformities, the pressure drop through the throat and the

location of the sonic point would be affected further. The combined effects of these nonuniformities and boundary-layer growth would result in an appreciable pressure drop and the sonic point would be expected somewhat downstream of the minimum physical diameter in the throat region.

Returning now to Figures 29, the agreement of the experimental results with the predicted distribution is good in the contraction and expansion sections. In the tubular throat, however, the agreement is not good and, based on the above discussion, is not too surprising. A constant pressure is predicted by theory whereas a pressure drop of approximately 58 psi occurs for the 0.3-inch diameter throat and approximately 18 psi for the 0.4-inch throat. This disagreement can be attributed to machining nonuniformities and boundary-layer effects discussed above. Variations occur in the real and effective flow area through the tubular throat which have a significant effect on the pressure distribution.

Measurements of the variation in diameter between the pressure taps in the throat (2 and 7) were made by traversing the throat with a pivot-arm dial gauge micrometer. For the 0.3-inch throat, the variation was 0.0046-inch over the distance between taps and the minimum diameter occurred close to the entrance to the throat. The pressure drop corresponding to the resultant variation in area is approximately 39 psi. The boundary-layer effect was also investigated by a simple calculation of the pressure drop due to the combined effects of friction and heat transfer (Ref. 25). For the 0.3-inch throat, this contribution is approximately 13 psi. The total predicted pressure drop due to machining nonuniformities and boundary-layer effects is therefore 52 psi as compared to the measured value of 58 psi. The agreement is surprisingly good. As seen in Figure 29(a), the experimental sonic points for both tests are approximately  $2/3$  of the distance down

the tubular throat. The combined effects of machining nonuniformities and boundary-layer growth apparently resulted in a minimum effective area at this point.

A similar analysis was made for the 0.4-inch throat nozzle. The variation in throat diameter was 0.0020-inch and results in a pressure drop of approximately 13 psi. The combined effects of friction and heat transfer contribute an 8 psi drop. The total predicted drop here is then 21 psi as compared to the measure value of 18 psi. Again the agreement is surprisingly good. The minimum physical throat diameter occurred approximately halfway down the throat. The sonic point, as seen from Figure 29(b), is close to the throat exit. Again boundary-layer growth apparently caused the effective area to be a minimum downstream of the point of the physical minimum area.

The experimental results indicate that the pressure distributions in the contraction and expansion sections of the nozzles are closely defined by a one-dimensional isentropic expansion. This does not apply in the tubular throat, but the pressure drop here can be predicted quite closely by considering both the actual nonuniformities in throat diameter and boundary-layer effects. Further pressure distribution tests will be performed to fully confirm this; testing over the complete range of test conditions is not anticipated because of the favorable results obtained so far.

#### 3.3.5.2 Chemical erosion test

The ATJ graphite-nozzle firing results are presented in Figures 30 and 31. A photograph of the firing is shown in Figure 32 and a post-test photograph of the nozzle is presented in Figure 33.

Figure 30 shows the before and after internal profile of the nozzle at one cross-section. The maximum surface recession occurred close to the entrance to the throat and corresponded

to an average recession rate over the 31.0 seconds of test of approximately 6.2 mils/sec. Over most of the tubular throat region, the recession was approximately uniform at an average rate of about 5.2 mils/sec. The recession was sufficiently great that no expansion section was left at the end of test; the minimum diameter was at the exit of the test section. The circumferential uniformity of erosion was difficult to measure in the throat region because of the roughness of the final surface, however visual inspection indicated no significant assymetry. Measurements were made in the contraction cone and the uniformity was good. The variation at one plane between two mutually perpendicular measurements of diameter did not exceed 0.008 inch or 1.5 percent of the diameter.

After test, the entire surface in the tubular throat region was quite rough as seen in Figure 33. As mentioned previously, this condition is felt to be at least partially due to the low density and therefore high porosity of ATJ graphite. Because of this condition, it appears that the mechanical removal of material was a significant contributor to the surface recession. A higher density graphite will be tested shortly and a choice will then be made as to the graphite type to be used in the rest of the test program.

The instantaneous throat surface recession may be determined for any time during a test firing from the time history of plenum pressure. The instantaneous nozzle throat area is directly related to the plenum pressure through the equation

$$A_* = \frac{1}{C_n} \frac{\dot{m}}{p_o} \sqrt{\frac{RT_o}{M}} \frac{1}{\sqrt{\gamma g \left( \frac{2}{\gamma+1} \right)^{\frac{\gamma+1}{\gamma-1}}}} \quad (63)$$

where  $C_n$  is a nozzle coefficient ( $C_n \leq 1$ ) which accounts for non-isentropic effects due to friction and heat transfer. The equation assumes that both the molecular weight  $M$  and isentropic

exponent  $\gamma$  are constant in the expansion process from plenum to sonic conditions. For the test gas mixtures, these properties actually vary somewhat in the expansion. Their variation is small, however, and therefore the equation yields accurate results.

Sufficient data are taken in each nozzle firing to determine all variables of Equation (63). The nozzle coefficient  $C_n$  is determined as that value which makes the measured throat area before test equal to the calculated throat area at the start of test before surface recession has begun. The throat area and diameter ( $A_*$  and  $D_*$ ) are then calculated as a function of time from the measured time variation of plenum pressure and other operating conditions. The surface recession, assuming the location of the throat does not shift with time, is then given at any time  $\theta$  simply by

$$\sigma = \frac{(D_*)_{\theta} - (D_*)_{\theta=0}}{2} \quad (64)$$

The results of this calculation for the graphite nozzle firing are presented in Figures 31(a) through (c); the plenum pressure, the surface recession, and the surface recession rate are presented as functions of test time. Unfortunately, as seen in Figure 30, the nozzle throat moved downstream with increasing test time until, at the end of test, the throat was actually at the nozzle exit. The evaluation of surface recession based on the throat calculations are therefore lower than the actual recession in what was the throat region before test. To eliminate this problem in future tests, consideration is being given to eliminating the expansion section in the test nozzles and decreasing the heat-sink effect of the nozzle retaining ring.

Turning now to the test results, Figure 31(b) shows the surface recession as a function of test time. It can be seen that the transient time to reach a quasi-steady ablation condition is approximately 8 seconds. The total predicted surface recession

(using Eq. (63)) after the 31.0 seconds of test is 102 mils. This corresponds to a final throat diameter of 0.513 inch as compared to the measured value after test of 0.554 inch. This discrepancy may well be due to the rough surface condition causing a decrease in the nozzle coefficient,  $C_n$ , during the firing. Also, the minimum diameter, the sonic point for which Equation (63) is valid, moved downstream with increasing test time until, at the end of test, it was at the nozzle exit. The calculated recession is therefore less than that for the tubular throat region. As discussed previously, efforts are being made to alleviate this problem.

The instantaneous surface-recession rate determined from Figure 31(b) is presented in Figure 31(c). The trend, a decreasing recession rate with increasing time, is as expected. An increase in diameter results in a decrease in the heat flux and the rate of species diffusion to the wall, thus decreasing the chemical erosion rate.

The theoretical surface-recession rate was also calculated from the dimensionless wall-recession rate for Mixture 4 predicted by Equation (53).

$$B' = \frac{3}{4} \left( \tilde{K}_o \right)_e \quad (53)$$

This equation assumes that chemical equilibrium exists at the wall and that chemical reaction is the only wall erosion mechanism. Recall that Equation (53) is essentially independent of wall temperature for Mixture 4 in the temperature range 2000° K to 3300° K (see Section 2.3.4), thus obviating the need for coupling the surface chemistry considerations with the internal conduction program. From Table III, the elemental mass fraction for Mixture 4 is  $\left( \tilde{K}_o \right)_e = 0.1525$  and therefore Equation (53) reduces to

$$B' = 0.1144 \quad (65)$$

$B'$  is defined in Equation (48) as

$$B' = \frac{(\rho v)_w}{\rho_e u_e C_M} \quad (48)$$

and is the ratio of the rate of introduction of wall material into the boundary layer to the rate of species diffusion to the wall. The term  $(\rho v)_w$  is related to the material behavior by

$$(\rho v)_w = \rho_m \frac{d\sigma}{d\theta} \quad (66)$$

where  $\rho_m$  is the density of the material and  $d\sigma/d\theta$  is the surface recession rate. From Equations (48), (65), and (66), the theoretical surface-recession rate for Mixture 4 is then given by

$$\frac{d\sigma}{d\theta} = 0.1144 \frac{\rho_e u_e C_M}{\rho_m} \quad (67)$$

The term  $\rho_e u_e C_M$  was determined from the heat-transfer coefficient from the simplified Bartz Equation (Eq. (56), Ref. 1). The Bartz equation was used instead of the ARM method because, as stated in Section 2.2.1, it is felt that the ARM method requires further verification before it can be recommended for all nozzle conditions. The diameter used in the calculation was that derived from the calculated throat area, Equation (63), and the Lewis-Semenov number was assumed to be unity

$$(\rho_e u_e C_M = \rho_e u_e C_H Le^{2/3})$$

The surface-recession rate as predicted from Equation (67) is indicated on Figure 31(c) as the dashed line. The agreement with the experimental results is amazingly good, but a word of caution is in order. In comparing results, it must be remembered that the surface recession presented in Figure 31(b) was lower than that measured after test by 16 percent. Based on this post-test measurement, the instantaneous experimental surface-recession



rate would be somewhat greater than that shown by the solid line of Figure 31(c), and thus greater than the theoretical prediction. This would be indicative of mechanical erosion in addition to the contribution of chemical reaction or, as discussed previously, a higher effective surface area for chemical reaction. Also note that Equation (67) assumes that chemical equilibrium obtains at the wall. If reaction is kinetically controlled, the contribution of chemical action to the surface recession is reduced, and the dashed line of Figure 31(c) would be lowered. Again, the resulting difference could be attributed to mechanical erosion. Further, had the ARM method been used with Equation (67) in generating the dashed curve, the curve would be lowered by about 30 percent, but would retain the same shape. If it is found that the ARM method is valid for the test conditions used, the resulting discrepancy between predicted and experimental curves would have to be attributed to mechanical erosion.

It is seen that the agreement between experiment and theory is not as clear cut as might be thought at first glance, primarily because of the counteracting effects of mechanical erosion and reaction kinetics. The test program is set up so that these individual contributions may be assessed; thus, a complete explanation of the results of Figure 31(c) will await further testing.

#### 3.4 Particle Impact Test Program

The particle impact program, the other phase of the experimental effort in the subject contract, is concerned with the effects of particle impingement on the material behavior in a rocket nozzle. The various mechanisms associated with the impact and presence of particles are therefore investigated. These mechanisms include thermal-energy transfer, kinetic-energy transfer, shear, chemical reactions, and effects on the convective and radiative heat-transfer.

Because of the large effort required by the chemical erosion test program, the progress in this phase of the program has been minimal. The primary effort to date has been the specific definition of instrumentation techniques and procedures. This instrumentation is, of necessity, somewhat unique and complicated in order to yield the desired test data. The general facility setup and checkout in preparation for the program has, for the most part, been completed in that the similar activities in preparation for the chemical erosion program are also applicable here. The program and instrumentation are discussed briefly below.

The Vidya arc-plasma generator is utilized to simulate the rocket-exhaust environment. The test gas to be used will be the simplest of the gas mixtures discussed previously which also adequately duplicates the nozzle materials response. Particles will be introduced in the plenum chamber of the plasma generator by a powder-hopper feed system or by a particle-slurry feed along with the secondary injection gases.

The test configuration consist of a flat-plate slab of the test material and is positioned in the hot-gas stream just downstream of the plasma generator nozzle exit. The test slab materials are tungsten, graphite, silica phenolic, and graphite phenolic. Tungsten is included for two reasons - first, it is a material used in rocket motors and second, it is a nonablator and, therefore, serves as a 'clean' basis for assessing particle-impact effects without the added complication of ablation. The angle of attack of the test slab with respect to the exit flow is variable. Plasma generator operation will first be established either with or without particles in the gas stream and then the test slab swung into position. Particle flow will be established before or at any time after the test material is exposed to the gas stream. Control tests with no particle loading will also be run to checkout the material performance with no particles present. The temperature response of the material will be monitored.

The test variables are the test-slab material, the slab wall-temperature, the plasma-generator operating conditions which will also influence the particle temperature and particle velocity, the particle size, the particle mass loading, and the angle of incidence of the particles on the test slab. The range of the last three parameters will be dictated in part by input from Aeronu-tronic under a companion program.

A number of special instrumentation techniques are required for data acquisition. Because of the high particle speeds, up to 5000 ft/sec, an image intensifier camera will be used for measure-ment of particle velocity both before and after impact. Film exposure is by electron bombardment rather than by the light emission from the particles. The extremely short exposure times required are therefore possible. Velocities will be determined by a streak-photography method similar to that used in star and satellite tracking in which an interrupted exposure is made. This allows measurement of leading-edge to leading-edge distance which limits tail-off errors inherent in single exposures. The measured particle displacement between the two exposures together with the interruption time (the order of a microsecond) allows calculation of the particle velocity. Because of the size of the zone of interest and the required camera location to keep it out of the hot environment, a complicated optics system is required. It is also anticipated that the optics will include the capability of photography in two perpendicular planes and thus allow a three-dimensional determination of particle speed and trajectory.

Particle temperatures both before and after impact will be measured by one or both of two techniques. One technique employs a two-color optical pyrometer which views the stream perpendicular to the flow direction. With large-particle loadings for which the particles appear as a cloud, the pyrometer will read out the cloud temperature and therefore the approximate particle temperature. For light-particle loadings, its utility is questionable however.

The possibility of making a tare measurement to account for the pyrometer response to the stream alone and of correcting for the fraction of its view field which includes particles is being considered. Hope is small here, however. The other method is applicable to light particle loadings and employs a technique developed at Vidya (Ref. 26). A double-image photograph of the particle-laden gas stream and of a calibrated tungsten filament is made. Temperature is then determined by a color densitometer analysis of the exposed film through comparison of the gas stream and filament images. The use of this technique in conjunction with the image intensifier camera is also being investigated.

The heat flux due to radiation from the particles will be determined by radiometer. In some cases, the heat flux into the test section will be determined from the measured internal temperature distribution. The thermocouple probes and data-reduction technique will be similar to those used in the chemical erosion program. At least one wall-temperature history will be obtained for each test section.

Particle sampling will also be attempted. A number of techniques are under study, however, none seem to offer a reliable and practical answer. The problem is still under investigation.

The complete definition of all instrumentation procedures will be completed during the next reporting period and setup begun. The actual start of testing in the program will necessarily depend on the time required to get all instrumentation set up and operating.

REFERENCES

1. Lundberg, R. E., Schaefer, J. W., and McCuen, P. A.: A Study of Solid-Propellant Rocket Motor Exposed Materials Behavior, First Quarterly Progress Report. Air Force Rpt. No. RTD-TDR-63-1038, Sept. 1963.
2. Rubesin, M. W.: The Effect of an Arbitrary Surface-Temperature Variation Along a Flat Plate on the Convective Heat Transfer in an Incompressible Turbulent Boundary Layer. NACA TN 2345, Apr. 1951.
3. Vidya Staff: Effects of Supersonic and Hypersonic Aircraft Speed Upon Aerial Photography. Vidya Rept. No. 37, Jan. 1961.
4. Ambrok, G. S.: Approximate Solution of Equations for Thermal Boundary Layer with Variations in Boundary Layer Structure. Soviet Physics, Tech. Physics, vol. 2, no. 9, 1957, p. 1979.
5. Mayer, E.: Analysis of Convective Heat Transfer in Rocket Nozzles. ARS Jour., July 1961.
6. Fischer, W. W. and Norris, R. H.: Supersonic Convective Heat Transfer Correlation from Skin-Temperature Measurements on a V-2 Rocket in Flight. ASME TRANS. July 1949.
7. Sommers, S. C. and Short, B. J.: Free-Flight Measurements of Turbulent Boundary-Layer Skin Friction in the Presence of Severe Aerodynamic Heating at Mach Numbers from 2.8 to 7.0. NACA TN 3391, Mar. 1955.
8. Massier, P. F., Gier, H. L., Witte, A. B., and Harper, E. Y.: A. Heat Transfer and Fluid Mechanics. Jet Propulsion Laboratory Research Summary No. 36-11, for the period Aug. 1, 1961 to Oct. 1, 1961, pp. 80-89.
9. Bartz, D. R.: An Approximate Solution of Compressible Turbulent Boundary-Layer Development and Convective Heat Transfer in Convergent-Divergent Nozzles. ASME TRANS., Nov. 1955.
10. Scala, S. M.: The Ablation of Graphite in Dissociated Air Part I - Theory, General Electric Rept. R62S072, Sept. 1962.
11. Trapnell, B.: Chemisorption, Butterworths, 1955.
12. Roberts, J.: Some Problems in Adsorption, Cambridge, 1939.

13. Glasstone, S., Laidler, K. J., and Eyring, H.: The Theory of Rate Processes, McGraw-Hill, 1941.
14. Binford and Eyring, H.: Kinetics of the Steam-Carbon Reaction, Jour. Phys. Chem., vol. 60, 1956, p. 486.
15. Blyholder, G. D., and Eyring, H.: Kinetics of the Steam-Carbon Reaction, Jour. Phys. Chem., vol. 61, 1957, p. 682.
16. Lowrie, R., et al.: Research on Physical and Chemical Principles Affecting High Temperature Materials for Rocket Nozzles, Semiannual Progress Report, Contract No. DA-30-0690 ORD-2787, Union Carbide Research Institute, Jun. 30, 1961.
17. Lowrie, R., et al.: Research on Physical and Chemical Principles Affecting High Temperature Materials for Rocket Nozzles, Semiannual Progress Report, Contract No. DA-30-069-ORD-2787, Union Carbide Research Institute, Dec. 31, 1961.
18. Schneider, P. J.: Temperature Response Charts, John Wiley and Sons, New York, 1963.
19. Ragent, B. and Noble, C. E. Jr.: High Temperature Transport Coefficients of Selected Gases. Vidya Report No. 52, Sept. 1, 1961.
20. Rubesin, M. W., Higgins, R. W., and Flood, D. T.: The Characteristics of a Magnetically Driven Arc-Plasma Generator for Use in Re-entry and Rocket Nozzle Environment Simulation. Vidya Rept. No. 117, to be published Jan. 15, 1964. (Presented at ASME Regional Conference, San Mateo, Calif., Oct. 15, 1963.)
21. Massier, P. F., Noel, M. B., and Back, L. H.: A. Heat Transfer and Fluid Mechanics. Jet Propulsion Laboratory Space Programs Summary No. 37-22, vol. IV, for the period June. 1, 1963 to July. 31, 1963, Aug. 31, 1963. pp. 119-125.
22. Massier, P. F., and Noel, M. B.: A. Heat Transfer and Fluid Mechanics. Jet Propulsion Laboratory Space Programs Summary No. 37-19, vol. IV, for the period Dec. 1, 1962 to Jan. 31, 1963, Feb. 28, 1963, pp. 119-125.
23. Jakob, Max: Heat Transfer, vol. II, Wiley, 1957, pp. 148 and 149.
24. Thorne, C. J. and Morrin, H. C.: Temperature Tables, Part 2, NAVORD Rept. 5562, Part 2, Mar. 15, 1960.

25. Shapiro, A. H.: The Dynamics and Thermodynamics of Compressible Fluid Flow, vol. I, Ronald Press, 1953, Chap. 8.
26. Tickner, E. G.: Laboratory Report on the Determination of Surface Temperature vis Color Photography and Two-Color Pyrometer Techniques. Vidya Internal Publication, Feb. 26, 1963.
27. Kulgein, N. G.: Transport Processes in a Combustible Turbulent Boundary-Layer, Jour. Fluid Mech. vol. 12, part 3, p. 417, Mar. 1962.
28. O'Brien, G. G., Hymen, M. A., and Kaplan, S.: A Study of the Numerical Solution of Partial Differential Equations, Jour. Math. Phys., vol. 29, 1951.

TABLE I

PROPELLANT COMPOSITION AND PRODUCT SPECIES FOR  
WALL EROSION CALCULATION

Fuel	Percent By Mass	Oxidizer	Percent By Mass
$C_{6.884}H_{10.089}N_{0.264}O_{0.278}$	39.667	$NH_4ClO_4$	100
$C_{21}H_{24}O_2$	7.000	$\frac{\text{Mass Oxidizer}}{\text{Mass Fuel}} = 2.333$	
Al	53.333		

Product Species Considered

H	OH	$CO_2$	N
O	$O_2$	Cl	$Cl_2$
$CH_4$	C	$H_2$	$H_2O$
CO	$N_2$	HCl	$C_2H_2$
CN	$C_2$	$C_3$	$C_2H$
$C_3H$	$C_4H$	$C_6H$	$CH_2$
$C_4H_2$	$C_3H_2$		



TABLE II

CHEMICAL EROSION OF GRAPHITE IN H, C, N, O, and Cl EXHAUST

T (°K)	P (atm)	B'	H ( $\frac{\text{cal}}{\text{gm}}$ )	S ( $\frac{\text{cal}}{\text{gm-}^\circ\text{K}}$ )	M	$\rho_e u_e C_M$ ( $\frac{\text{lb}}{\text{ft}^2\text{-sec}}$ )	$(K_{H_2O})_e$	
1500.0	5.0	.0270	-.4920E+03	2.65	20.11	1.000E-01	.1178	2
1500.0	5.0	.0269	-.4922E+03	2.65	20.11	1.000E-00	.1178	2
1500.0	5.0	.0269	-.4922E+03	2.65	20.11	2.000E-00	.1178	2
1500.0	10.0	.0275	-.4933E+03	2.58	20.15	1.000E-01	.1178	2
1500.0	10.0	.0274	-.4936E+03	2.58	20.15	1.000E-00	.1178	2
1500.0	10.0	.0274	-.4936E+03	2.58	20.15	2.000E-00	.1178	2
1500.0	25.0	.0291	-.4969E+03	2.49	20.26	1.000E-01	.1178	2
1500.0	25.0	.0289	-.4976E+03	2.49	20.26	1.000E-00	.1178	2
1500.0	25.0	.0289	-.4977E+03	2.49	20.26	2.000E-00	.1178	2
1500.0	40.0	.0306	-.5003E+03	2.43	20.37	1.000E-01	.1178	2
1500.0	40.0	.0302	-.5015E+03	2.43	20.37	1.000E-00	.1178	2
1500.0	40.0	.0302	-.5016E+03	2.43	20.37	2.000E-00	.1178	2
1500.0	50.0	.0315	-.5025E+03	2.41	20.43	1.000E-01	.1178	2
1500.0	50.0	.0310	-.5040E+03	2.41	20.44	1.000E-00	.1178	2
1500.0	50.0	.0310	-.5041E+03	2.41	20.44	2.000E-00	.1178	2
2000.0	5.0	.0286	-.2643E+03	2.78	20.04	1.000E-01	.1178	2
2000.0	5.0	.0267	-.2710E+03	2.78	20.07	1.000E-00	.1178	2
2000.0	5.0	.0266	-.2714E+03	2.78	20.07	2.000E-00	.1178	2
2000.0	10.0	.0304	-.2591E+03	2.71	20.03	1.000E-01	.1178	2
2000.0	10.0	.0270	-.2709E+03	2.71	20.07	1.000E-00	.1178	2
2000.0	10.0	.0268	-.2716E+03	2.71	20.08	2.000E-00	.1178	2
2000.0	25.0	.0352	-.2443E+03	2.62	19.99	1.000E-01	.1178	2
2000.0	25.0	.0278	-.2698E+03	2.62	20.09	1.000E-00	.1178	2
2000.0	25.0	.0274	-.2714E+03	2.62	20.09	2.000E-00	.1178	2
2000.0	40.0	.0394	-.2313E+03	2.58	19.96	1.000E-01	.1178	2
2000.0	40.0	.0287	-.2685E+03	2.57	20.10	1.000E-00	.1178	2
2000.0	40.0	.0279	-.2710E+03	2.57	20.11	2.000E-00	.1178	2
2000.0	50.0	.0421	-.2236E+03	2.56	19.95	1.000E-01	.1178	2
2000.0	50.0	.0292	-.2676E+03	2.55	20.11	1.000E-00	.1178	2
2000.0	50.0	.0283	-.2706E+03	2.55	20.12	2.000E-00	.1178	2
2300.0	5.0	.0384	-.8912E+02	2.85	19.89	1.000E-01	.1178	2
2300.0	5.0	.0277	-.1262E+03	2.85	20.03	1.000E-00	.1178	2
2300.0	5.0	.0271	-.1285E+03	2.85	20.04	2.000E-00	.1178	2
2300.0	10.0	.0435	-.7426E+02	2.78	19.84	1.000E-01	.1178	2
2300.0	10.0	.0285	-.1260E+03	2.78	20.03	1.000E-00	.1178	2
2300.0	10.0	.0275	-.1295E+03	2.78	20.04	2.000E-00	.1178	2
2300.0	25.0	.0548	-.3897E+02	2.70	19.72	1.000E-01	.1178	2
2300.0	25.0	.0306	-.1211E+03	2.69	20.02	1.000E-00	.1178	2
2300.0	25.0	.0287	-.1279E+03	2.69	20.05	2.000E-00	.1178	2
2300.0	40.0	.0627	-.1482E+02	2.65	19.65	1.000E-01	.1178	2
2300.0	40.0	.0327	-.1154E+03	2.64	20.01	1.000E-00	.1178	2
2300.0	40.0	.0299	-.1252E+03	2.64	20.04	2.000E-00	.1178	2
2300.0	50.0	.0667	-.2604E+01	2.63	19.61	1.000E-01	.1178	2
2300.0	50.0	.0340	-.1116E+03	2.62	20.00	1.000E-00	.1178	2
2300.0	50.0	.0306	-.1233E+03	2.62	20.04	2.000E-00	.1178	2
2500.0	5.0	.0596	.8547E+02	2.90	19.60	1.000E-01	.1178	2
2500.0	5.0	.0303	-.1419E+02	2.89	19.96	1.000E-00	.1178	2
2500.0	5.0	.0284	-.2100E+02	2.89	19.98	2.000E-00	.1178	2
2500.0	10.0	.0657	.9955E+02	2.83	19.55	1.000E-01	.1178	2
2500.0	10.0	.0318	-.1491E+02	2.82	19.96	1.000E-00	.1178	2
2500.0	10.0	.0292	-.2397E+02	2.82	19.99	2.000E-00	.1178	2
2500.0	25.0	.0772	.1303E+03	2.74	19.45	1.000E-01	.1178	2
2500.0	25.0	.0357	-.6677E+01	2.73	19.93	1.000E-00	.1178	2
2500.0	25.0	.0314	-.2168E+02	2.73	19.99	2.000E-00	.1178	2
2500.0	40.0	.0837	.1483E+03	2.69	19.40	1.000E-01	.1178	2
2500.0	40.0	.0393	.3157E+01	2.68	19.90	1.000E-00	.1178	2
2500.0	40.0	.0335	-.1674E+02	2.68	19.98	2.000E-00	.1178	2

TABLE II.- CONTINUED

T (°K)	P (atm)	B'	H ( $\frac{\text{cal}}{\text{gm}}$ )	S ( $\frac{\text{cal}}{\text{gm-}^\circ\text{K}}$ )	M	$\rho_e u_e c_M$ ( $\frac{\text{lb}}{\text{ft}^2\text{-sec}}$ )	( $K_{H_2O}$ ) <sub>e</sub>	
2500.0	50.0	.0868	.1565E+03	2.67	19.38	1.000E-01	.1178	2
2500.0	50.0	.0414	.9477E+01	2.66	19.88	1.000E-00	.1178	2
2500.0	50.0	.0348	.1321E+02	2.66	19.97	2.000E-00	.1178	2
2600.0	5.0	.0796	.2068E+03	2.93	19.34	1.000E-01	.1178	2
2600.0	5.0	.0330	.5129E+02	2.91	19.89	1.000E-00	.1178	2
2600.0	5.0	.0298	.3987E+02	2.91	19.93	2.000E-00	.1178	2
2600.0	10.0	.0841	.2118E+03	2.86	19.33	1.000E-01	.1178	2
2600.0	10.0	.0349	.4917E+02	2.84	19.90	1.000E-00	.1178	2
2600.0	10.0	.0308	.3490E+02	2.84	19.95	2.000E-00	.1178	2
2600.0	25.0	.0921	.2276E+03	2.76	19.30	1.000E-01	.1178	2
2600.0	25.0	.0400	.5852E+02	2.75	19.87	1.000E-00	.1178	2
2600.0	25.0	.0337	.3706E+02	2.75	19.94	2.000E-00	.1178	2
2600.0	40.0	.0966	.2375E+03	2.71	19.29	1.000E-01	.1178	2
2600.0	40.0	.0443	.7015E+02	2.70	19.83	1.000E-00	.1178	2
2600.0	40.0	.0364	.4316E+02	2.70	19.93	2.000E-00	.1178	2
2600.0	50.0	.0987	.2422E+03	2.69	19.29	1.000E-01	.1178	2
2600.0	50.0	.0470	.7752E+02	2.68	19.81	1.000E-00	.1178	2
2600.0	50.0	.0381	.4755E+02	2.68	19.91	2.000E-00	.1178	2
2700.0	5.0	.1071	.3543E+03	2.95	19.04	1.000E-01	.1178	2
2700.0	5.0	.0374	.1270E+03	2.93	19.79	1.000E-00	.1178	2
2700.0	5.0	.0321	.1082E+03	2.93	19.86	2.000E-00	.1178	2
2700.0	10.0	.1080	.3423E+03	2.88	19.10	1.000E-01	.1178	2
2700.0	10.0	.0398	.1224E+03	2.86	19.81	1.000E-00	.1178	2
2700.0	10.0	.0334	.1002E+03	2.86	19.89	2.000E-00	.1178	2
2700.0	25.0	.1106	.3361E+03	2.78	19.19	1.000E-01	.1178	2
2700.0	25.0	.0460	.1317E+03	2.77	19.78	1.000E-00	.1178	2
2700.0	25.0	.0371	.1015E+03	2.77	19.88	2.000E-00	.1178	2
2700.0	40.0	.1131	.3375E+03	2.73	19.25	1.000E-01	.1178	2
2700.0	40.0	.0512	.1445E+03	2.72	19.74	1.000E-00	.1178	2
2700.0	40.0	.0405	.1086E+03	2.72	19.86	2.000E-00	.1178	2
2700.0	50.0	.1147	.3396E+03	2.70	19.29	1.000E-01	.1178	2
2700.0	50.0	.0542	.1525E+03	2.70	19.72	1.000E-00	.1178	2
2700.0	50.0	.0426	.1138E+03	2.70	19.85	2.000E-00	.1178	2
2800.0	5.0	.1124	.4381E+03	2.97	19.05	1.000E-01	.1178	2
2800.0	5.0	.0447	.2184E+03	2.95	19.66	1.000E-00	.1178	2
2800.0	5.0	.0359	.1877E+03	2.95	19.76	2.000E-00	.1178	2
2800.0	10.0	.1151	.4244E+03	2.89	19.16	1.000E-01	.1178	2
2800.0	10.0	.0475	.2094E+03	2.88	19.70	1.000E-00	.1178	2
2800.0	10.0	.0376	.1753E+03	2.88	19.80	2.000E-00	.1178	2
2800.0	25.0	.1227	.4252E+03	2.79	19.36	1.000E-01	.1178	2
2800.0	25.0	.0549	.2171E+03	2.79	19.69	1.000E-00	.1178	2
2800.0	25.0	.0423	.1747E+03	2.79	19.81	2.000E-00	.1178	2
2800.0	40.0	.1272	.4294E+03	2.73	19.46	1.000E-01	.1178	2
2800.0	40.0	.0609	.2302E+03	2.74	19.66	1.000E-00	.1178	2
2800.0	40.0	.0465	.1825E+03	2.74	19.80	2.000E-00	.1178	2
2800.0	50.0	.1271	.4259E+03	2.71	19.47	1.000E-01	.1178	2
2800.0	50.0	.0643	.2385E+03	2.72	19.64	1.000E-00	.1178	2
2800.0	50.0	.0490	.1883E+03	2.72	19.78	2.000E-00	.1178	2
2900.0	5.0	.1290	.5628E+03	2.98	19.21	1.000E-01	.1178	2
2900.0	5.0	.0571	.3350E+03	2.98	19.50	1.000E-00	.1178	2
2900.0	5.0	.0428	.2850E+03	2.97	19.64	2.000E-00	.1178	2
2900.0	10.0	.1368	.5524E+03	2.89	19.44	1.000E-01	.1178	2
2900.0	10.0	.0605	.3193E+03	2.90	19.57	1.000E-00	.1178	2
2900.0	10.0	.0448	.2661E+03	2.90	19.71	2.000E-00	.1178	2
2900.0	25.0	.1380	.5266E+03	2.79	19.56	1.000E-01	.1178	2
2900.0	25.0	.0692	.3230E+03	2.81	19.60	1.000E-00	.1178	2
2900.0	25.0	.0508	.2623E+03	2.80	19.74	2.000E-00	.1178	2

TABLE II.- CONTINUED

T (°K)	P (atm)	B'	H ( $\frac{\text{cal}}{\text{gm}}$ )	S ( $\frac{\text{cal}}{\text{gm-}^\circ\text{K}}$ )	M	$P_e u_e C_M$ ( $\frac{\text{lb}}{\text{ft}^2\text{-sec}}$ )	$(K_{H_2O})_e$	
2900.0	40.0	.0560	.2705E+03	2.76	19.74	2.000E-00	.1178	2
2900.0	40.0	.1369	.5130E+03	2.74	19.58	1.000E-01	.1178	2
2900.0	40.0	.0763	.3360E+03	2.76	19.61	1.000E-00	.1178	2
2900.0	50.0	.0804	.3447E+03	2.74	19.62	1.000E-00	.1178	2
2900.0	50.0	.1364	.5075E+03	2.72	19.59	1.000E-01	.1178	2
2900.0	50.0	.0591	.2770E+03	2.73	19.73	2.000E-00	.1178	2
3000.0	5.0	.1670	.7547E+03	2.97	19.66	1.000E-01	.1178	2
3000.0	5.0	.0800	.4964E+03	3.00	19.36	1.000E-00	.1178	2
3000.0	5.0	.0558	.4136E+03	2.99	19.52	2.000E-00	.1178	2
3000.0	10.0	.1596	.6909E+03	2.90	19.69	1.000E-01	.1178	2
3000.0	10.0	.0840	.4704E+03	2.92	19.48	1.000E-00	.1178	2
3000.0	10.0	.0583	.3853E+03	2.92	19.63	2.000E-00	.1178	2
3000.0	25.0	.1529	.6330E+03	2.80	19.73	1.000E-01	.1178	2
3000.0	25.0	.0952	.4686E+03	2.82	19.62	1.000E-00	.1178	2
3000.0	25.0	.0661	.3768E+03	2.82	19.72	2.000E-00	.1178	2
3000.0	40.0	.1505	.6117E+03	2.75	19.75	1.000E-01	.1178	2
3000.0	40.0	.1047	.4826E+03	2.77	19.71	1.000E-00	.1178	2
3000.0	40.0	.0731	.3859E+03	2.77	19.75	2.000E-00	.1178	2
3000.0	50.0	.1496	.6032E+03	2.73	19.75	1.000E-01	.1178	2
3000.0	50.0	.1103	.4929E+03	2.74	19.77	1.000E-00	.1178	2
3000.0	50.0	.0773	.3936E+03	2.75	19.77	2.000E-00	.1178	2
3100.0	5.0	.2023	.9502E+03	2.96	19.98	1.000E-01	.1178	2
3100.0	5.0	.1265	.7416E+03	3.01	19.37	1.000E-00	.1178	2
3100.0	5.0	.0829	.6015E+03	3.01	19.49	2.000E-00	.1178	2
3100.0	10.0	.1878	.8535E+03	2.90	19.98	1.000E-01	.1178	2
3100.0	10.0	.1315	.7003E+03	2.93	19.60	1.000E-00	.1178	2
3100.0	10.0	.0860	.5595E+03	2.93	19.65	2.000E-00	.1178	2
3100.0	25.0	.1748	.7645E+03	2.80	19.98	1.000E-01	.1178	2
3100.0	25.0	.1478	.6919E+03	2.81	19.95	1.000E-00	.1178	2
3100.0	25.0	.0971	.5450E+03	2.83	19.86	2.000E-00	.1178	2
3100.0	40.0	.1701	.7315E+03	2.76	19.98	1.000E-01	.1178	2
3100.0	40.0	.1551	.6907E+03	2.76	20.08	1.000E-00	.1178	2
3100.0	40.0	.1075	.5566E+03	2.77	19.98	2.000E-00	.1178	2
3100.0	50.0	.1682	.7183E+03	2.74	19.98	1.000E-01	.1178	2
3100.0	50.0	.1548	.6815E+03	2.74	20.07	1.000E-00	.1178	2
3100.0	50.0	.1138	.5670E+03	2.75	20.05	2.000E-00	.1178	2
3200.0	5.0	.2582	.1206E+04	2.95	20.50	1.000E-01	.1178	2
3200.0	5.0	.2192	.1114E+04	2.98	19.94	1.000E-00	.1178	2
3200.0	5.0	.1432	.9024E+03	3.01	19.77	2.000E-00	.1178	2
3200.0	10.0	.2315	.1064E+04	2.89	20.41	1.000E-01	.1178	2
3200.0	10.0	.2258	.1051E+04	2.89	20.33	1.000E-00	.1178	2
3200.0	10.0	.1466	.8396E+03	2.92	20.03	2.000E-00	.1178	2
3200.0	25.0	.2073	.9310E+03	2.80	20.34	1.000E-01	.1178	2
3200.0	25.0	.2073	.9310E+03	2.80	20.34	1.000E-00	.1178	2
3200.0	25.0	.1635	.8152E+03	2.81	20.44	2.000E-00	.1178	2
3200.0	40.0	.1986	.8807E+03	2.76	20.31	1.000E-01	.1178	2
3200.0	40.0	.1986	.8807E+03	2.76	20.31	1.000E-00	.1178	2
3200.0	40.0	.1668	.7965E+03	2.76	20.50	2.000E-00	.1178	2
3200.0	50.0	.1950	.8604E+03	2.74	20.30	1.000E-01	.1178	2
3200.0	50.0	.1950	.8604E+03	2.74	20.30	1.000E-00	.1178	2
3200.0	50.0	.1658	.7829E+03	2.74	20.48	2.000E-00	.1178	2
3600.0	5.0	.9195	.2796E+04	2.75	26.18	1.000E-01	.1178	2
3600.0	5.0	.9195	.2796E+04	2.75	26.18	1.000E-00	.1178	2
3600.0	5.0	.9195	.2796E+04	2.75	26.18	2.000E-00	.1178	2
3600.0	10.0	.7572	.2494E+04	2.73	25.28	1.000E-01	.1178	2
3600.0	10.0	.7572	.2494E+04	2.73	25.28	1.000E-00	.1178	2
3600.0	10.0	.7572	.2494E+04	2.73	25.28	2.000E-00	.1178	2

TABLE II.- CONCLUDED

T (°K)	P (atm)	B'	H $\left(\frac{\text{cal}}{\text{gm}}\right)$	S $\left(\frac{\text{cal}}{\text{gm-}^\circ\text{K}}\right)$	M	$\rho_e u_e C_M$ $\left(\frac{\text{lb}}{\text{ft}^2\text{-sec}}\right)$	$(K_{\text{H}_2\text{O}})_e$	
3600.0	25.0	.5867	.2118E+04	2.70	24.19	1.000E-01	.1178	2
3600.0	25.0	.5867	.2118E+04	2.70	24.19	1.000E-00	.1178	2
3600.0	25.0	.5867	.2118E+04	2.70	24.19	2.000E-00	.1178	2
3600.0	40.0	.5188	.1946E+04	2.68	23.71	1.000E-01	.1178	2
3600.0	40.0	.5187	.1946E+04	2.68	23.71	1.000E-00	.1178	2
3600.0	40.0	.5187	.1946E+04	2.68	23.71	2.000E-00	.1178	2
3600.0	50.0	.4908	.1871E+04	2.67	23.50	1.000E-01	.1178	2
3600.0	50.0	.4908	.1871E+04	2.67	23.50	1.000E-00	.1178	2
3600.0	50.0	.4908	.1871E+04	2.67	23.50	2.000E-00	.1178	2

TABLE III.- COMPOSITION OF TEST GAS MIXTURES

(a) Elemental Composition.

Element	Mixture 1		Mixture 2		Mixture 3		Mixture 4		Mixture 5	
	$x_j$	$K_j$	$x_j$	$K_j$	$x_j$	$K_j$	$x_j$	$K_j$	$x_j$	$K_j$
H	0.5006	0.0538	0.4011	0.0452	0.4015	0.452	--	--	--	--
He	--	--	--	--	--	--	0.5150	0.2284	0.5020	0.2237
C	.1265	.1620	.1207	.1620	--	--	--	--	--	--
N	.0843	.1259	.2793	.4372	.5131	.8023	.3990	.6191	.4980	.7764
O	.2085	.3556	.1989	.3556	.0854	.1525	.0860	.1525	--	--
Cl	.0801	.3028	--	--	--	--	--	--	--	--

TABLE III.- CONTINUED

(b) Molecular composition; temperature, 3500° K; pressure, 20 atm.

Molecule	Mixture 1		Mixture 2		Mixture 3		Mixture 4		Mixture 5	
	$x_j$	$K_j$	$x_j$	$K_j$	$x_j$	$K_j$	$x_j$	$K_j$	$x_j$	$K_j$
H	0.0666	0.0034	0.0654	0.0035	0.0627	0.0033	--	--	--	--
H <sub>2</sub>	.2692	.0281	.2478	.0269	.2278	.0246	--	--	--	--
He	--	--	--	--	--	--	0.6728	0.2283	0.6684	0.2236
C	0	0	0	0	--	--	--	--	--	--
N	0	0	0	0	0	0	0	0	0	0
O	.0024	.0019	.0024	.0021	.0031	.0026	.0208	.0282	--	--
HO	.0160	.0141	.0162	.0148	.0198	.0180	--	--	--	--
H <sub>2</sub> O	.1340	.1252	.1273	.1236	.1491	.1439	--	--	--	--

TABLE III.- CONTINUED

(b) Concluded.

Molecule	Mixture 1		Mixture 2		Mixture 3		Mixture 4		Mixture 5	
	$x_j$	$K_j$	$x_j$	$K_j$	$x_j$	$K_j$	$x_j$	$K_j$	$x_j$	$K_j$
CO	0.2449	0.3556	0.2352	0.3549	--	--	--	--	--	--
N <sub>2</sub>	.0866	.1258	.2897	.4372	0.5323	.7991	0.2509	.5962	0.3314	.7762
NO	--	--	--	--	.0041	.0067	.0192	.0489	--	--
O <sub>2</sub>	.0005	.0007	.0004	.0008	.0008	.0013	.0361	.0981	--	--
Cl	.0246	.0451	--	--	--	--	--	--	--	--
HCl	.1400	.2647	--	--	--	--	--	--	--	--
CO <sub>2</sub>	.0152	.0347	.0151	.0358	--	--	--	--	--	--
Molecular Weight	19.28		18.56		18.66		11.79		11.96	

TABLE III.- CONTINUED

(c) Molecular composition; temperature 3500° K; pressure, 10 atm.

Molecule	Mixture 1		Mixture 2		Mixture 3		Mixture 4		Mixture 5	
	$x_j$	$K_j$	$x_j$	$K_j$	$x_j$	$K_j$	$x_j$	$K_j$	$x_j$	$K_j$
H	0.0914	0.0048	0.0902	0.0049	0.0870	0.0047	--	--	--	--
H <sub>2</sub>	.2592	.0277	.2357	.0260	.2190	.0241	--	--	--	--
H <sub>e</sub>	--	--	--	--	--	--	0.6703	0.2283	0.6684	0.2236
C	0	0	0	0	--	--	--	--	--	--
N	0	0	0	0	0	0	0	0	.0001	.0001
O	.0045	.0038	.0046	.0041	.0058	.0050	.0280	.0381	--	--
HO	.0209	.0189	.0215	.0201	.0257	.0239	--	--	--	--
H <sub>2</sub> O	.1232	0.1178	.1166	.1153	.1344	.1324	--	--	--	--



TABLE III.- CONTINUED

(c) Concluded.

Molecule	Mixture 1		Mixture 2		Mixture 3		Mixture 4		Mixture 5	
	$x_j$	$K_j$	$x_j$	$K_j$	$x_j$	$K_j$	$x_j$	$K_j$	$x_j$	$K_j$
CO	0.2399	0.3566	0.2313	0.3557	--	--	--	--	--	--
N <sub>2</sub>	.846	.1258	.2843	.4372	.5209	.7980	.2504		.3314	
NO	--	--	--	--	.0054		.0183		--	0.7761
O <sub>2</sub>	.0008	.0014	.0009	.0016	.0014	.0024	.0328	.0893	--	--
Cl	.0327	.0616	--	--	--	--	--	--	--	--
HCl	.1281	.2479	--	--	--	--	--	--	--	--
CO <sub>2</sub>	.0142	.0333	.0143	.0346	--	--	--	--	--	--
Molecular Weight	18.84		18.21		18.28		11.74		11.96	

TABLE III.- CONTINUED

(d) Molecular composition; temperature, 2500° K; pressure 10 atm.

Molecule	Mixture 1		Mixture 2		Mixture 3		Mixture 4		Mixture 5	
	$x_j$	$K_j$	$x_j$	$K_j$	$x_j$	$K_j$	$x_j$	$K_j$	$x_j$	$K_j$
H	0.0043	0.0002	0.0042	0.0002	0.0039	0.0002	--	--	--	--
H <sub>2</sub>	.2992	.0296	.2836	.0295	.2501	.0258	--	--	--	--
H <sub>e</sub>	--	--	--	--	--	--	0.6795	0.2283	0.6684	0.2236
C	0	0	0	0	--	--	--	--	--	--
N	0	0	0	0	0	0	0	0	0	0
O	0	0	0	0	0	0	.0010	.0014	--	--
HO	.0004	.0004	.0004	.0004	.0006	.0005	--	--	--	--
H <sub>2</sub> O	.1558	.1378	.1481	.1377	.1855	.1710	--	--	--	--

TABLE III.- CONTINUED

(d) Concluded.

Molecule	Mixture 1		Mixture 2		Mixture 3		Mixture 4		Mixture 5	
	$x_j$	$K_j$	$x_j$	$K_j$	$x_j$	$K_j$	$x_j$	$K_j$	$x_j$	$K_j$
CO	0.2531	0.3479	0.2405	0.3479	--	--	--	--	--	--
N <sub>2</sub>	.0915	.1258	.3022	.4372	.5596	.8022	.2597	0.6110	.3315	0.7763
NO	--	--	--	--	0	0	.0068	.0172	--	--
O <sub>2</sub>	0	0	0	0	0	0	.0528	.1418	--	--
Cl	.0018	.0031	--	--	--	--	--	--	--	--
HCl	.1721	.3081	--	--	--	--	--	--	--	--
CO <sub>2</sub>	.0216	.0467	.0206	.0468	--	--	--	--	--	--
Molecular Weight	20.36		19.36		19.54		11.90		11.96	

TABLE IV  
CHEMICAL EROSION PROGRAM TEST CONDITIONS

Test Point	Mixture	Material	Total Temperature (°K)	Plenum Pressure (psia)
1	1	Graphite	3500	300 (0.3) *
2	1	Silica Phenolic	3500	300 (0.3)
3	1	Graphite Phenolic	3500	300 (0.3)
4	1	Graphite	2750	300 (0.3)
5	1	Graphite	2000	300 (0.3)
6	2	Graphite	3500	300 (0.3)
7	2	Graphite	3500	300 (0.3)
8	2	Silica Phenolic	3500	300 (0.3)
9	2	Graphite Phenolic	3500	300 (0.3)
10	2	Graphite	3500	175 (0.4)
11	2	Graphite	2750	300 (0.3)
12	2	Silica Phenolic	2750	300 (0.3)
13	2	Graphite Phenolic	2750	300 (0.3)
14	2	Graphite	2000	300 (0.3)
15	2	Silica Phenolic	2000	300 (0.3)
16	2	Graphite Phenolic	2000	300 (0.3)
17	3	Graphite	3500	300 (0.3)
18	3	Graphite	3500	300 (0.3)
19	3	Silica Phenolic	3500	300 (0.3)
20	3	Graphite Phenolic	3500	300 (0.3)
21	3	Graphite	3500	175 (0.4)
22	3	Graphite	2750	300 (0.3)
23	3	Silica Phenolic	2750	300 (0.3)
24	3	Graphite Phenolic	2750	300 (0.3)
25	3	Graphite	2000	300 (0.3)
26	3	Silica Phenolic	2000	300 (0.3)
27	3	Graphite Phenolic	2000	300 (0.3)
28	4	Graphite	3500	300 (0.3)

TABLE IV.- CONCLUDED

Test Point	Mixture	Material	Total Temperature ( $^{\circ}$ K)	Plenum Pressure (psia)
29	4	Graphite	3500	300 (0.3)
30	4	Silica Phenolic	3500	300 (0.3)
31	4	Graphite Phenolic	3500	300 (0.3)
32	4	Graphite	3500	175 (0.4)
33	4	Graphite	2750	300 (0.3)
34	4	Silica Phenolic	2750	300 (0.3)
35	4	Graphite Phenolic	2750	300 (0.3)
36	4	Graphite	2000	300 (0.3)
37	4	Silica Phenolic	2000	300 (0.3)
38	4	Graphite Phenolic	2000	300 (0.3)
39	5	Graphite	3500	300 (0.3)
40	5	Graphite	3500	300 (0.3)
41	5	Silica Phenolic	3500	300 (0.3)
42	5	Graphite Phenolic	3500	300 (0.3)
43	5	Graphite	3500	175 (0.4)
44	5	Graphite	2750	300 (0.3)
45	5	Silica Phenolic	2750	300 (0.3)
46	5	Graphite Phenolic	2750	300 (0.3)
47	5	Graphite	2000	300 (0.3)
48	5	Silica Phenolic	2000	300 (0.3)
49	5	Graphite Phenolic	2000	300 (0.3)
50	Conditions as found desirable or necessary from other test results			
51				
52				
53				
54				
55				
56				

\*Test nozzle throat diameter, inch.



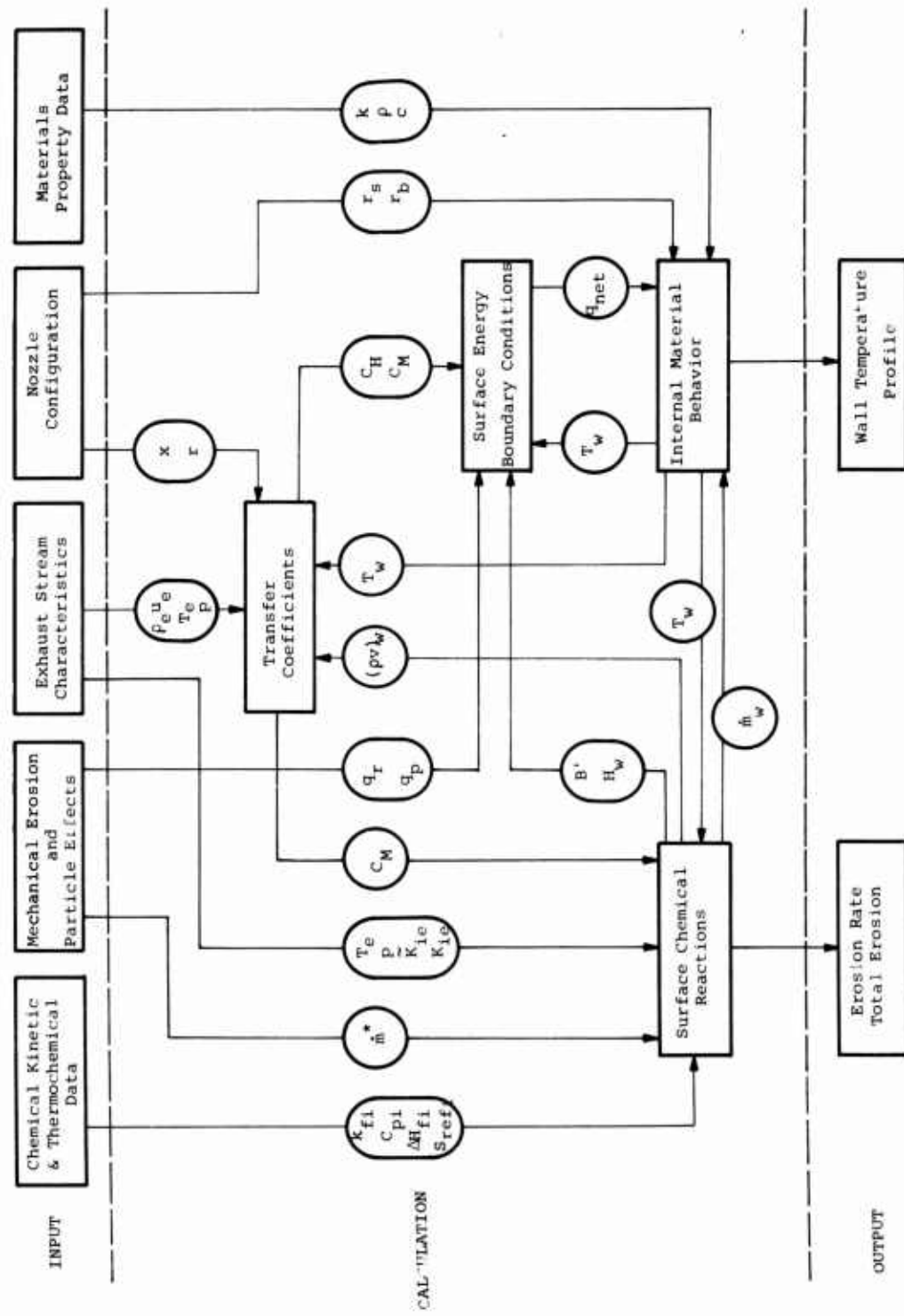


Figure 2.- Flow diagram of wall-erosion calculation.

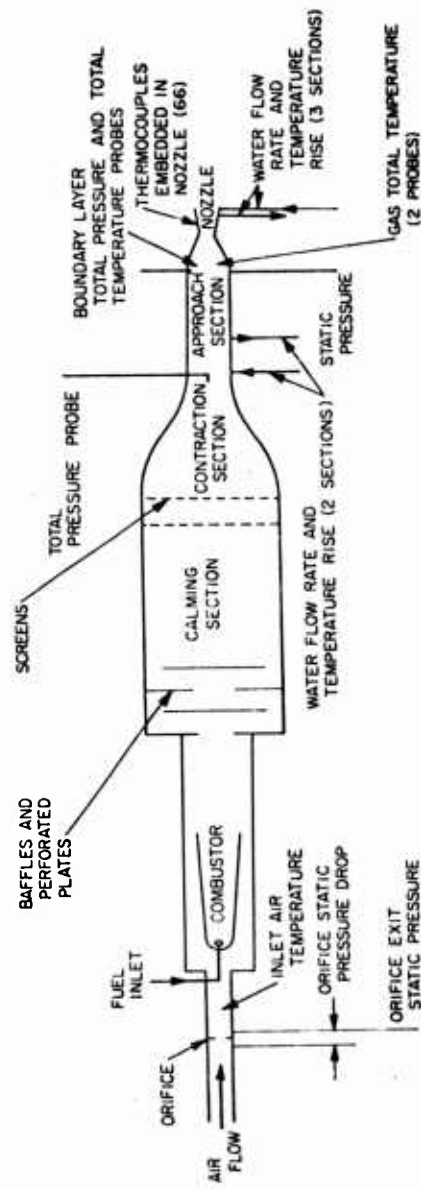


Figure 3.- Flow and instrumentation diagram (from Ref. 8).



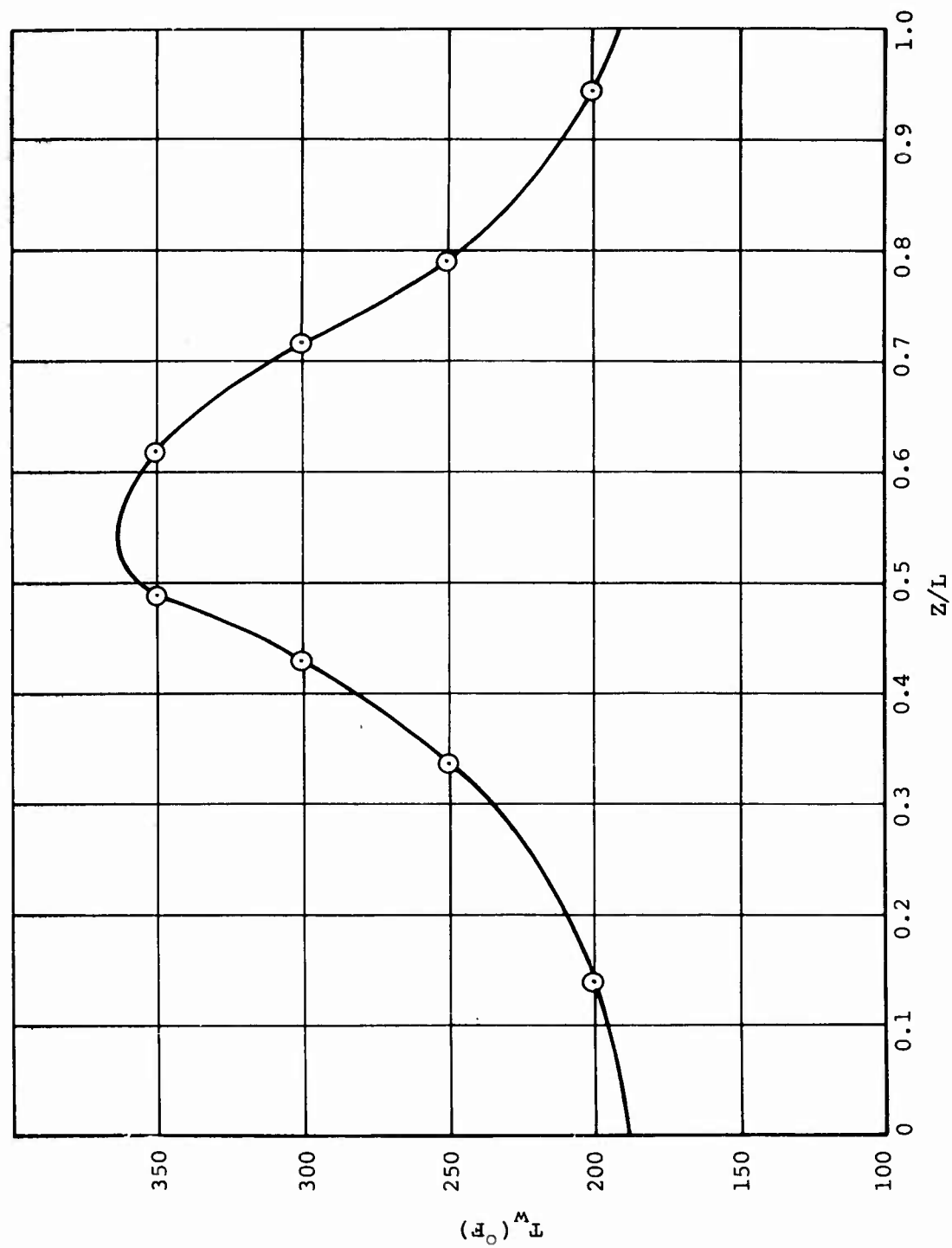


Figure 4.- Measured wall temperature axial distribution, JPL Test 218.

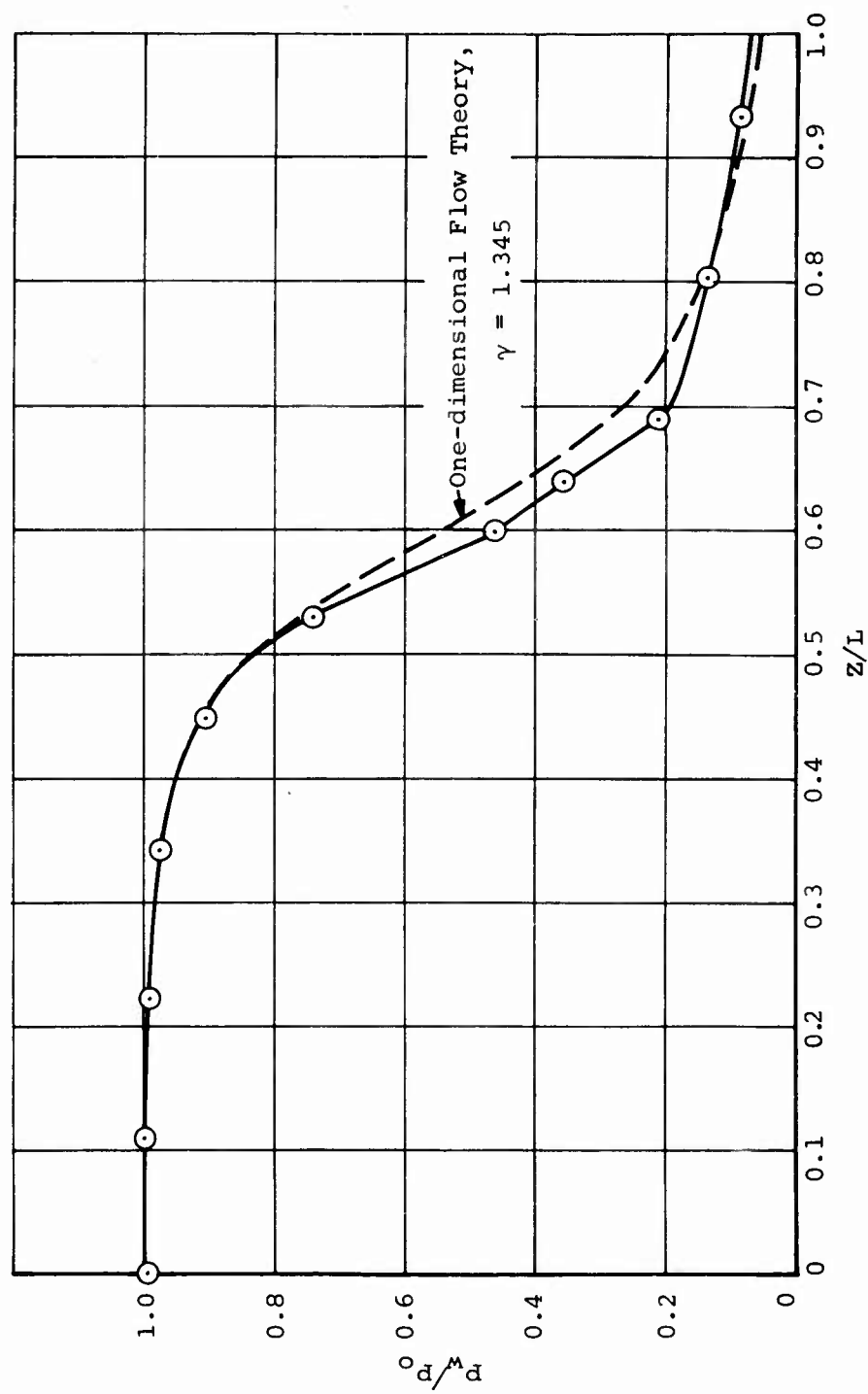


Figure 5.- Measured wall pressure axial distribution, JPL Test 218.

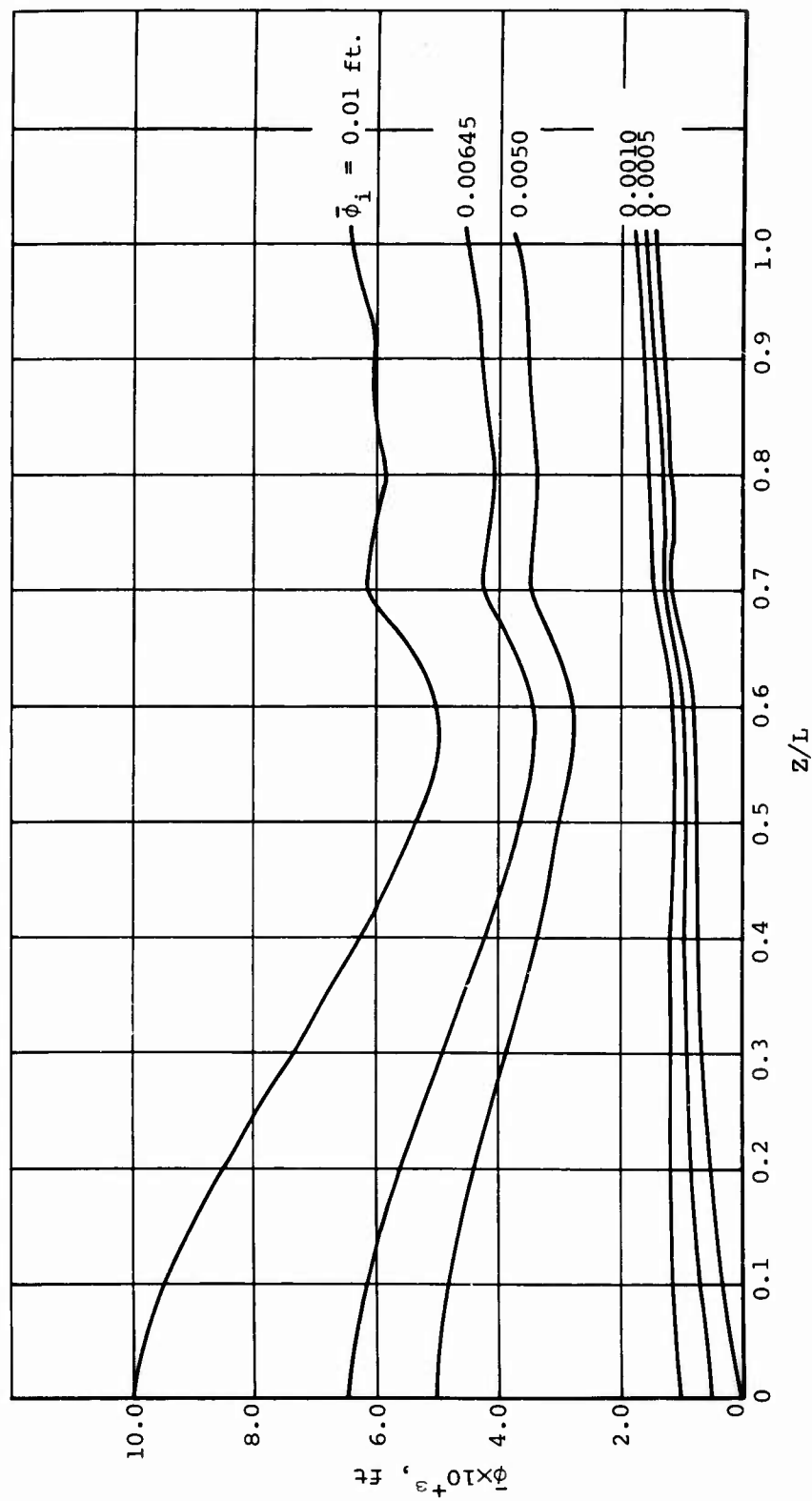


Figure 6.- Calculated energy thickness axial distribution.

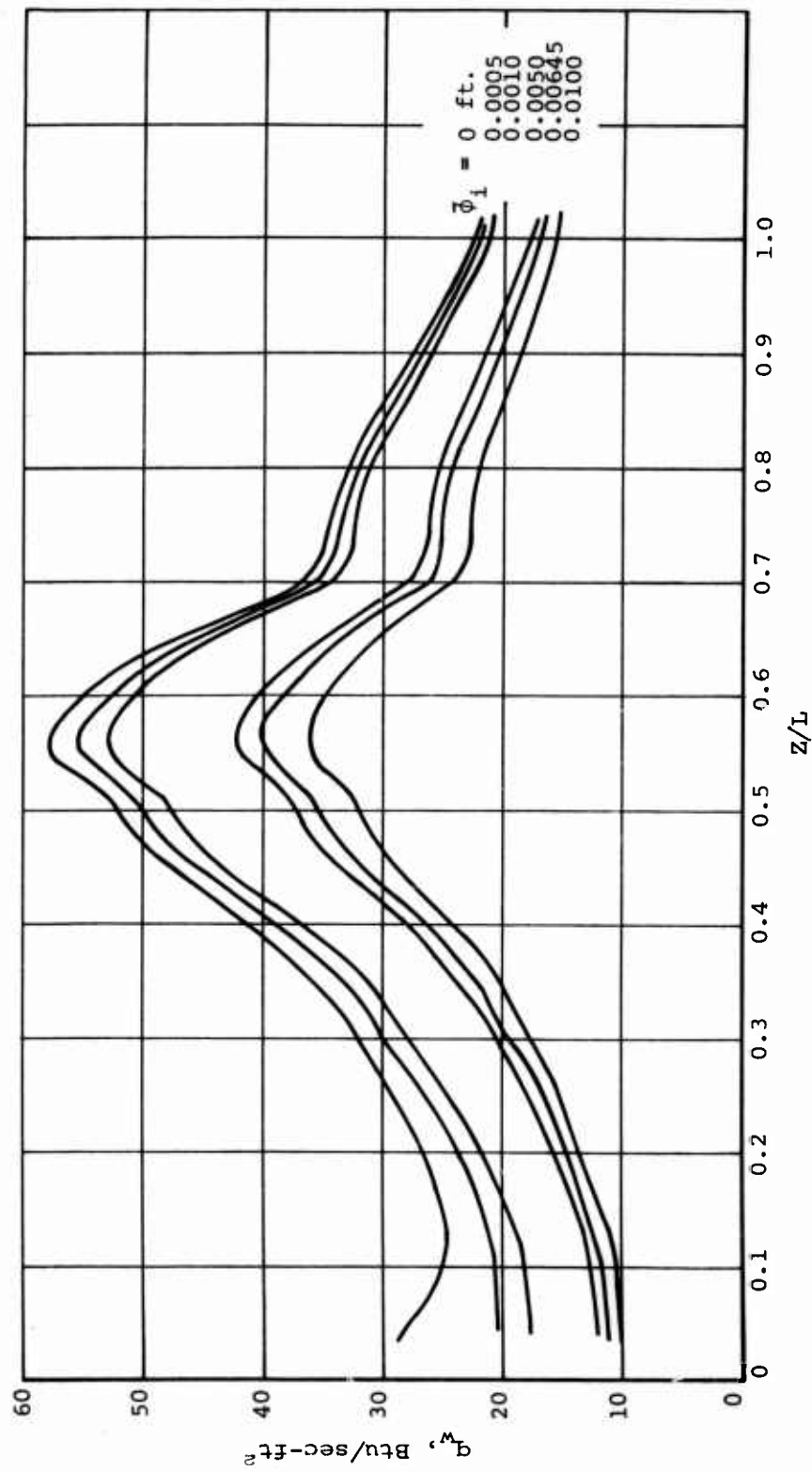


Figure 7.- Calculated wall heat flux axial distribution.

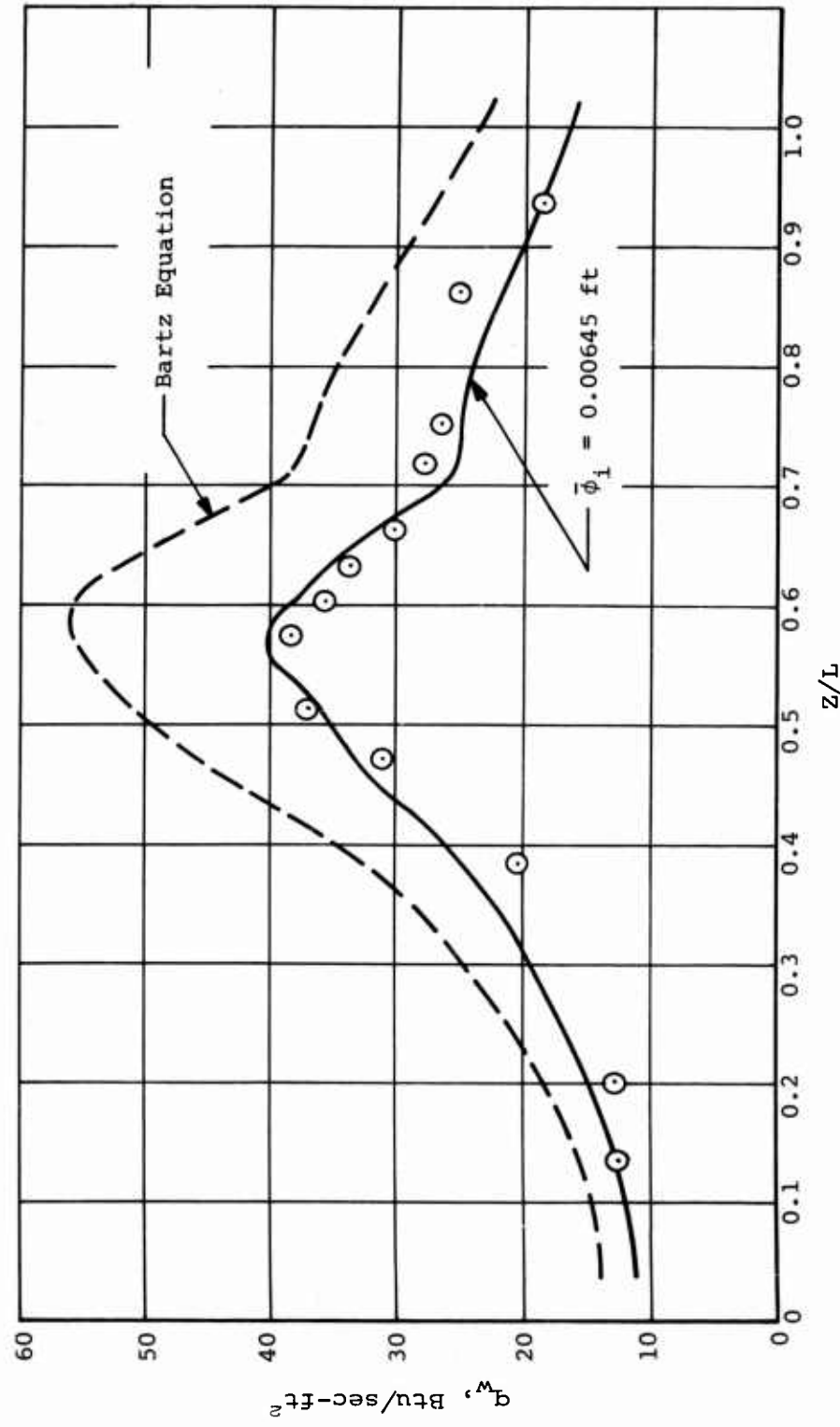


Figure 8.- Comparison of results with experimental data, JPL, Test 218.

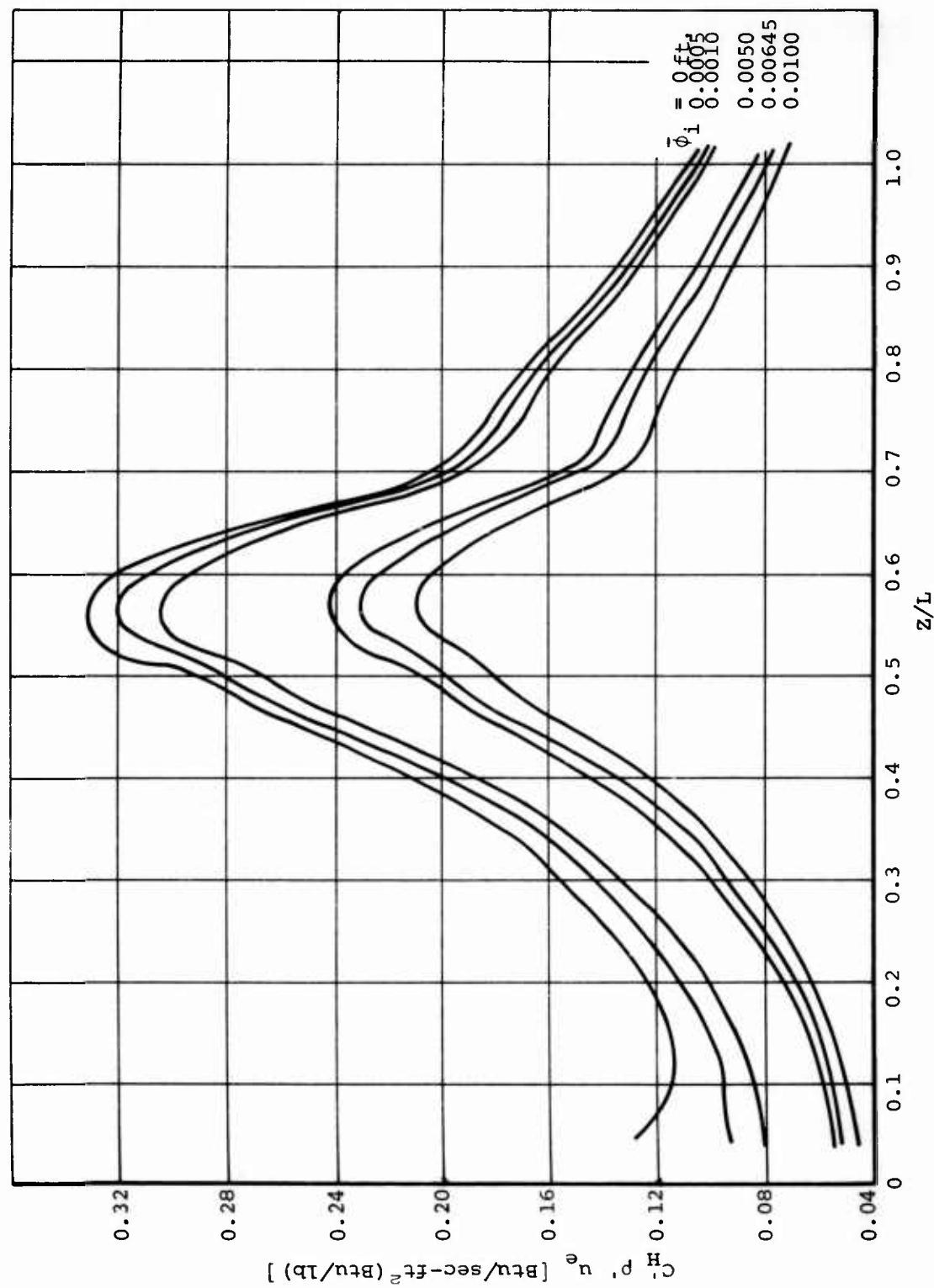


Figure 9.- Calculated enthalpy heat transfer coefficient axial distribution.

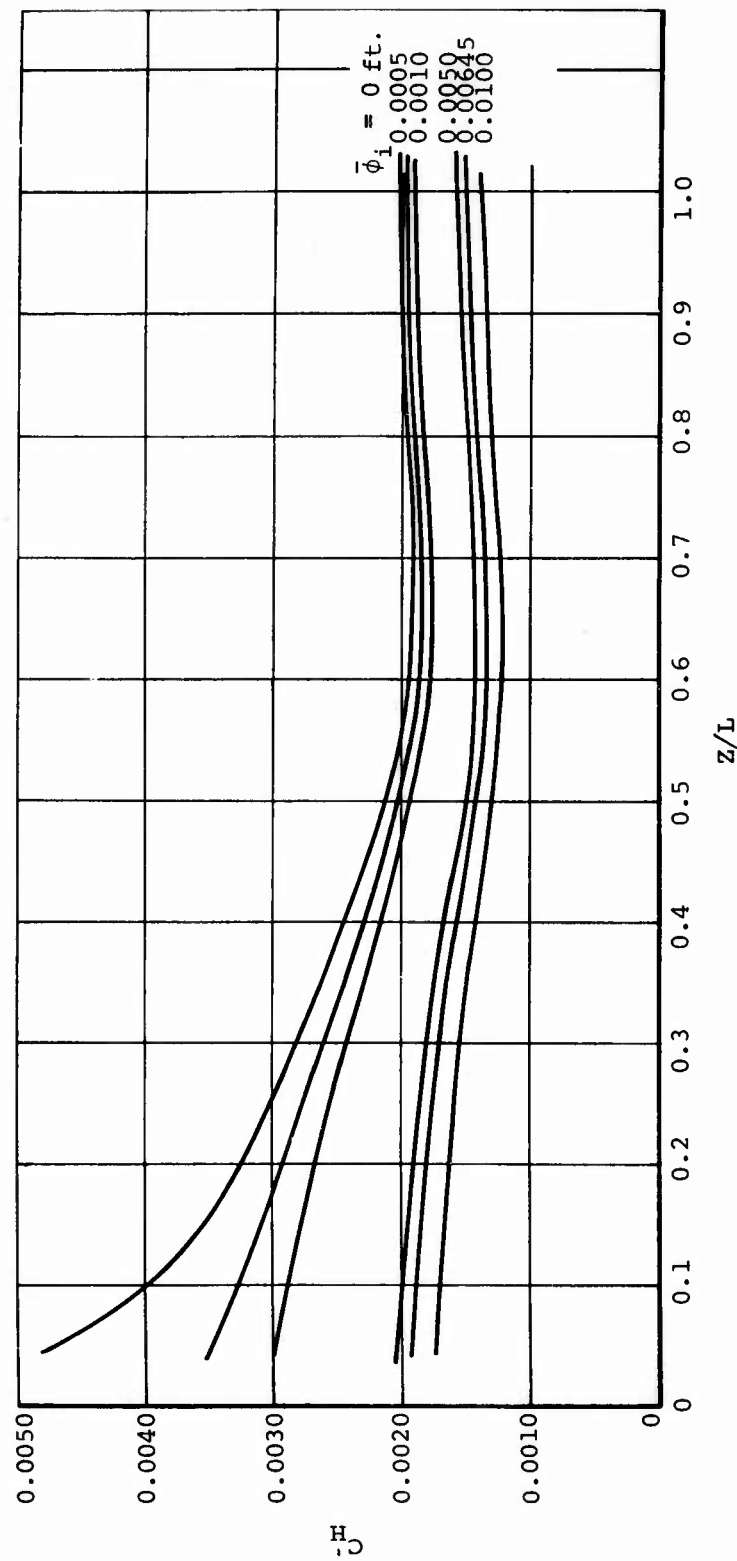


Figure 10.- Calculated Stanton number axial distribution.

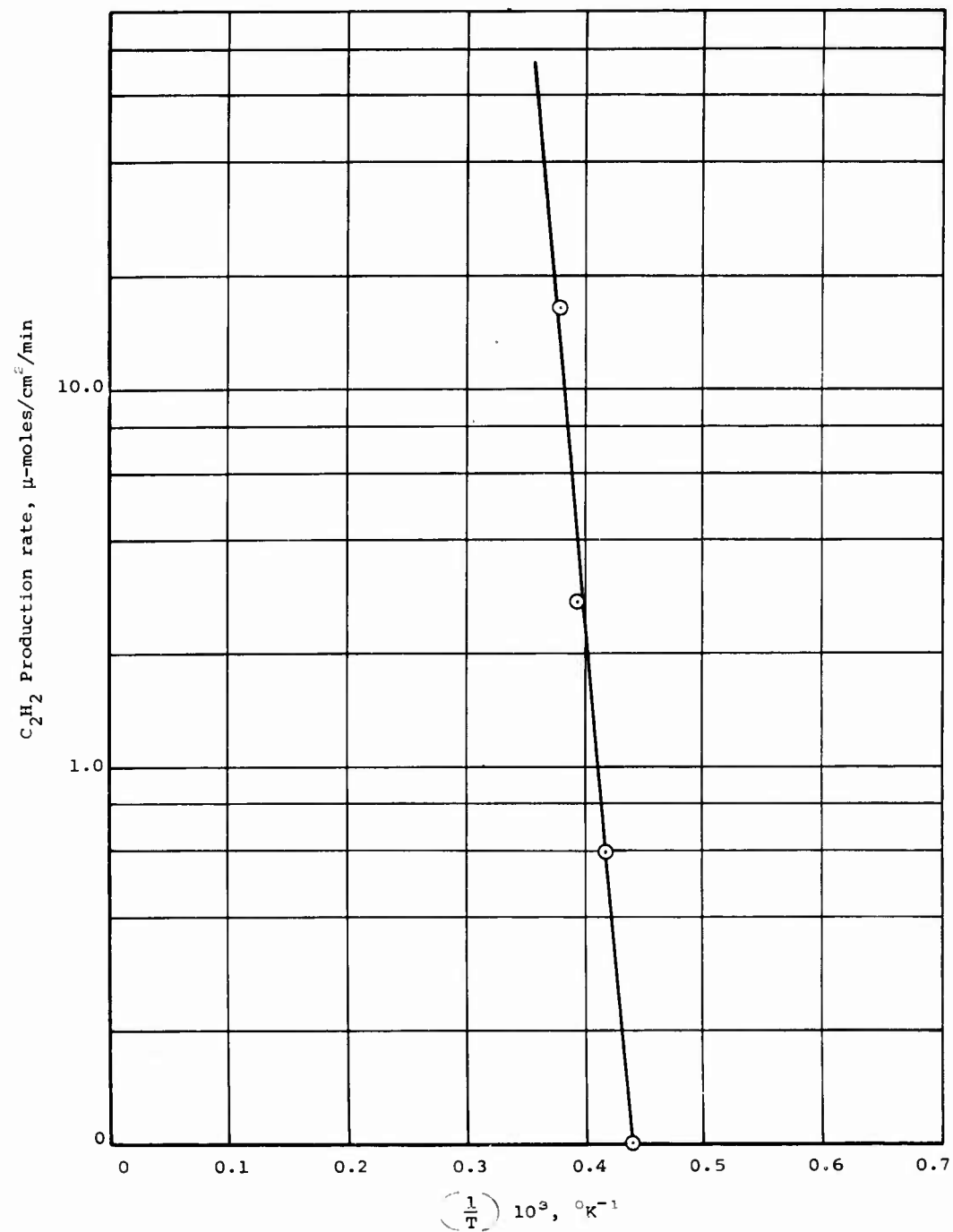


Figure 11.- Reaction rate data for hydrogen on graphite.



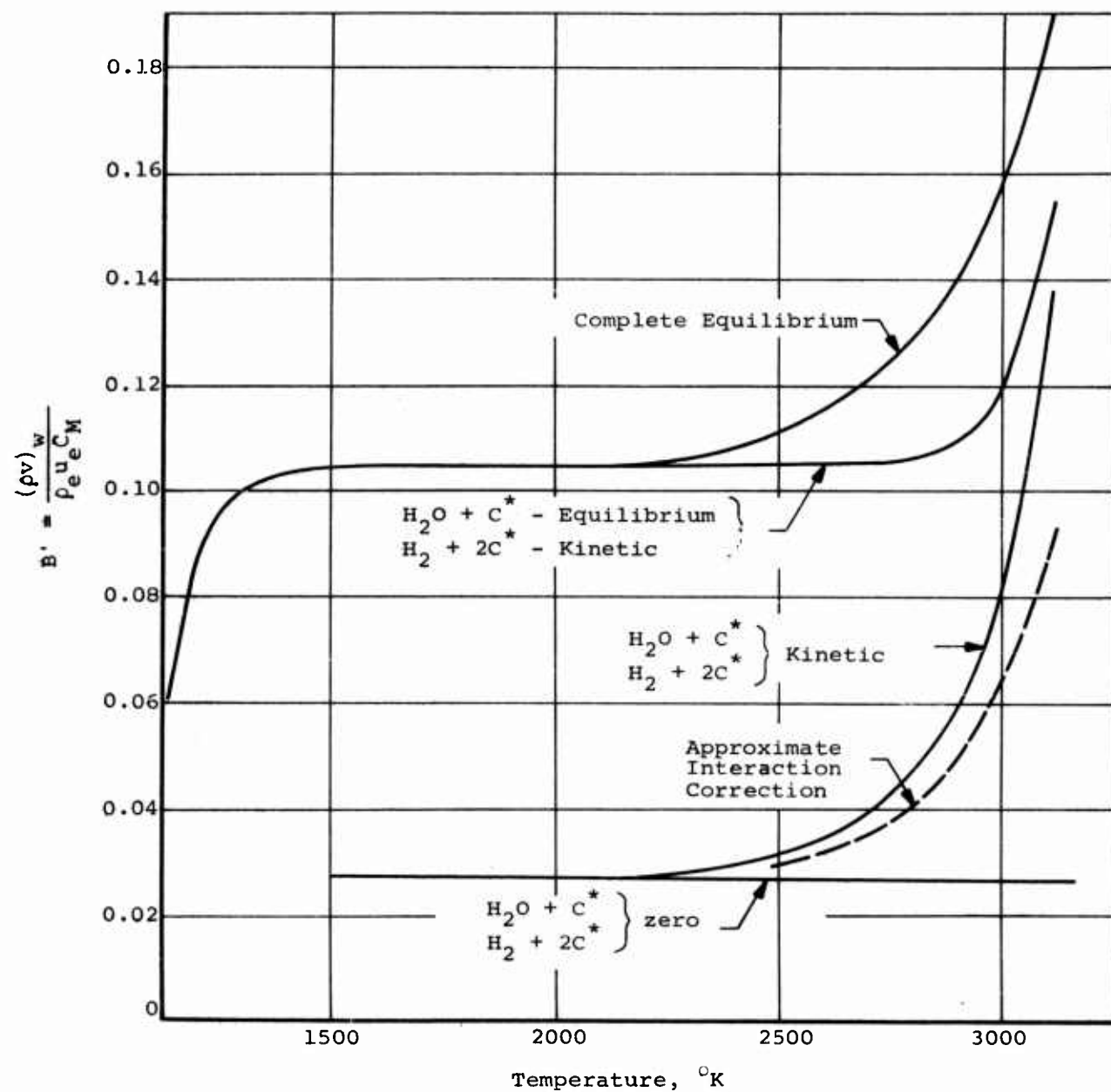


Figure 12.- Predicted graphite wall erosion in H, C, N, O, and Cl exhaust.

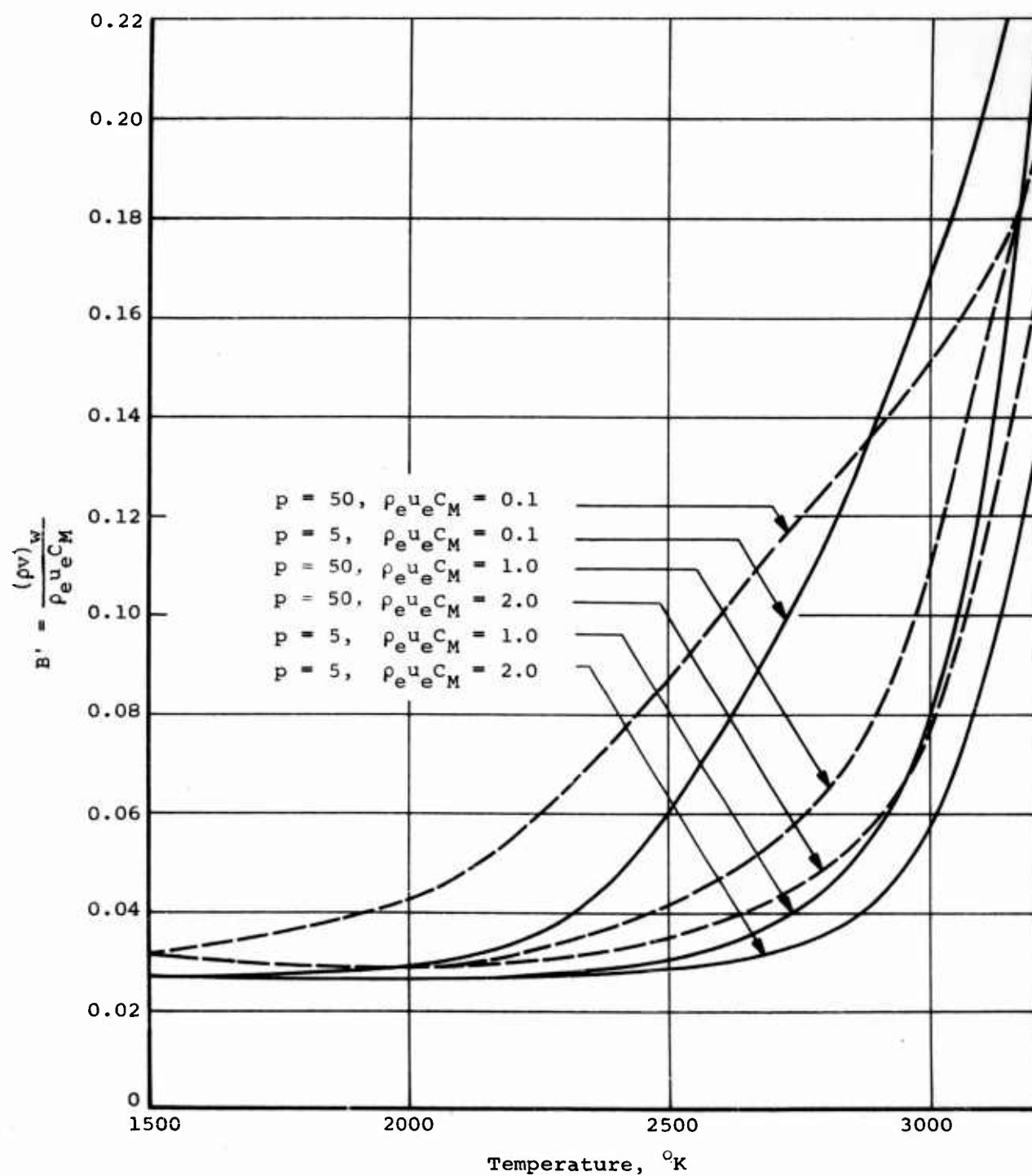


Figure 13.- Pressure and mass transfer effects on predicted chemical erosion of graphite in H, C, N, O, and Cl exhaust.

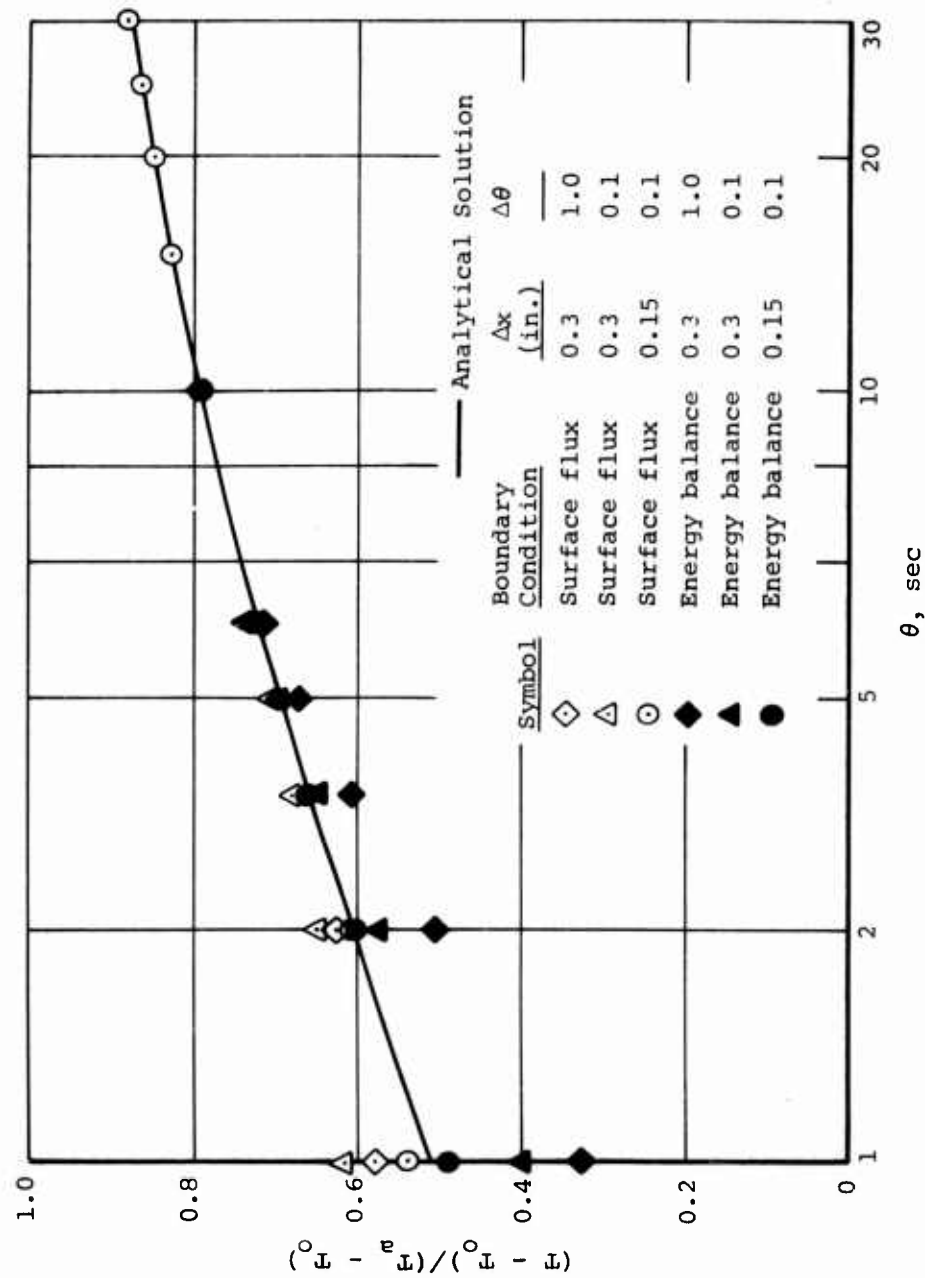


Figure 14.- Surface temperature for transient heat conduction in a slab.

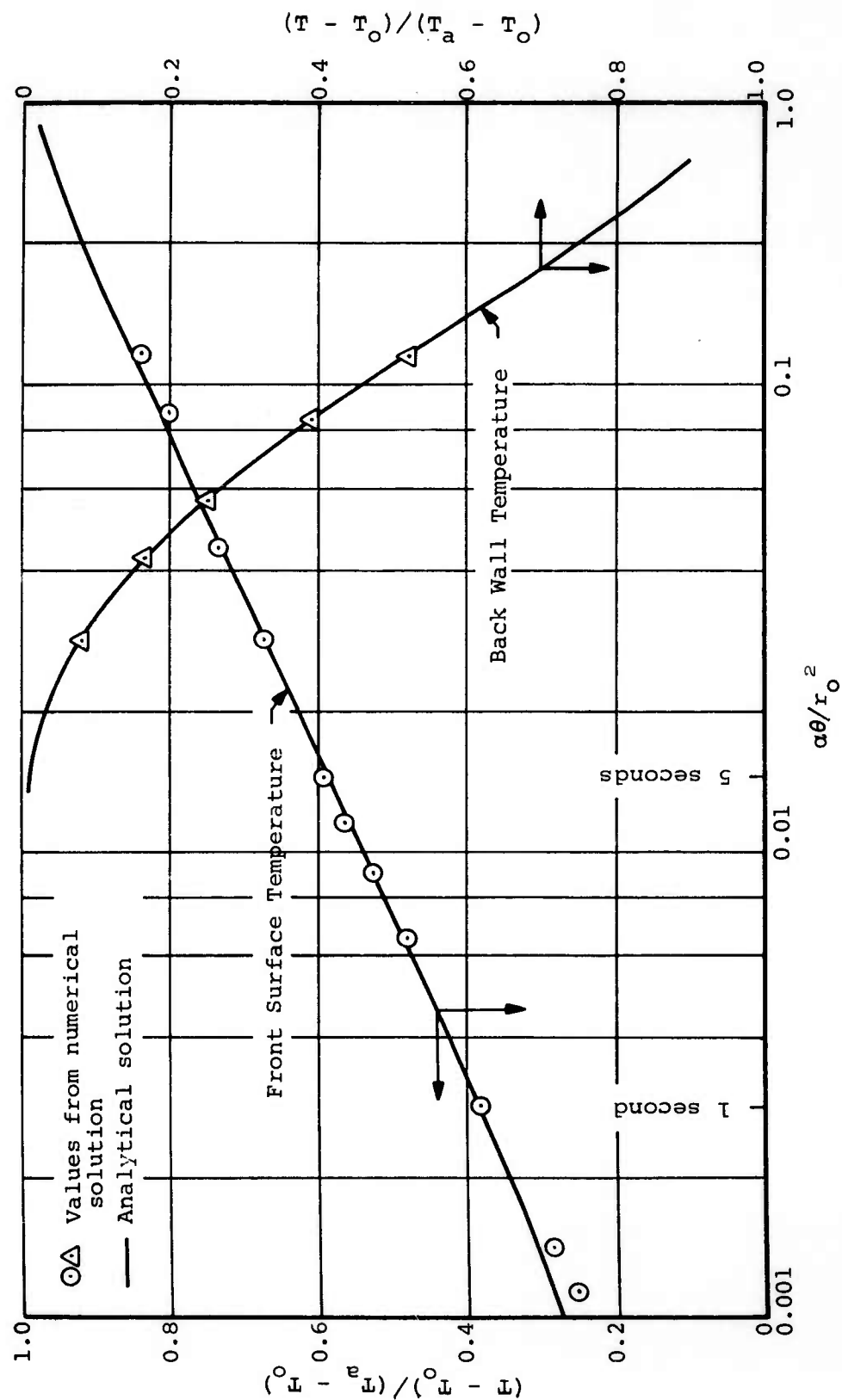
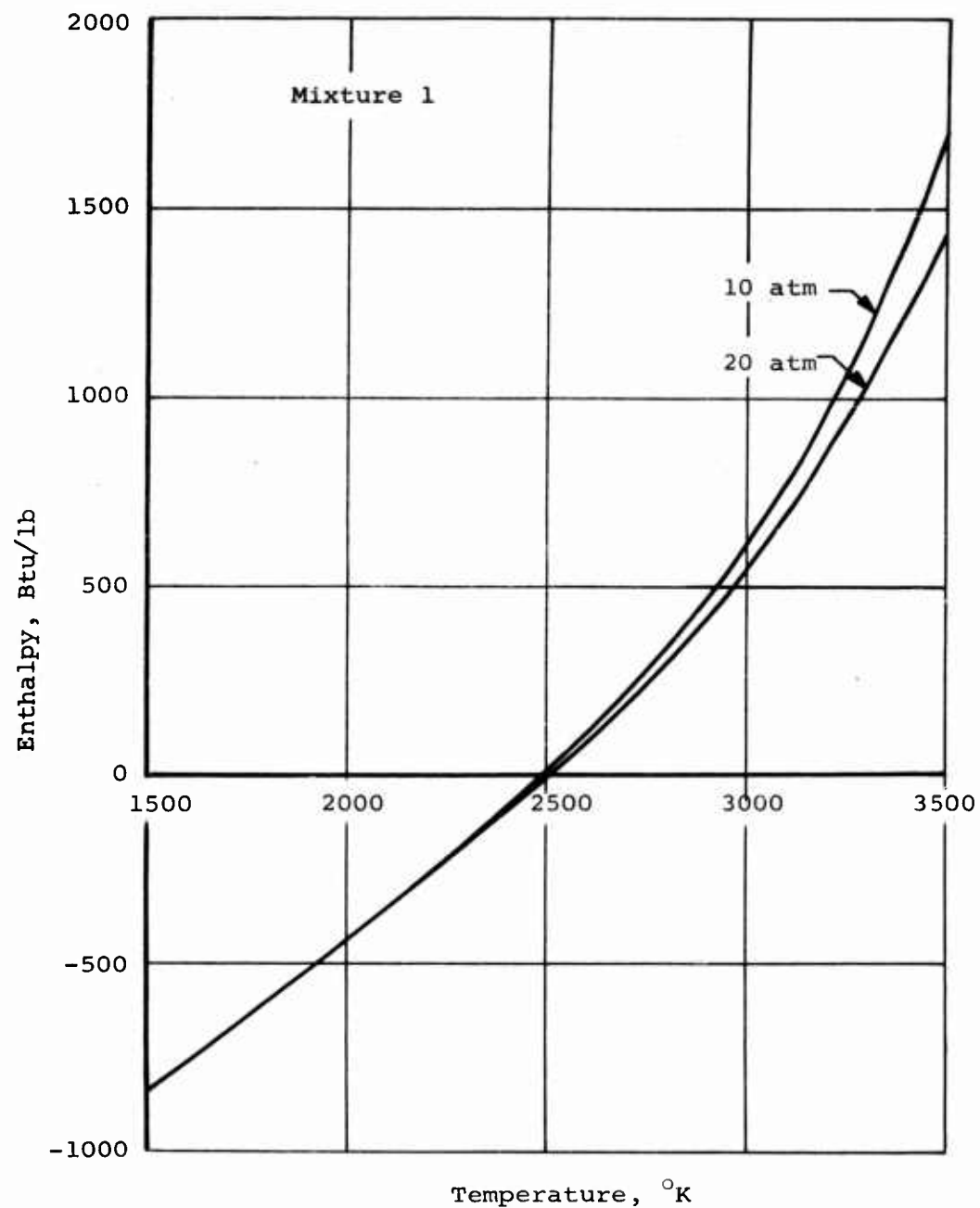
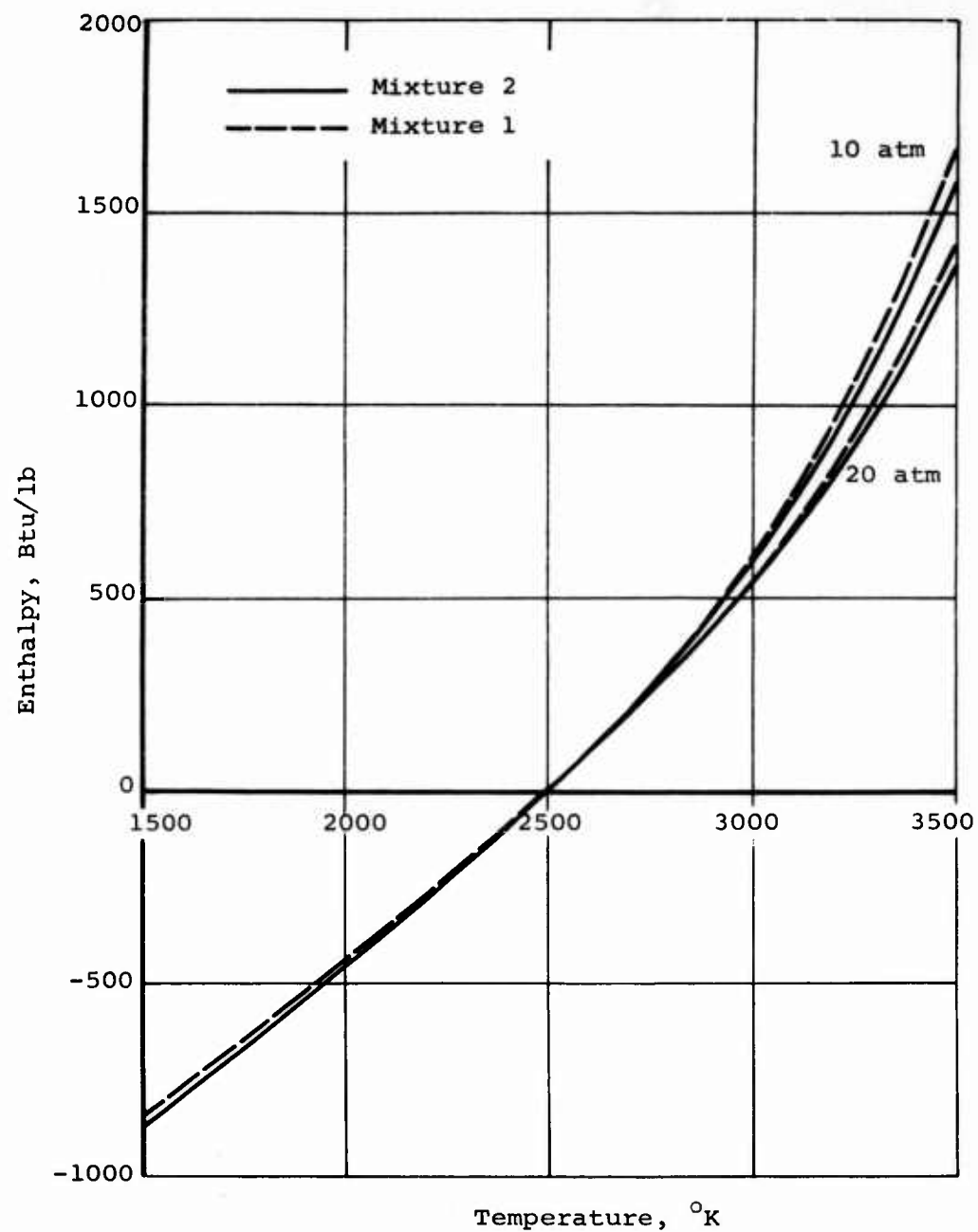


Figure 15.- Transient conduction in the hollow cylinder, back wall insulated,  $r_s/r_o = 0.6$ .



(a) Mixture 1.

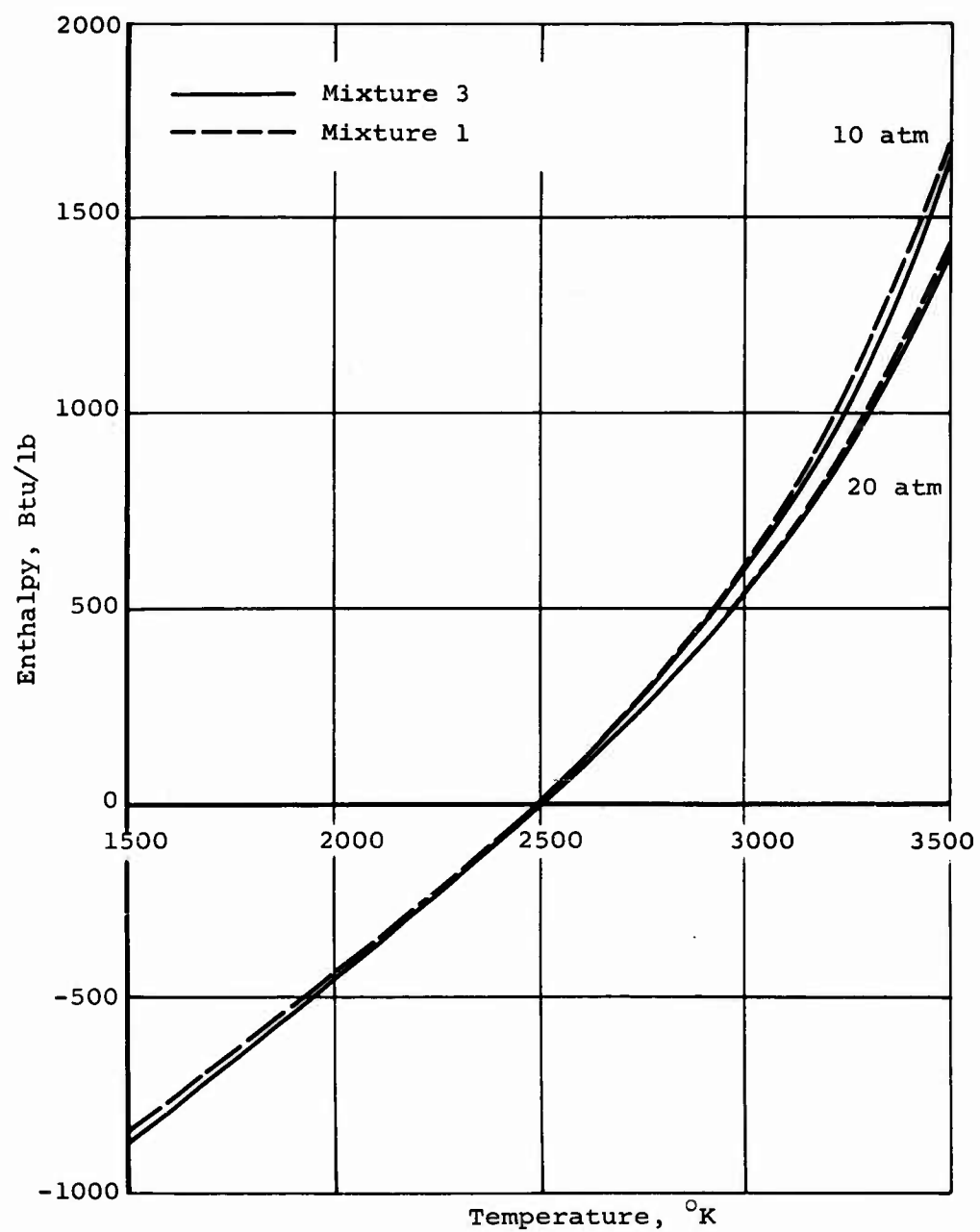
Figure 16.- Temperature enthalpy variation for test gas mixtures.



Temperature, °K

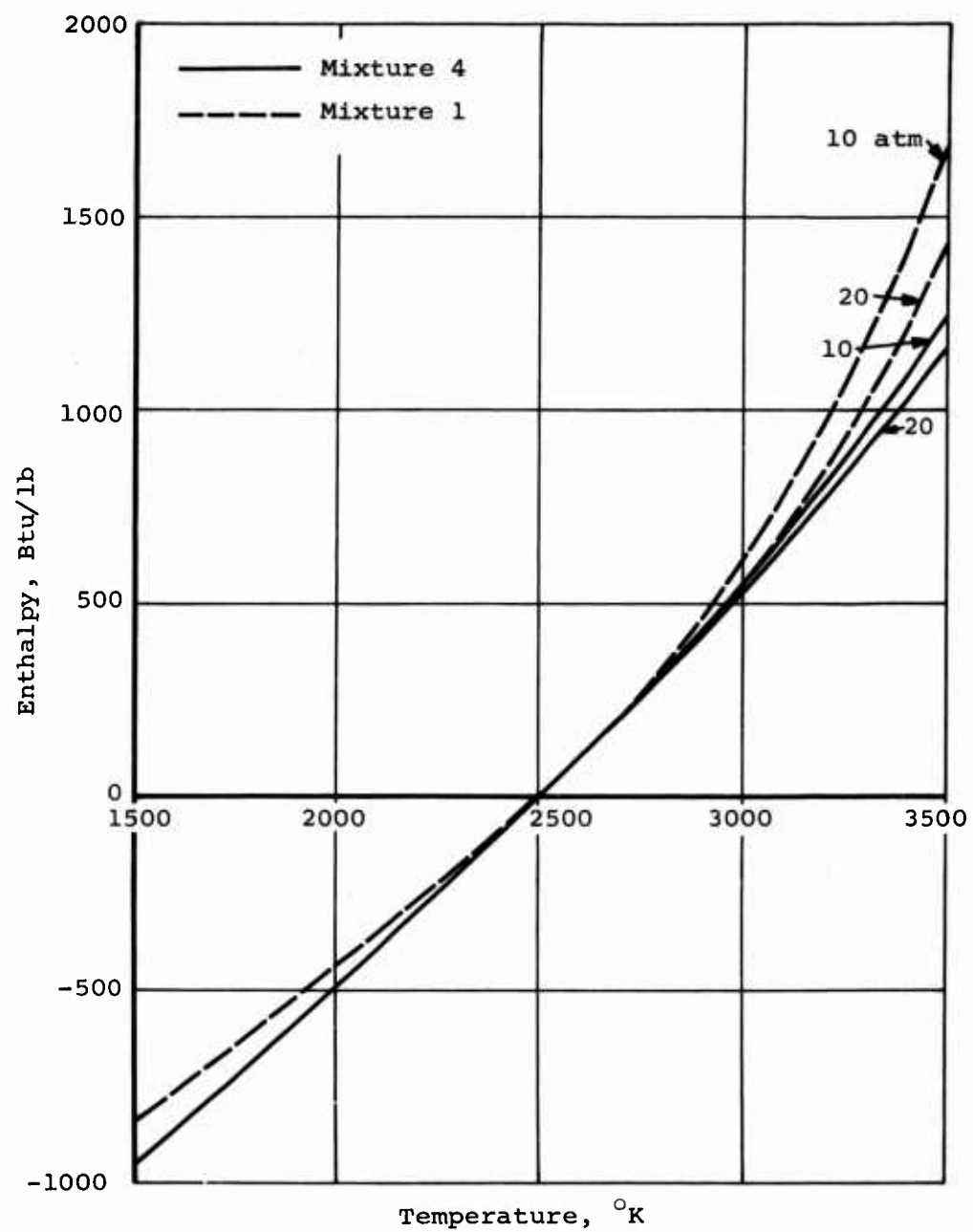
(b) Mixture 2.

Figure 16.- Continued



(c) Mixture 3.

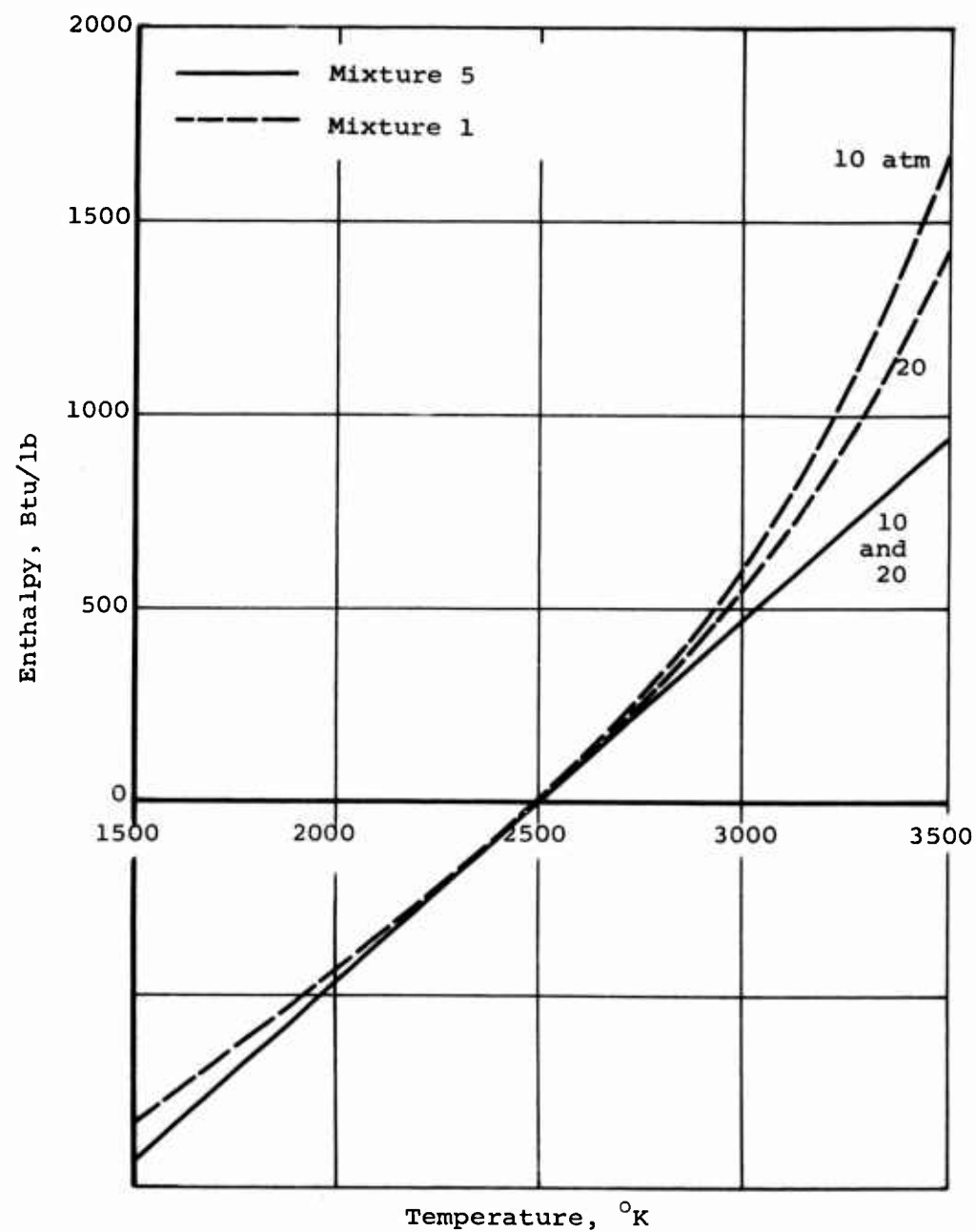
Figure 16.- Continued



(d) Mixture 4

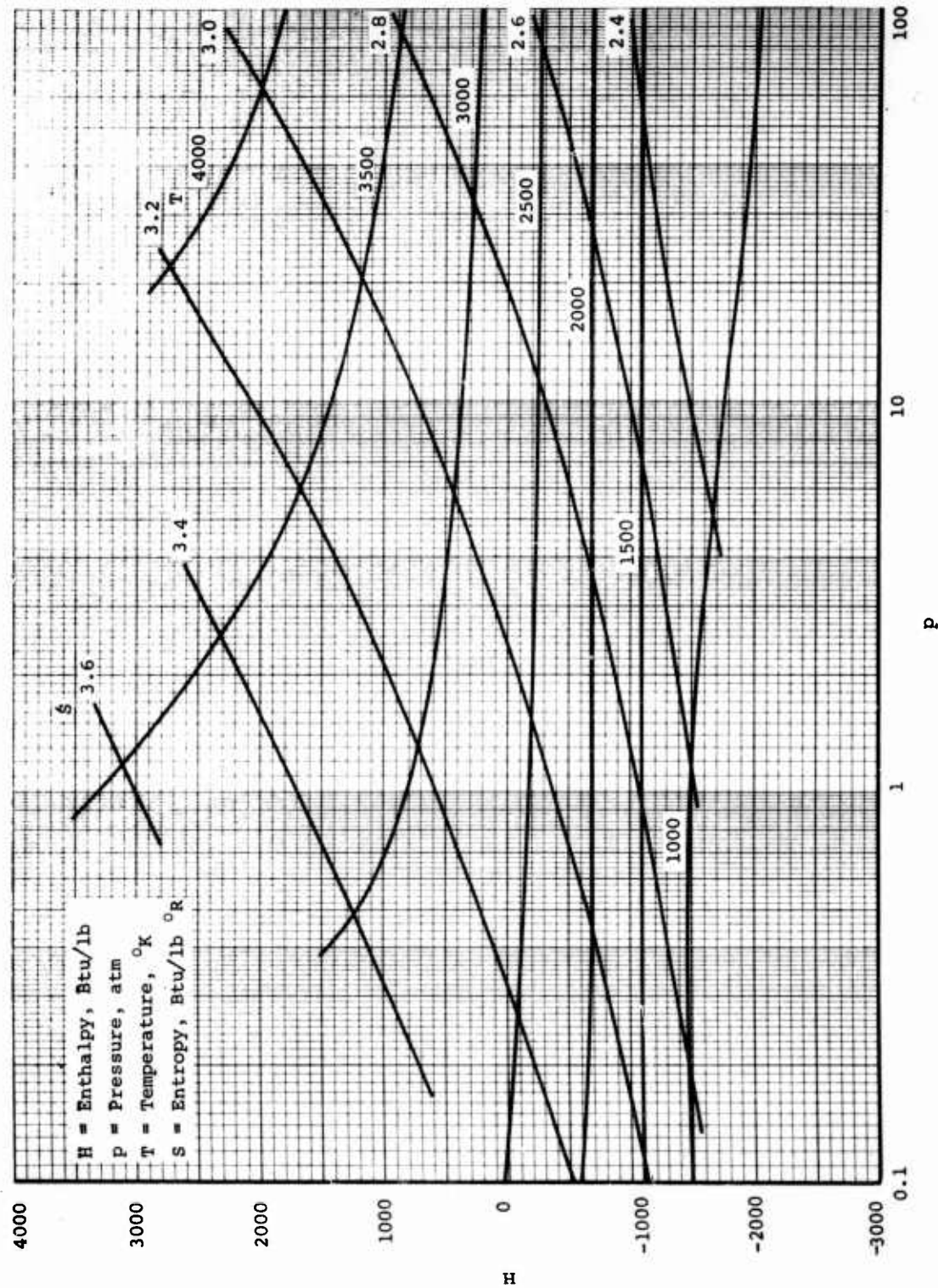
Figure 16.- Continued.





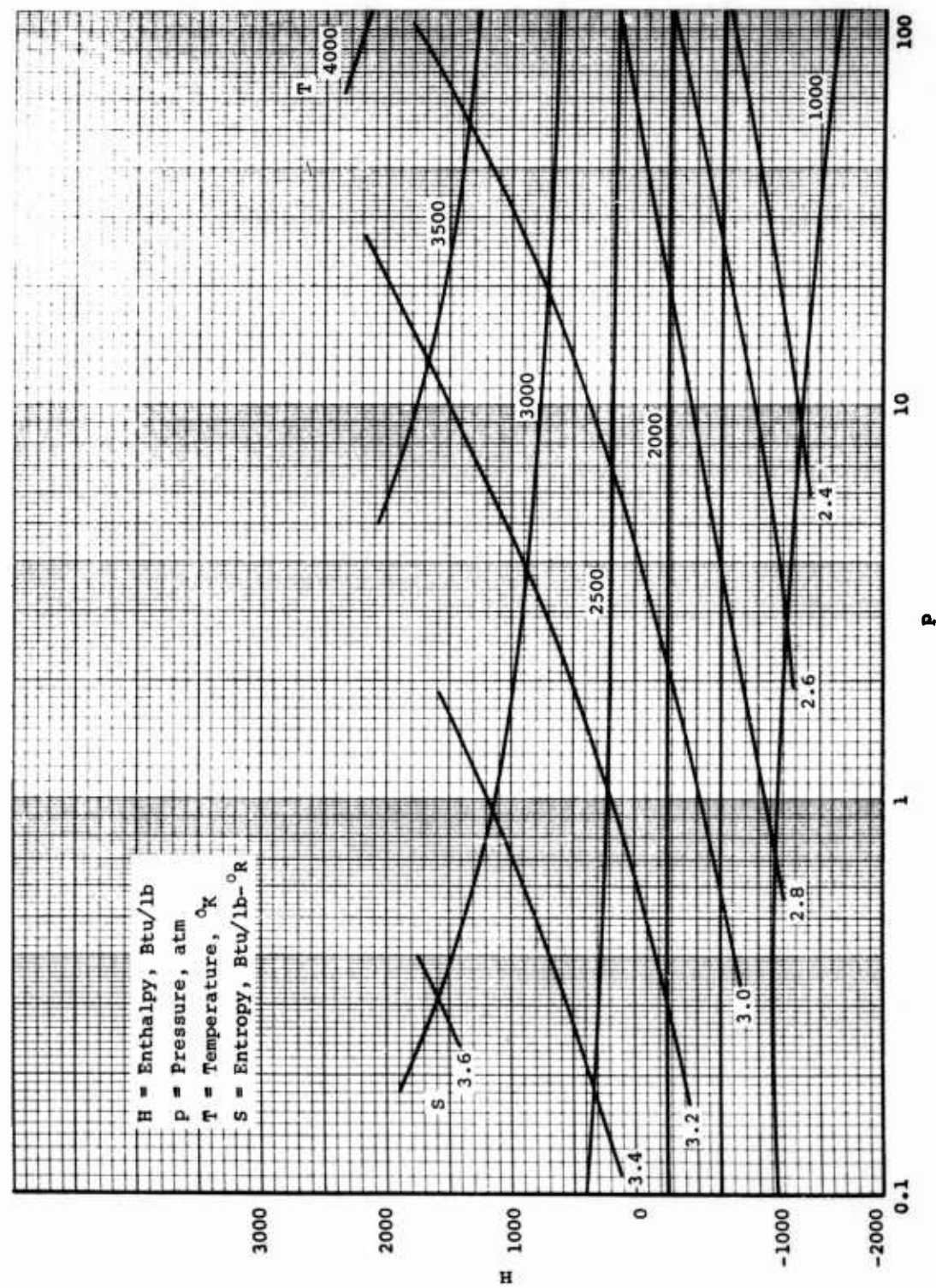
(e) Mixture 5.

Figure 16.- Concluded.



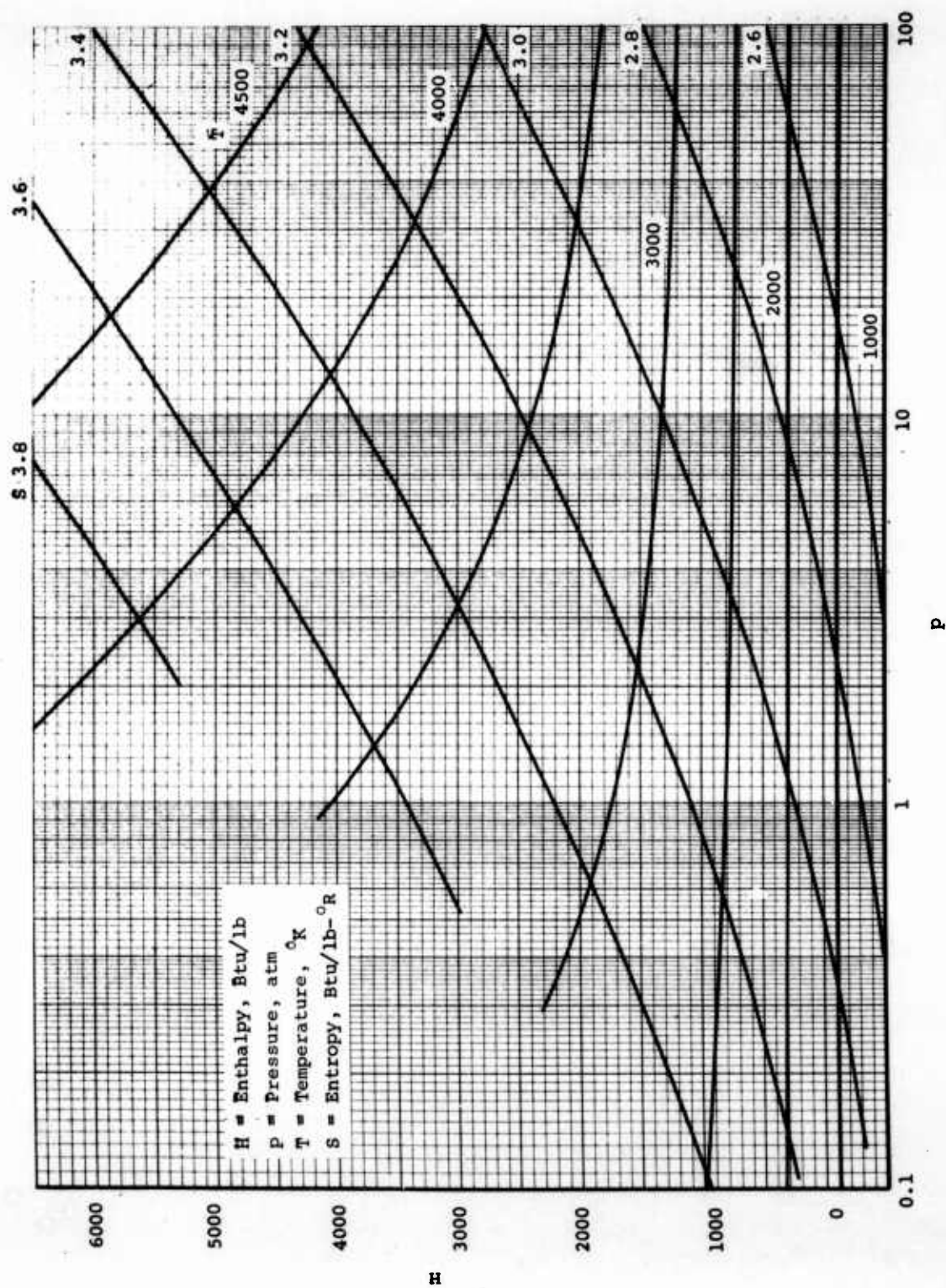
(a) Mixture 1.

Figure 17.- Master thermodynamic charts for test gas mixtures.



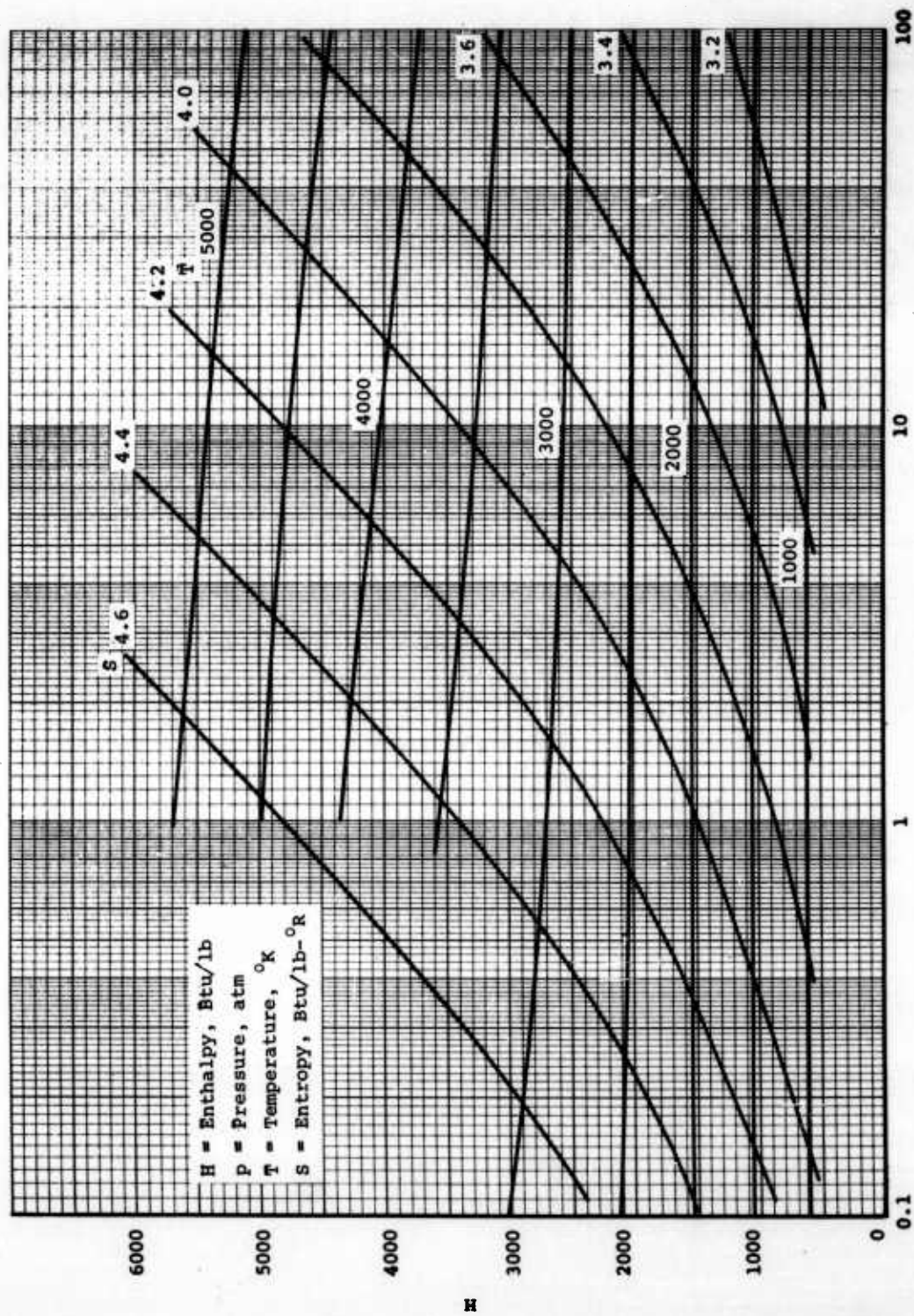
(b) Mixture 2.

Figure 17.- Continued.



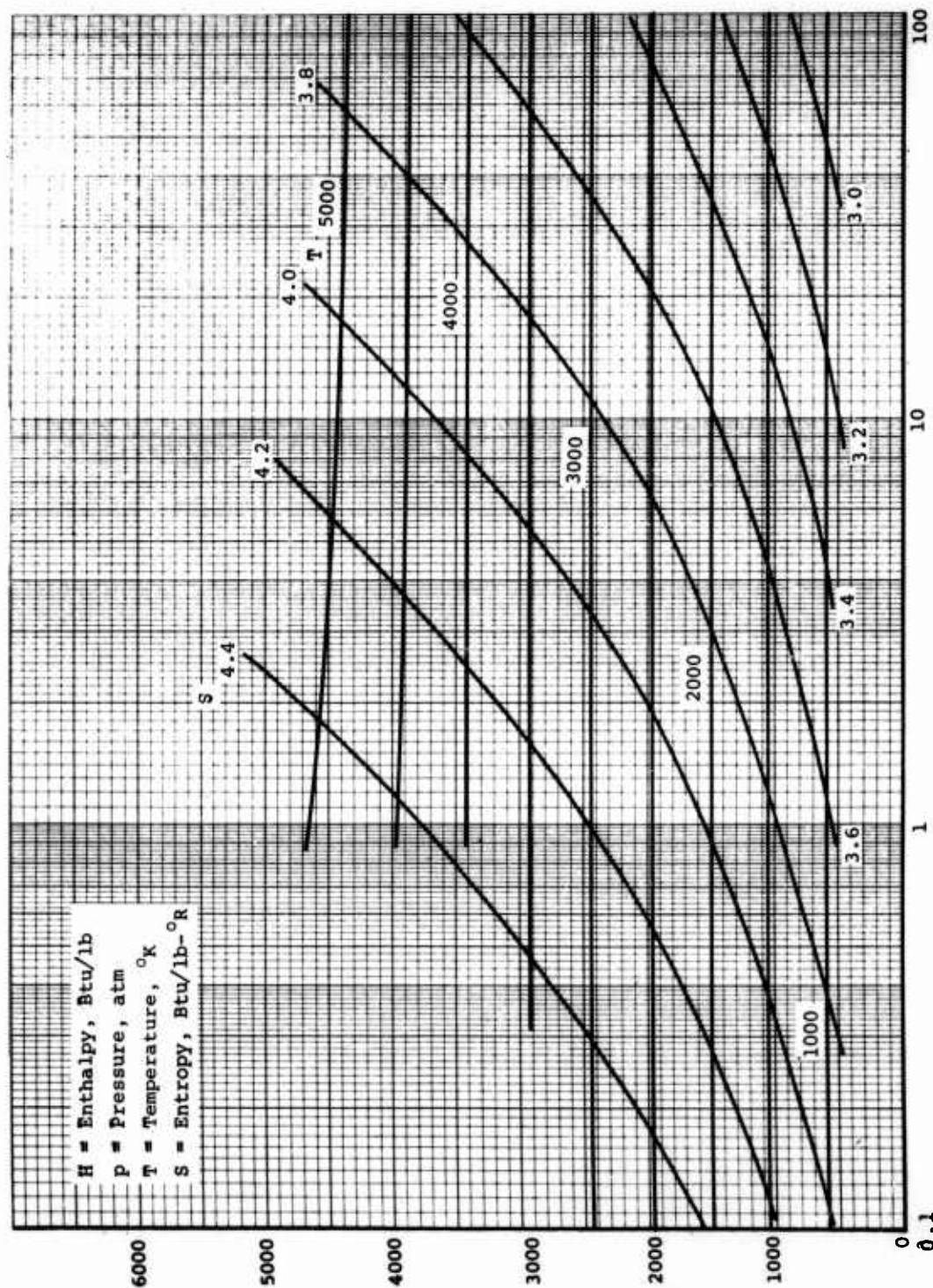
(c) Mixture 3.  
 Figure 17.- Continued.





(d) Mixture 4.

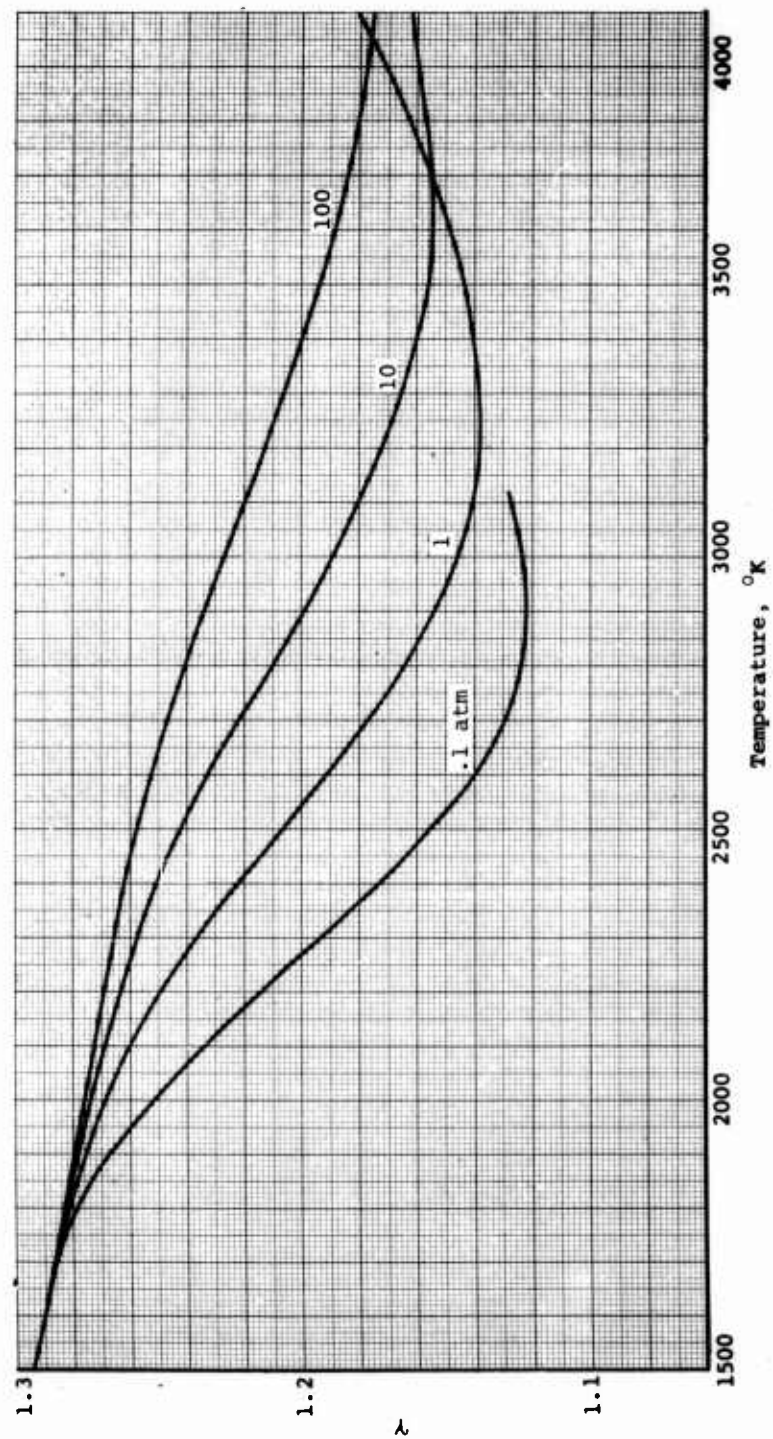
Figure 17.- Continued.



P

(e) Mixture 5.

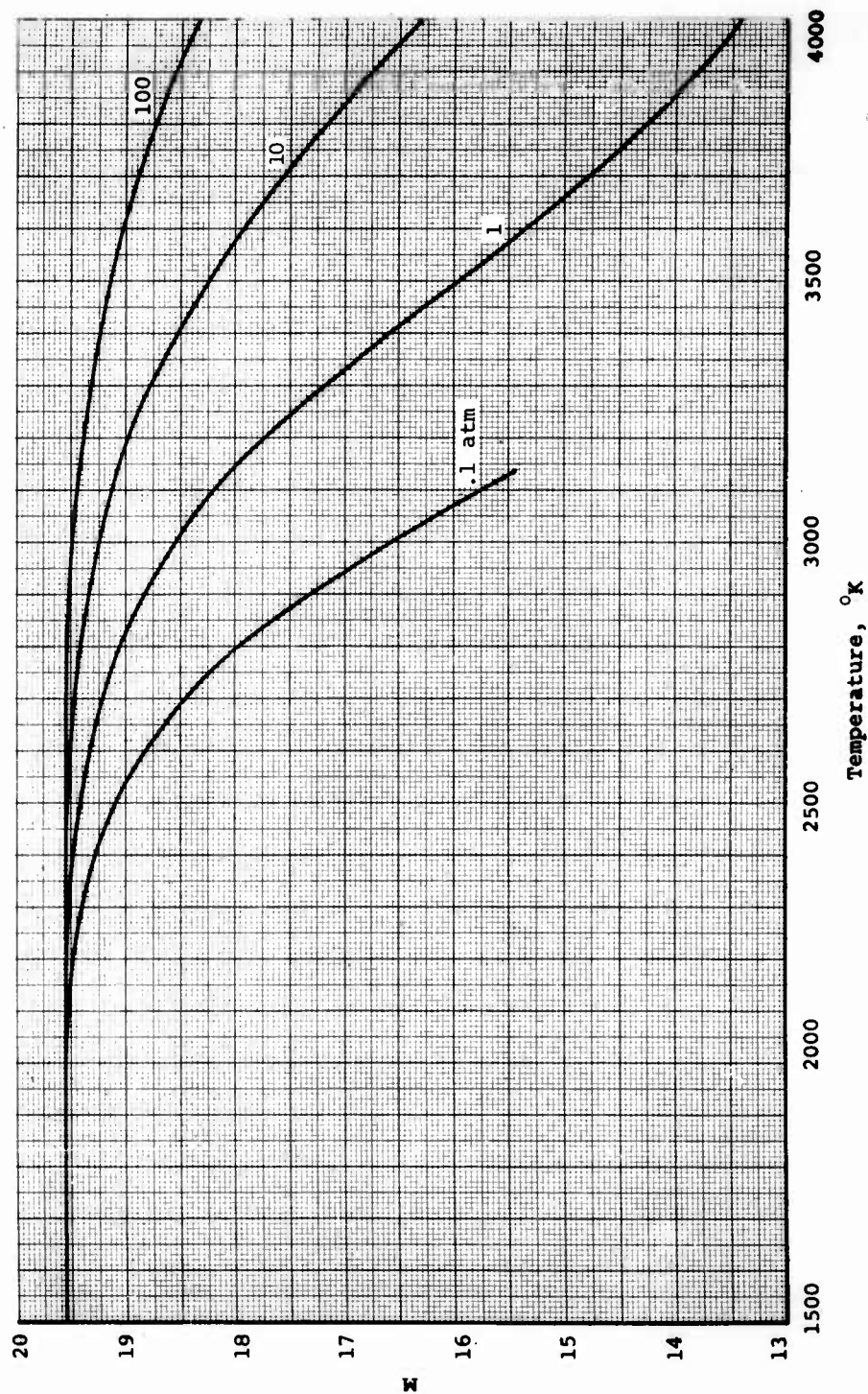
Figure 17.- Concluded.



(a) Isentropic exponent.

Figure 18.- Thermodynamic charts for mixture 3.

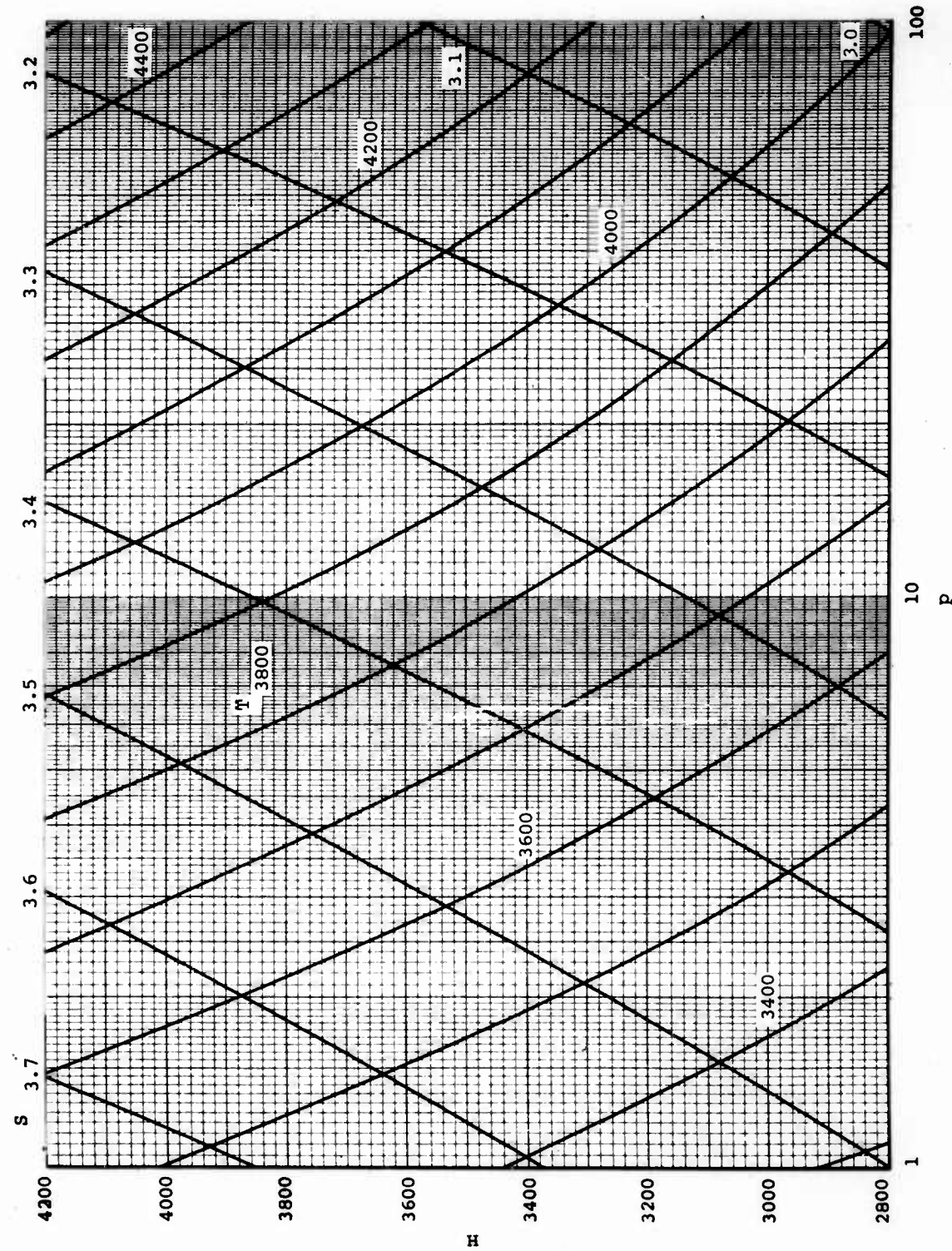




(b) Molecular weight.

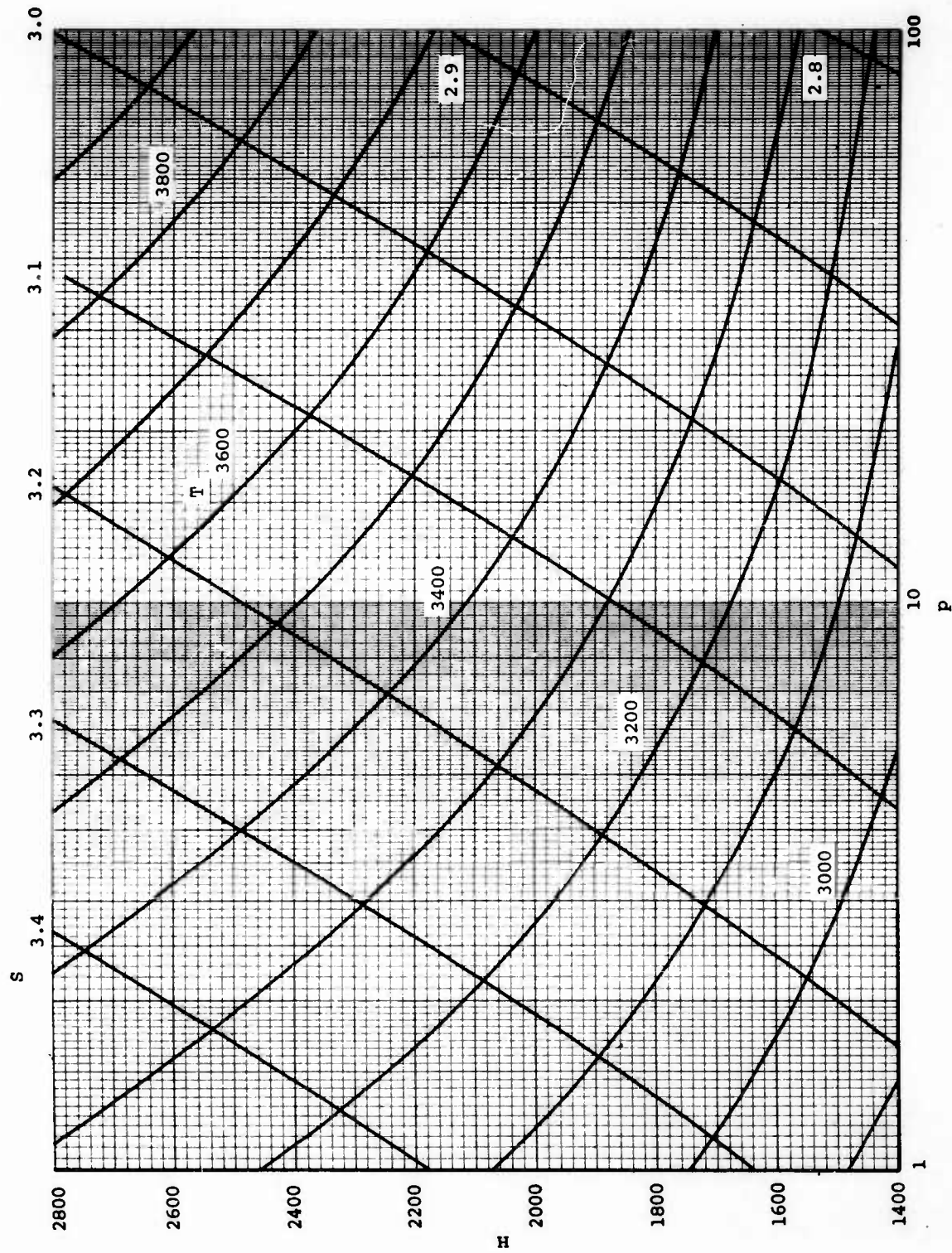
Figure 18.- Continued.





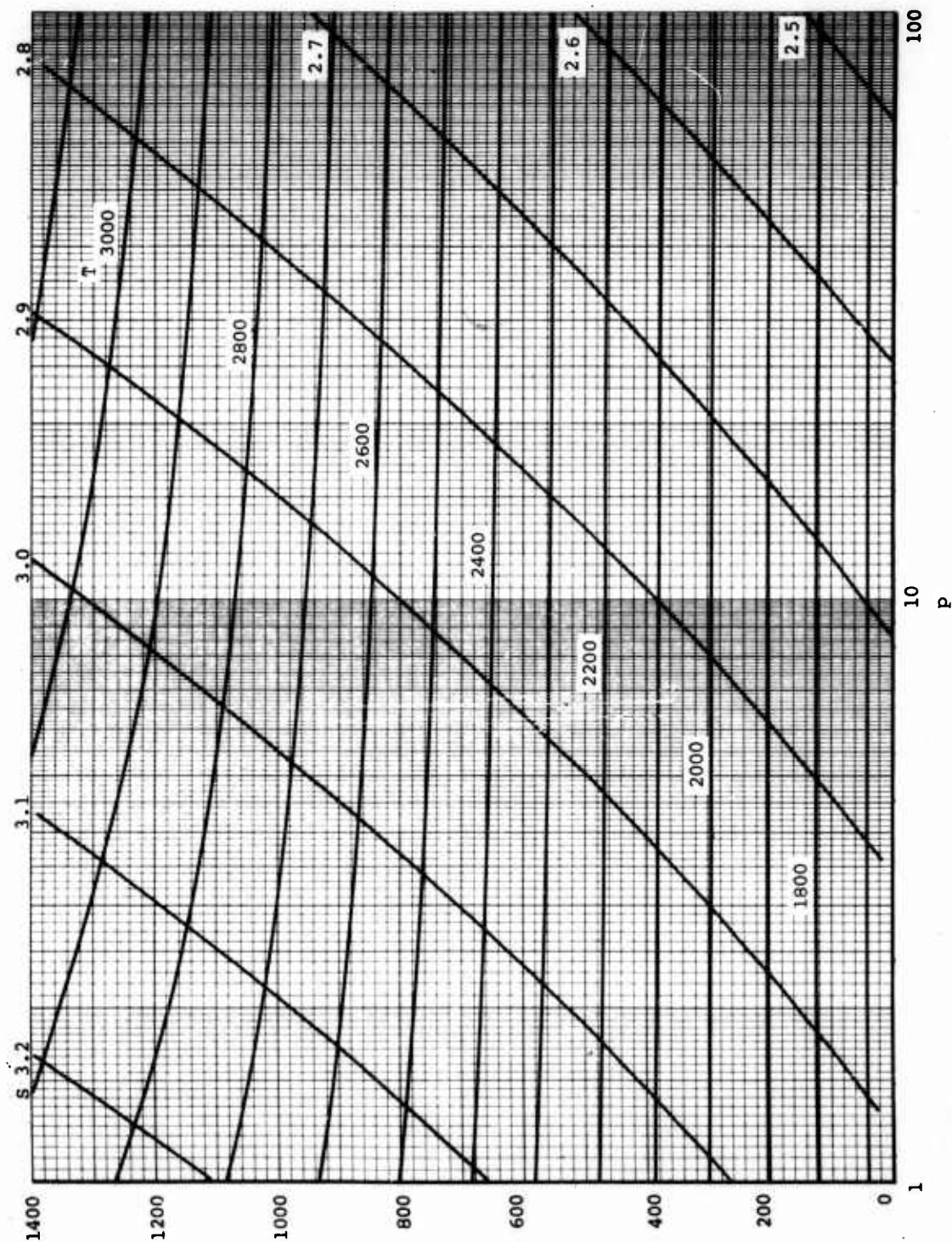
(c) Thermodynamic properties.

Figure 18.- Continued.



(c) Continued.

Figure 18.- Continued.



(c) Concluded.

Figure 18.- Concluded.

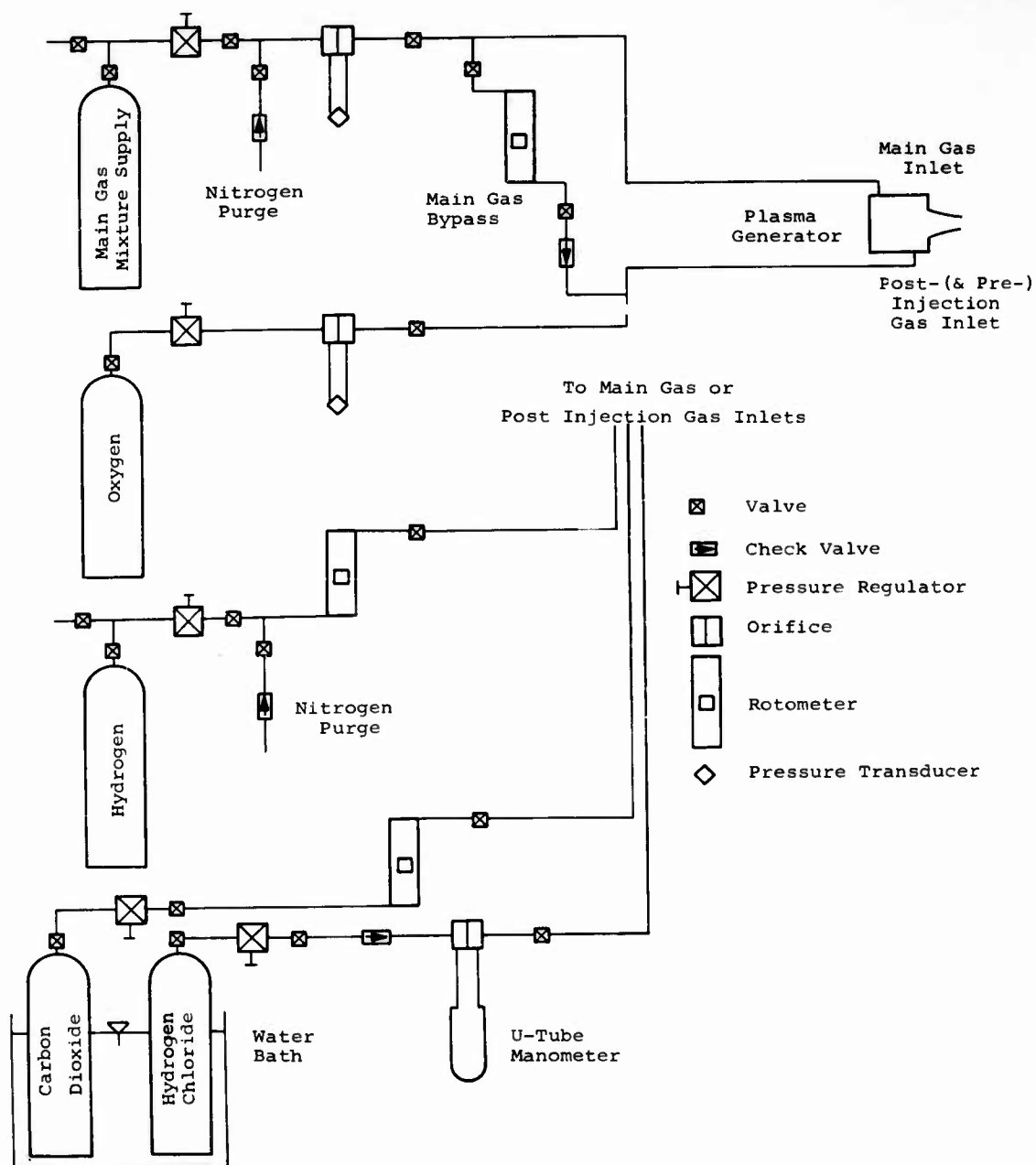


Figure 19.- Gas feed and metering systems.

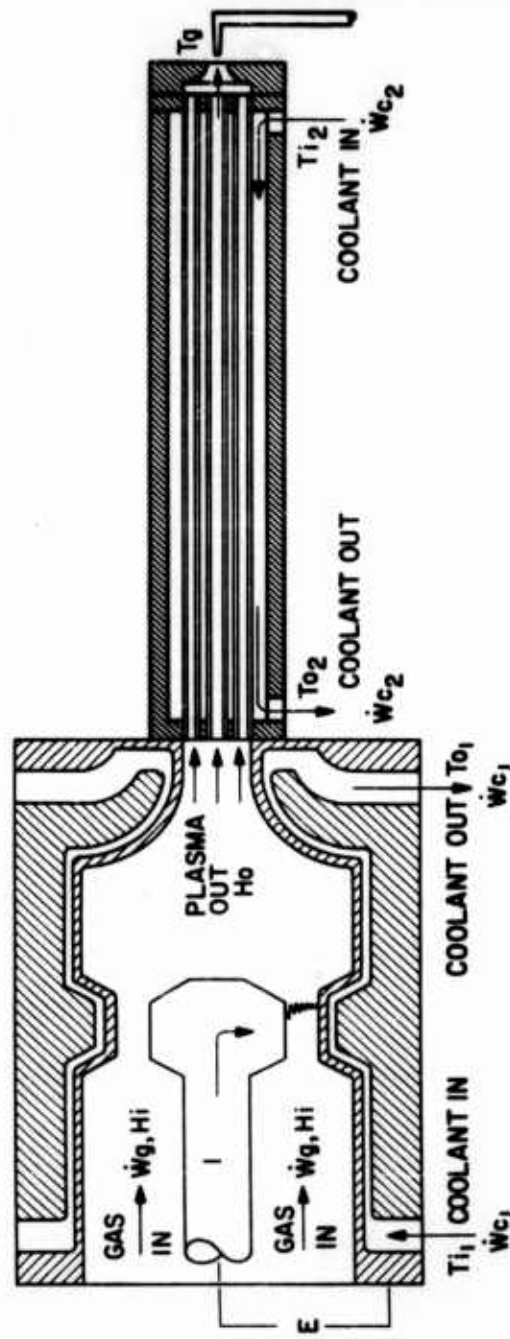


Figure 20.- Test setup for arc-plasma generator calibration.



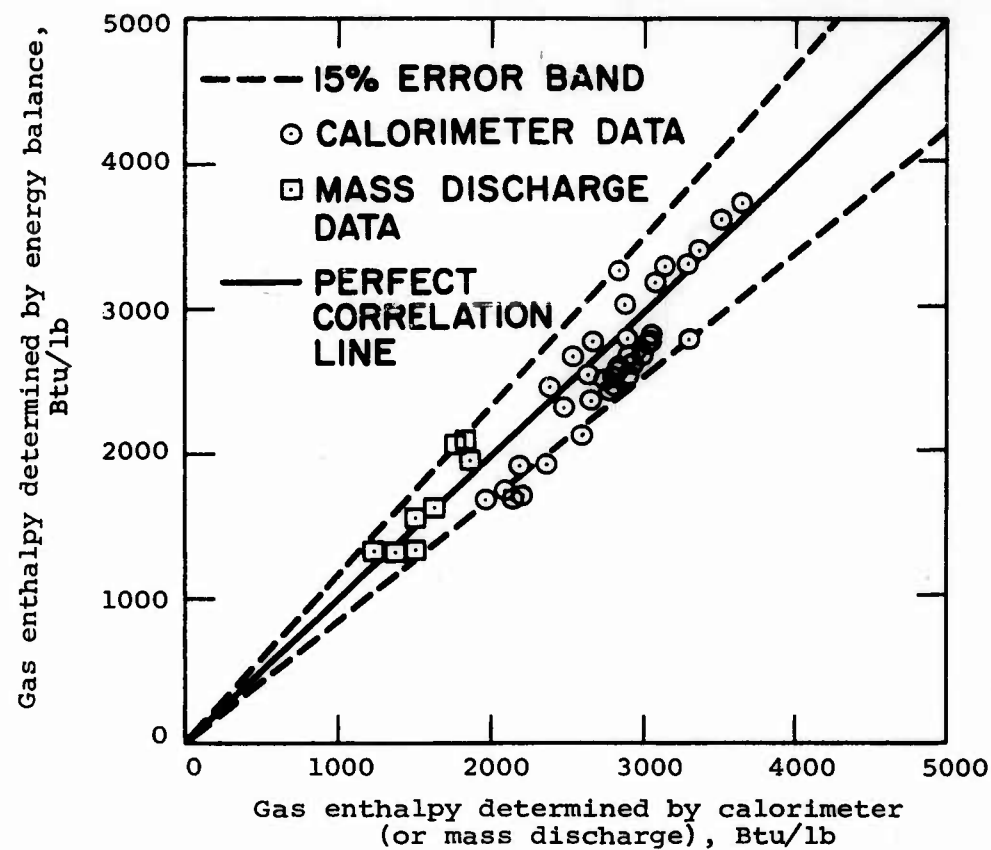


Figure 21.- Comparison of gas enthalpy by energy balance, calorimeter and mass discharge methods for nitrogen gas.

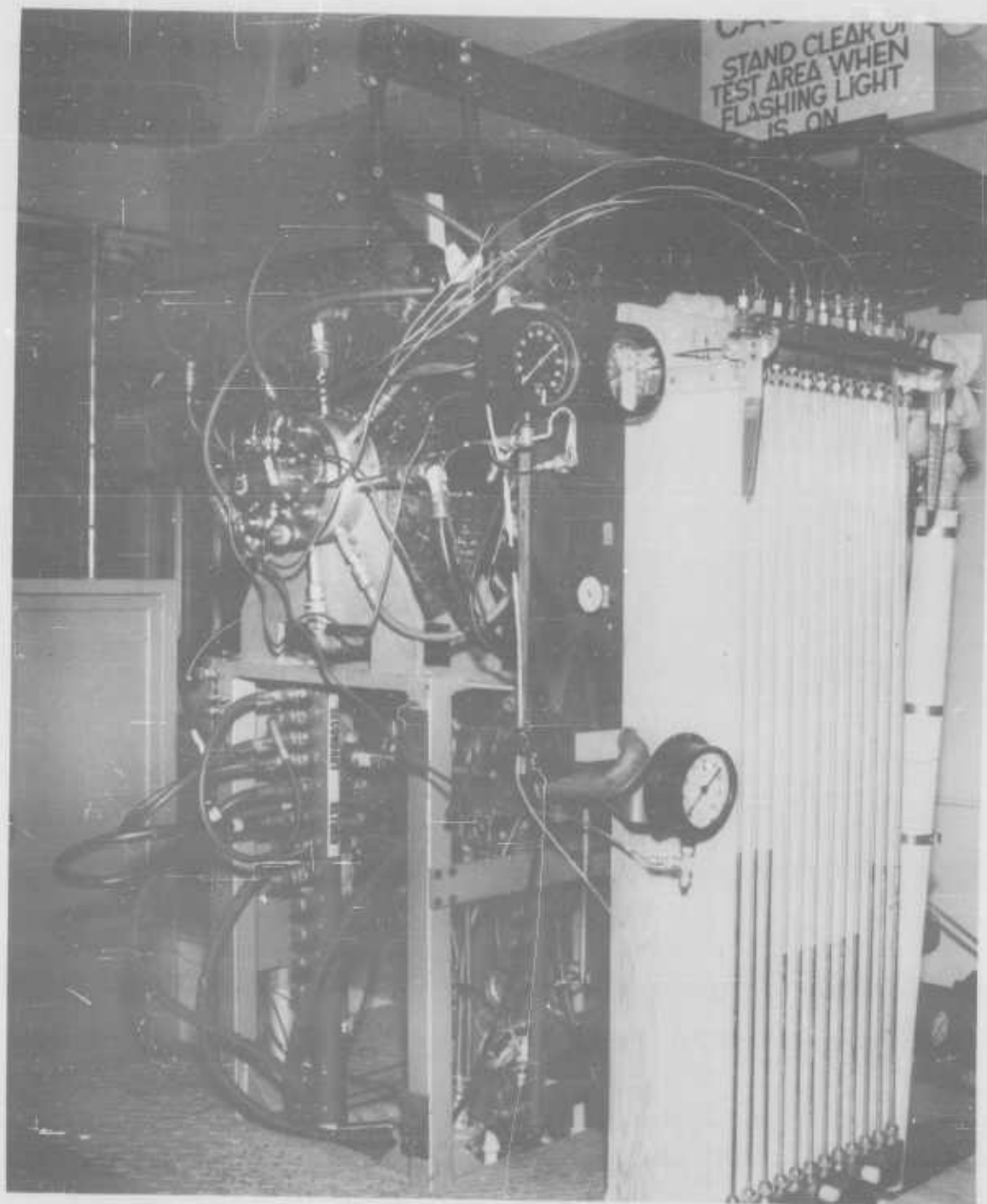


Figure 22.- Pressure distribution calibration test setup.

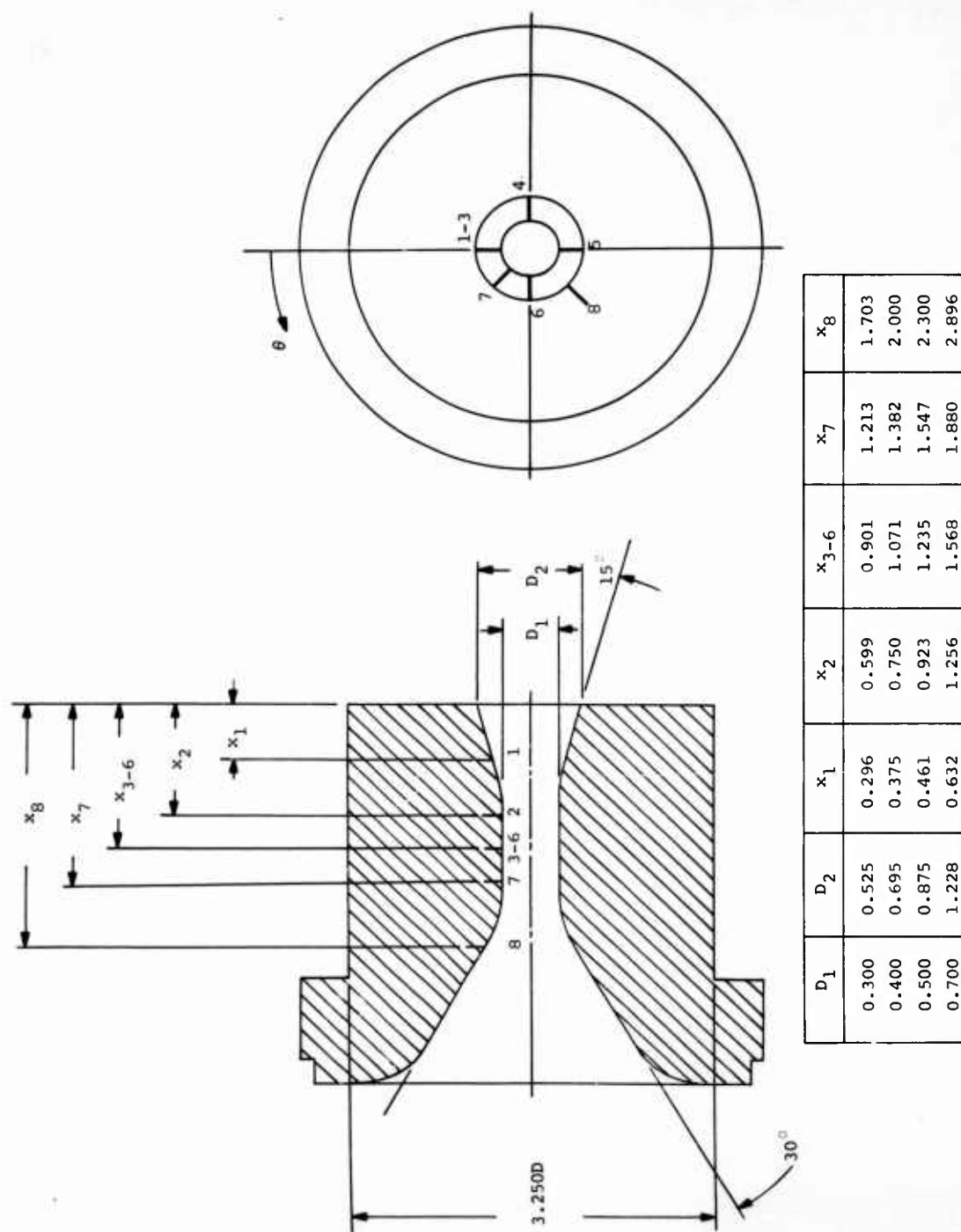


Figure 23.- Pressure-tap locations in calibration nozzles.



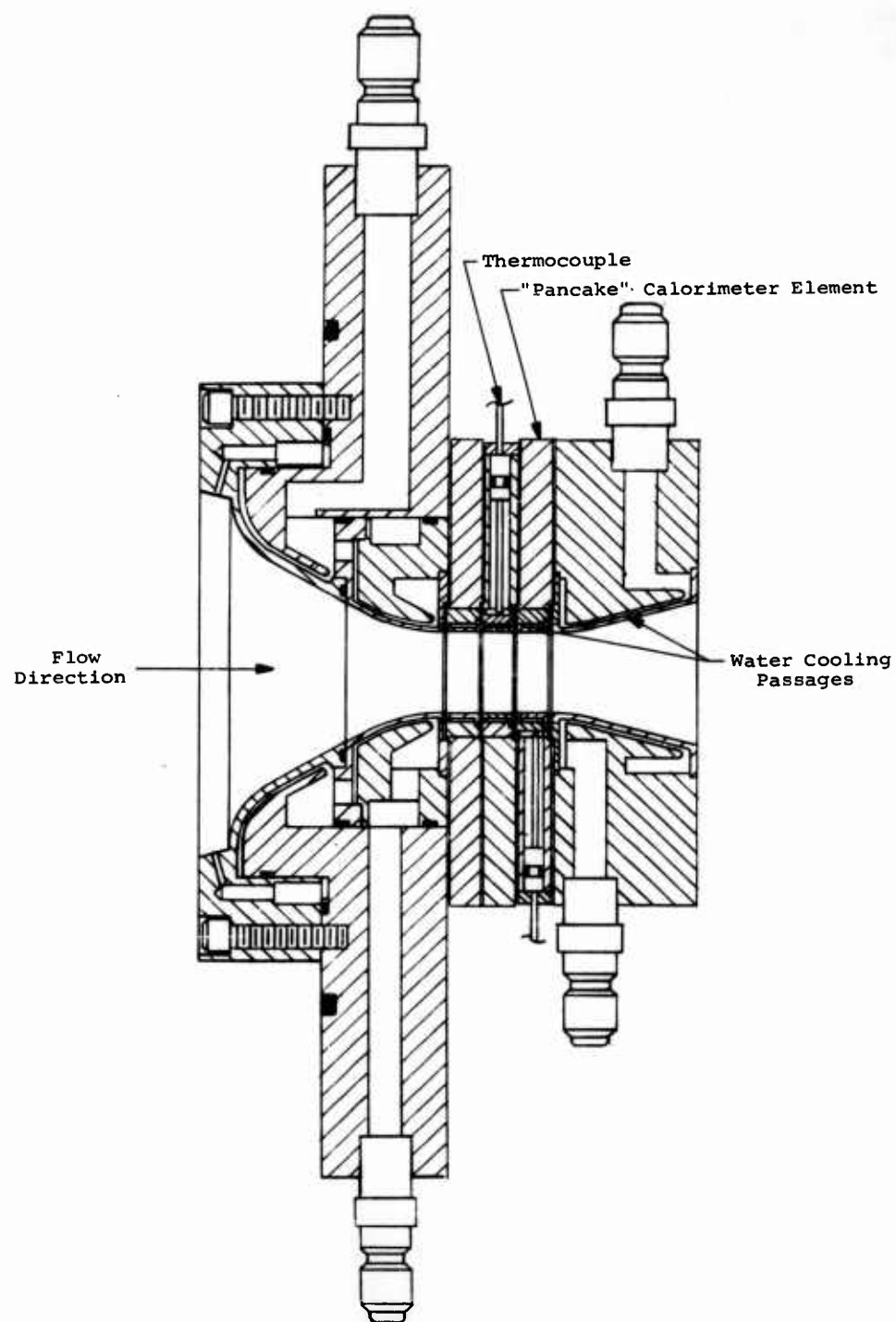


Figure 24.- Heat-transfer calibration nozzle.

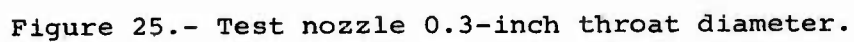


Figure 25.- Test nozzle 0.3-inch throat diameter.

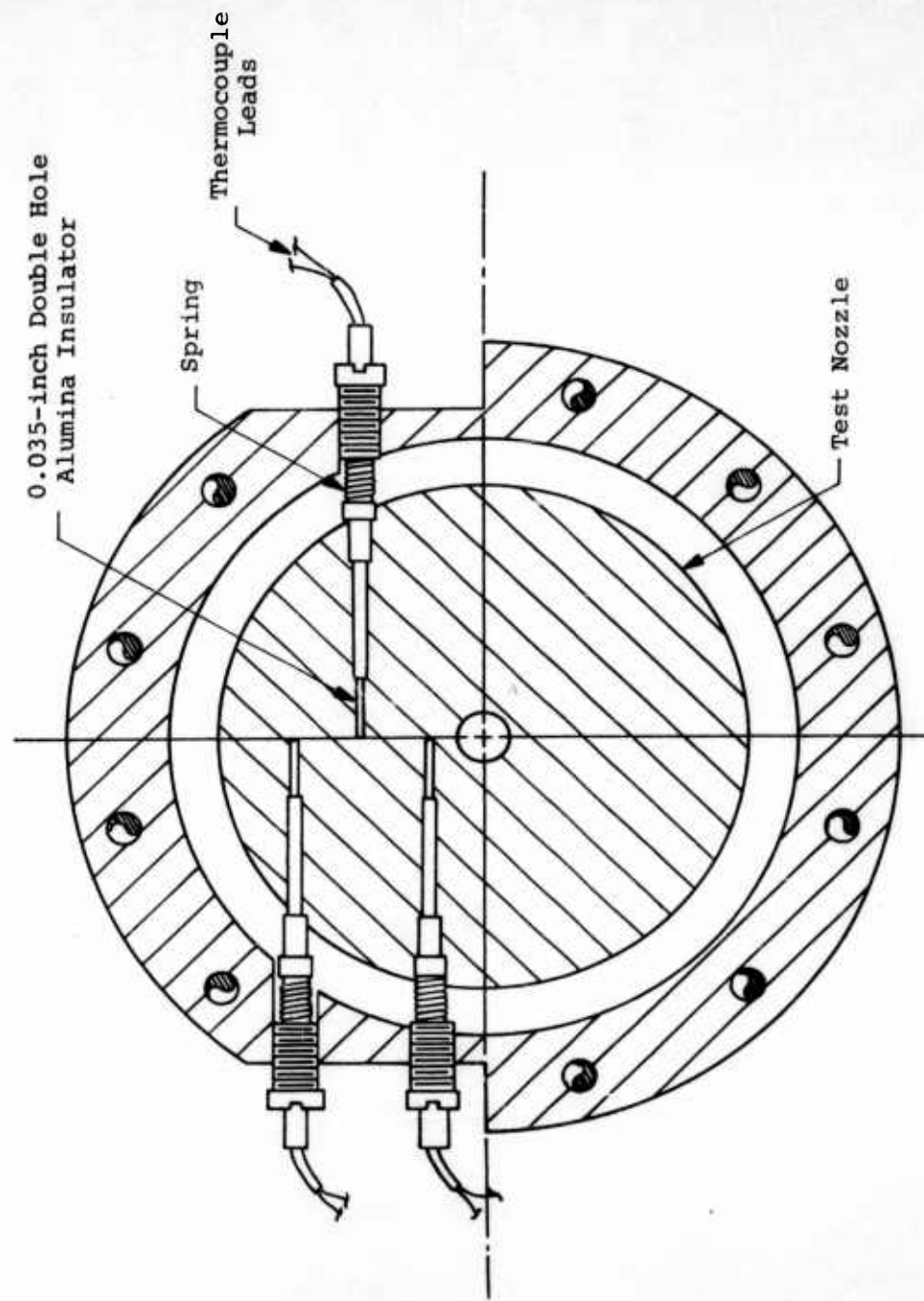


Figure 26.- Thermocouple installation in test nozzle.

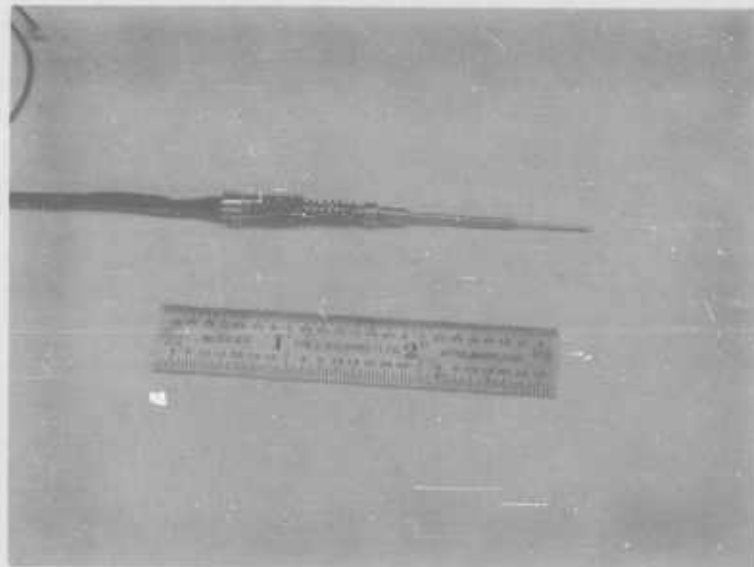
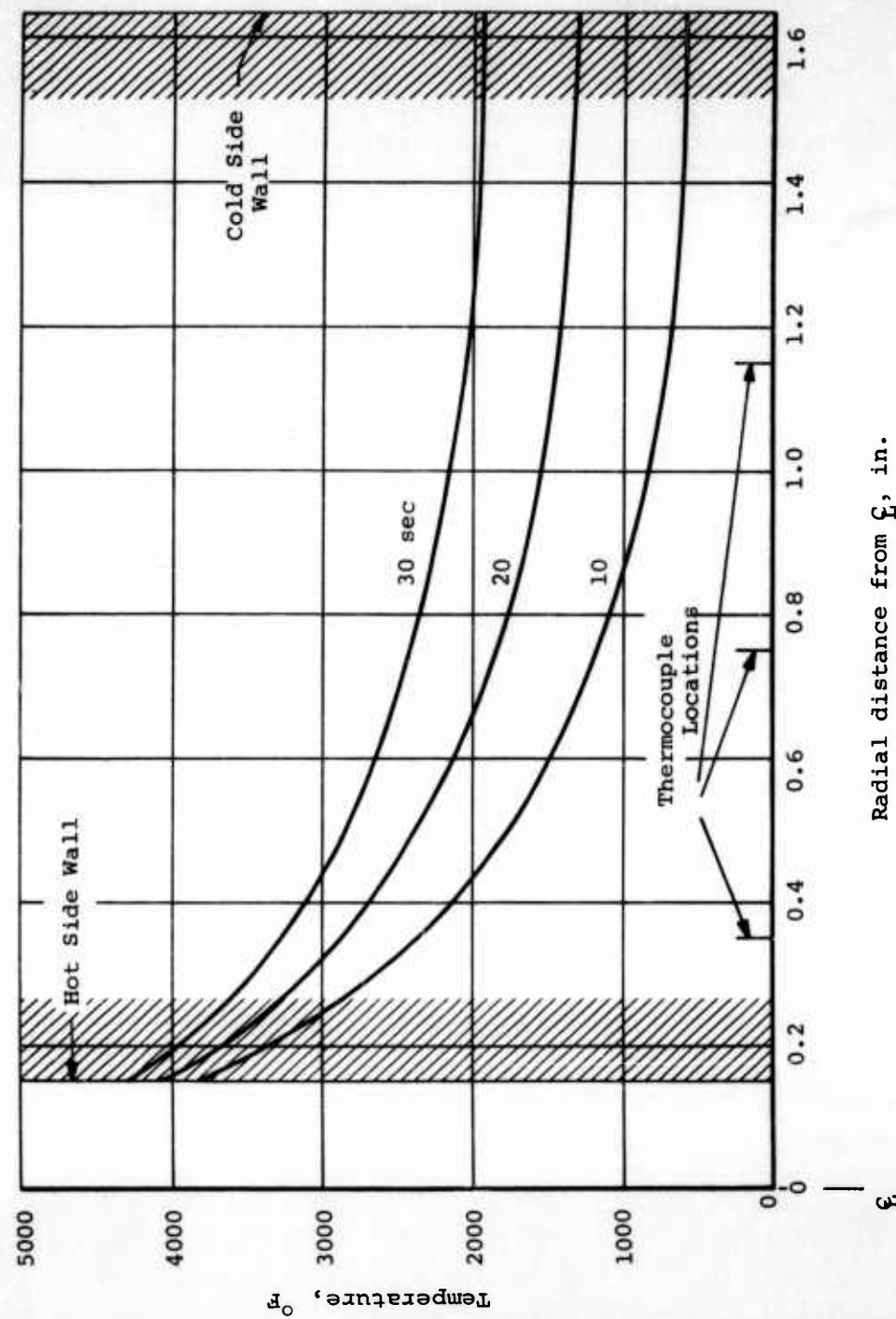
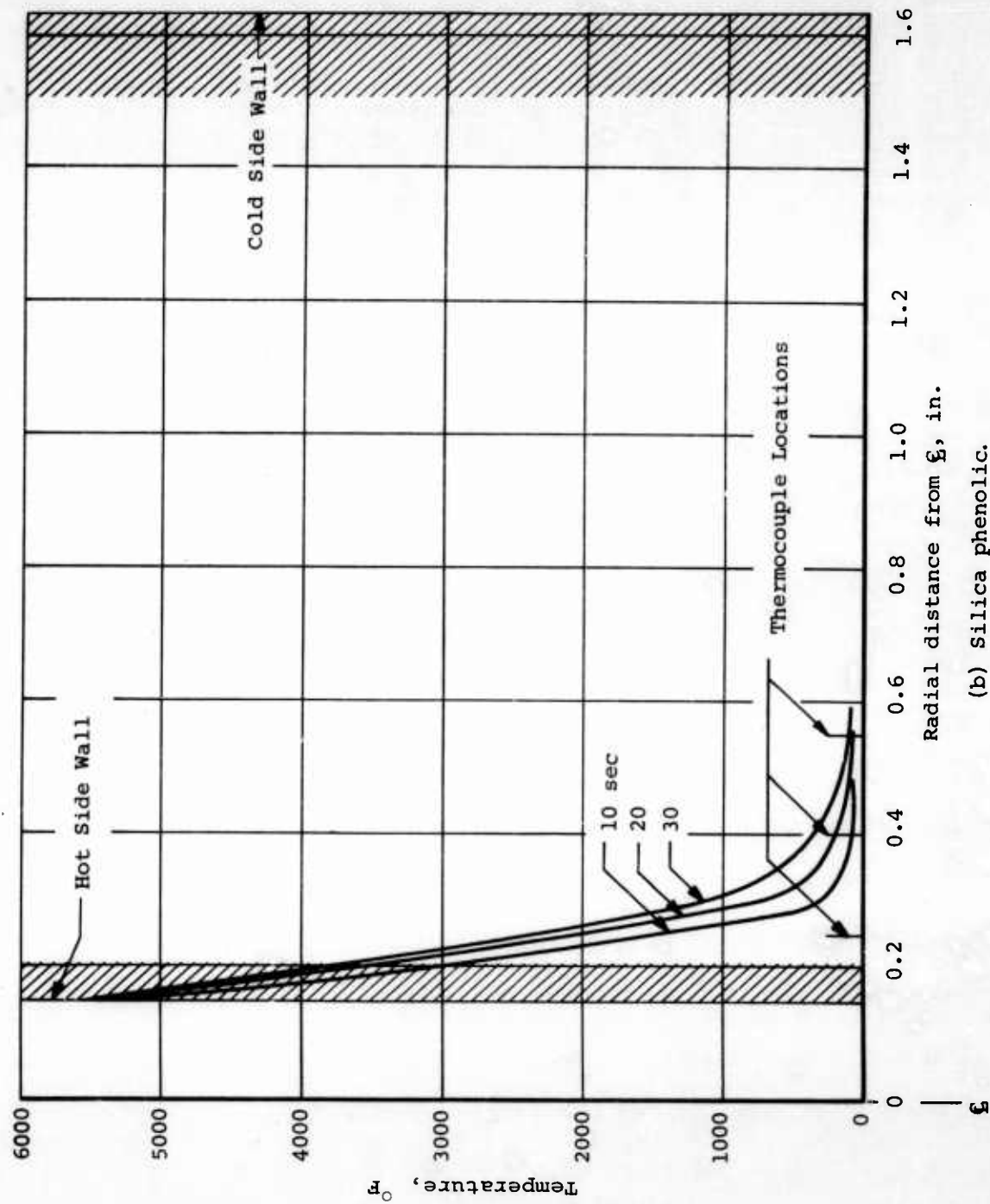


Figure 27.- Thermocouple probe.



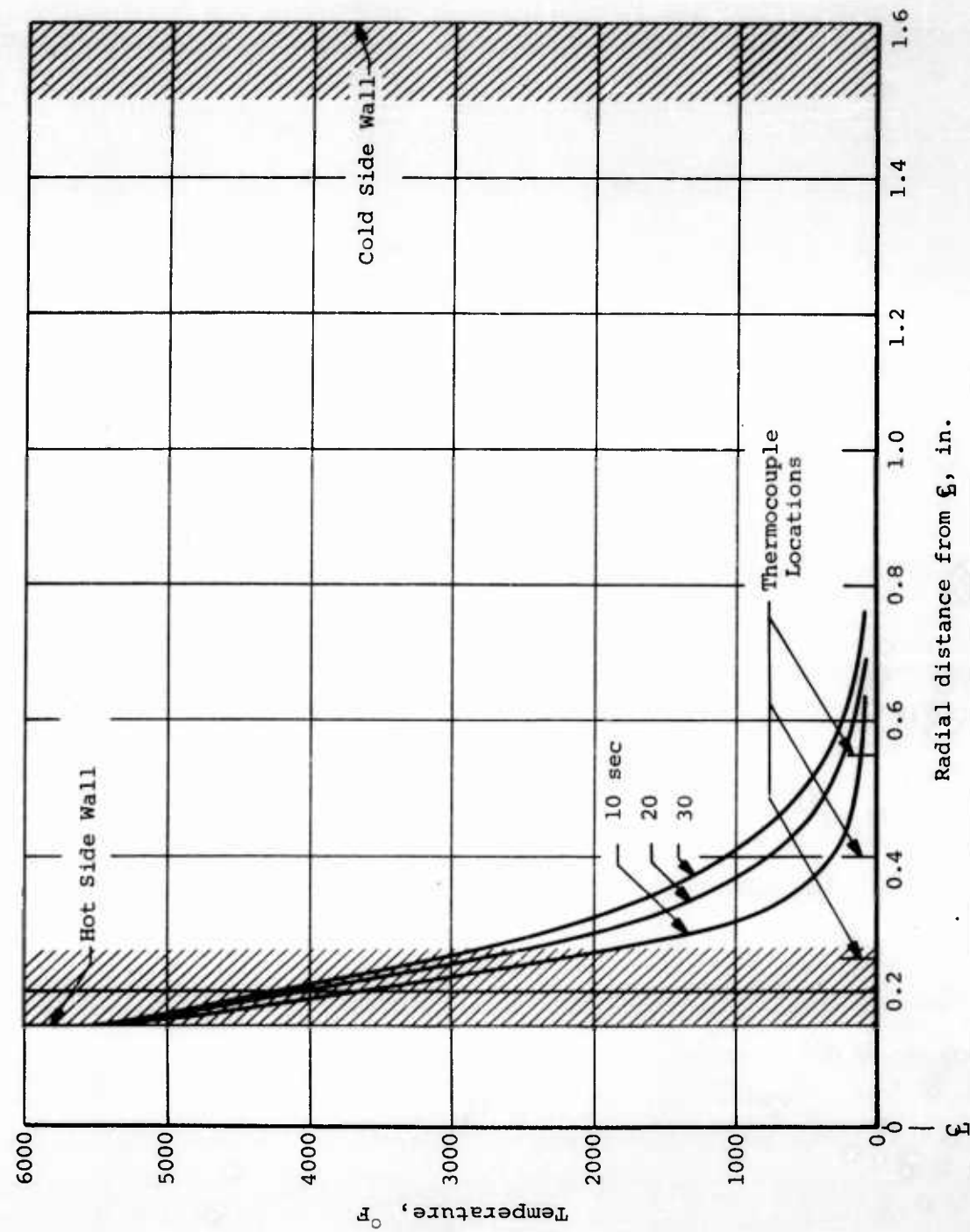
(a) Graphite.

Figure 28.- Thermocouple locations and analytic temperature distributions in test nozzles.



(b) Silica phenolic.

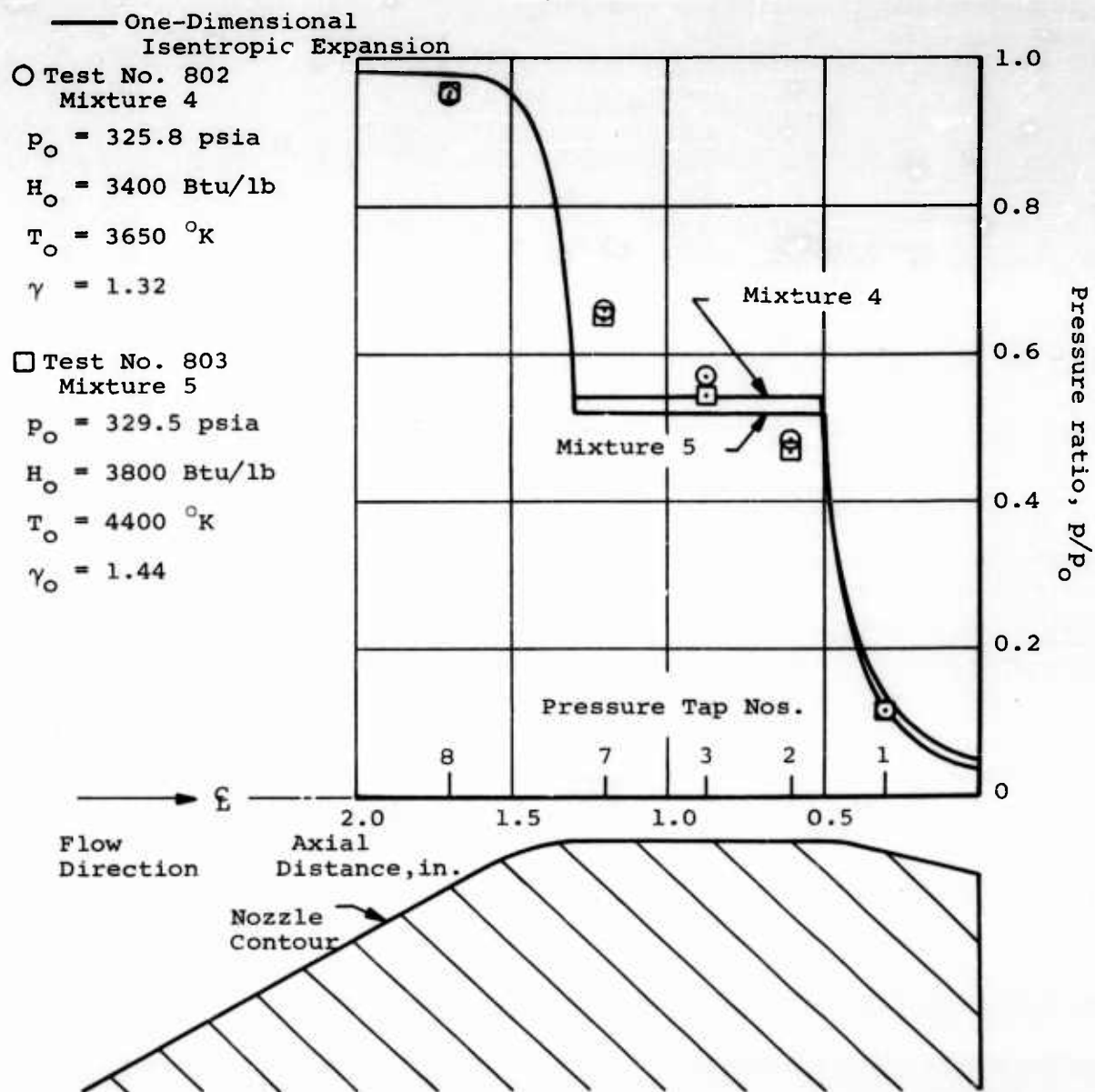
Figure 28.- Continued.



(c) Graphite phenolic

Figure 28.- Concluded.

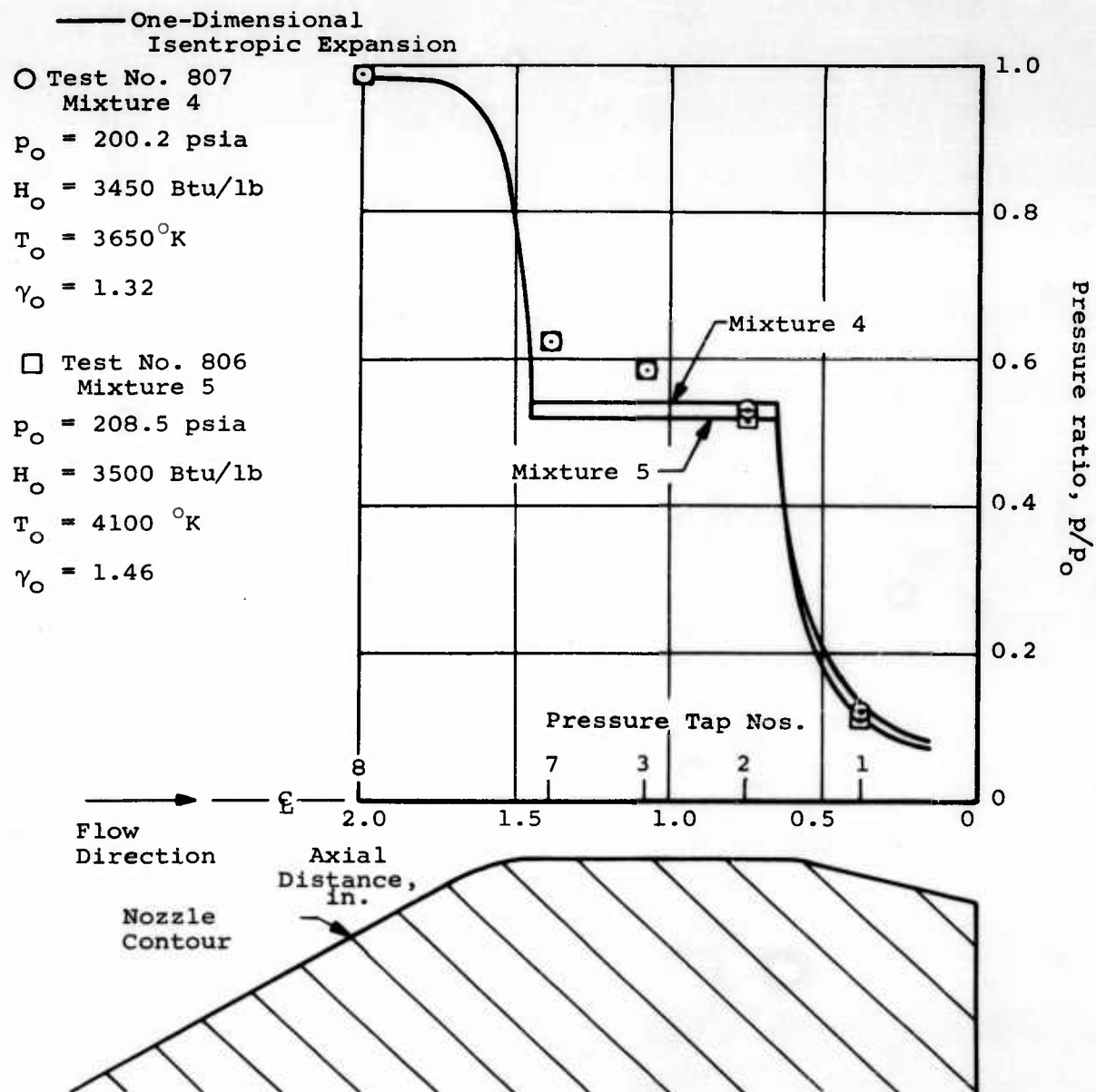




(a) 0.3-inch-diameter throat.

Figure 29.- Pressure distribution test results.





(b) 0.4-inch-diameter throat.

Figure 29.- Concluded.

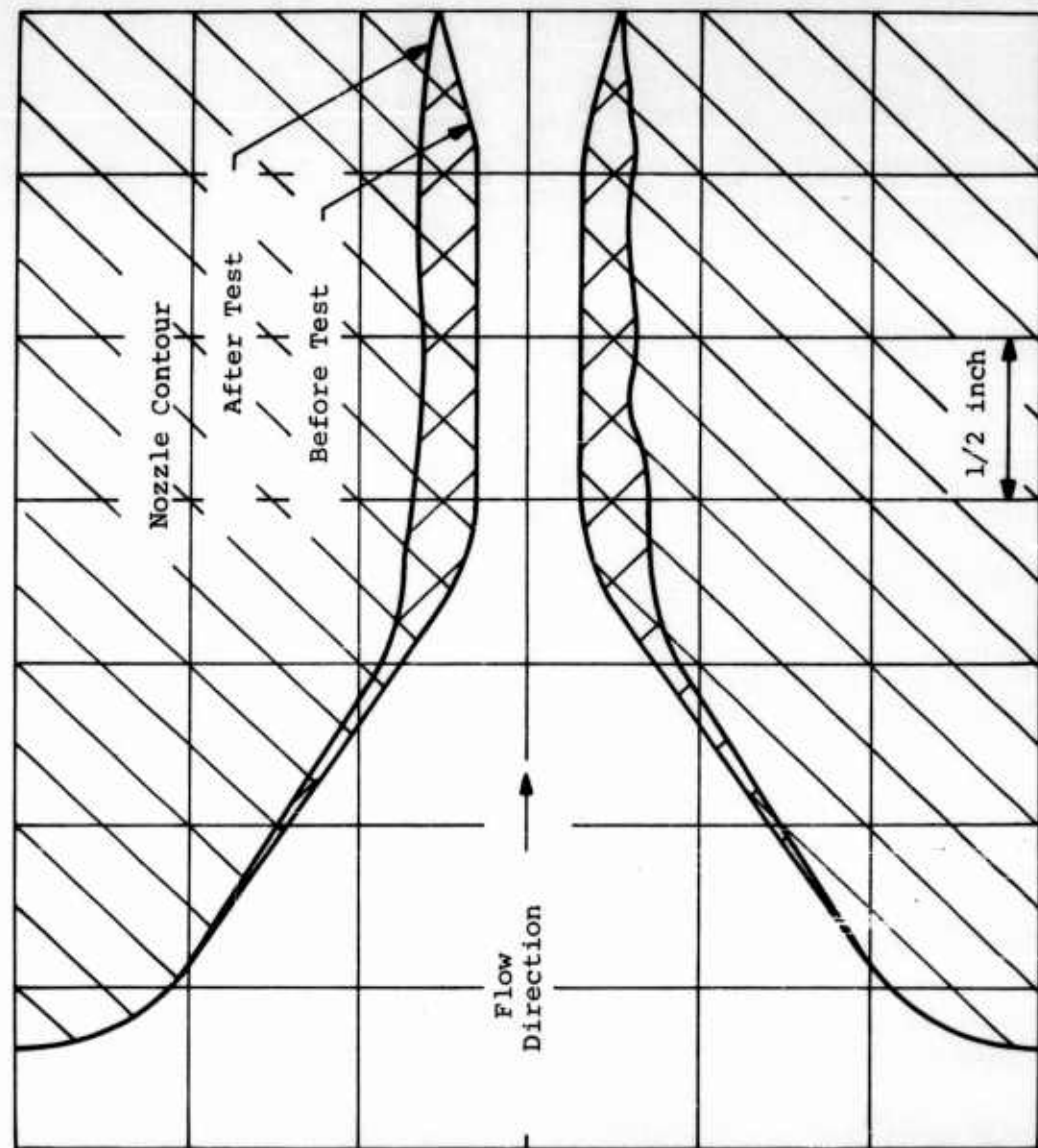
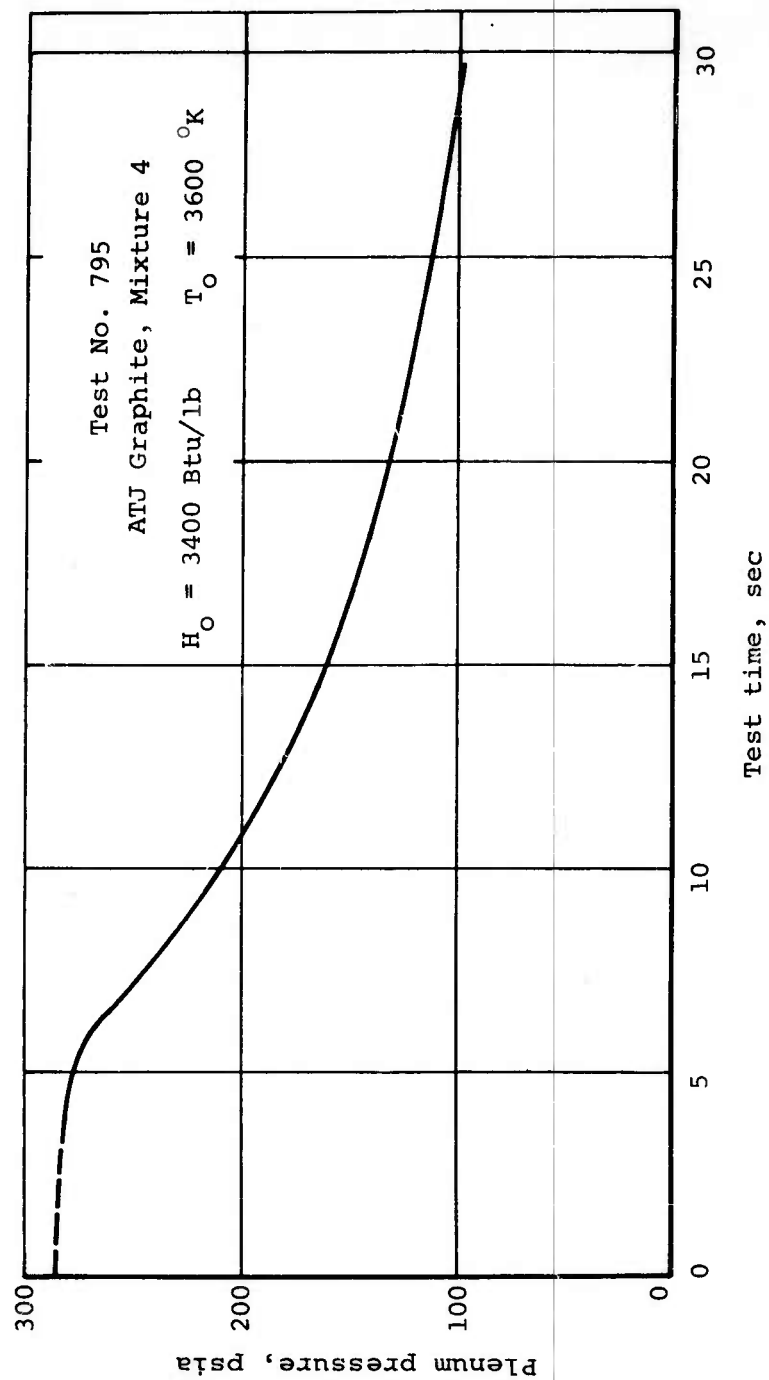
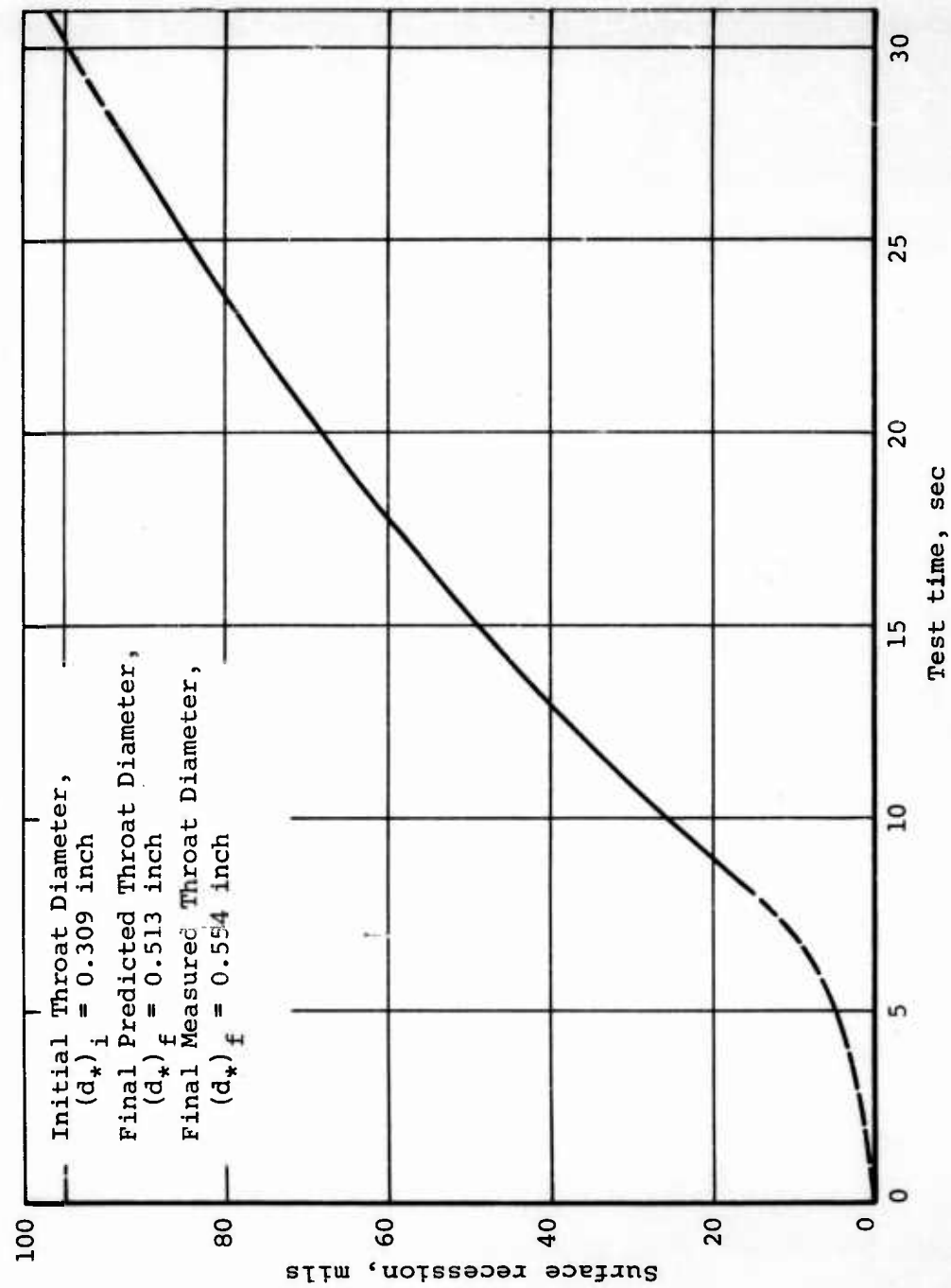


Figure 30.- Pre- and post-test wall profile; Test No. 795.



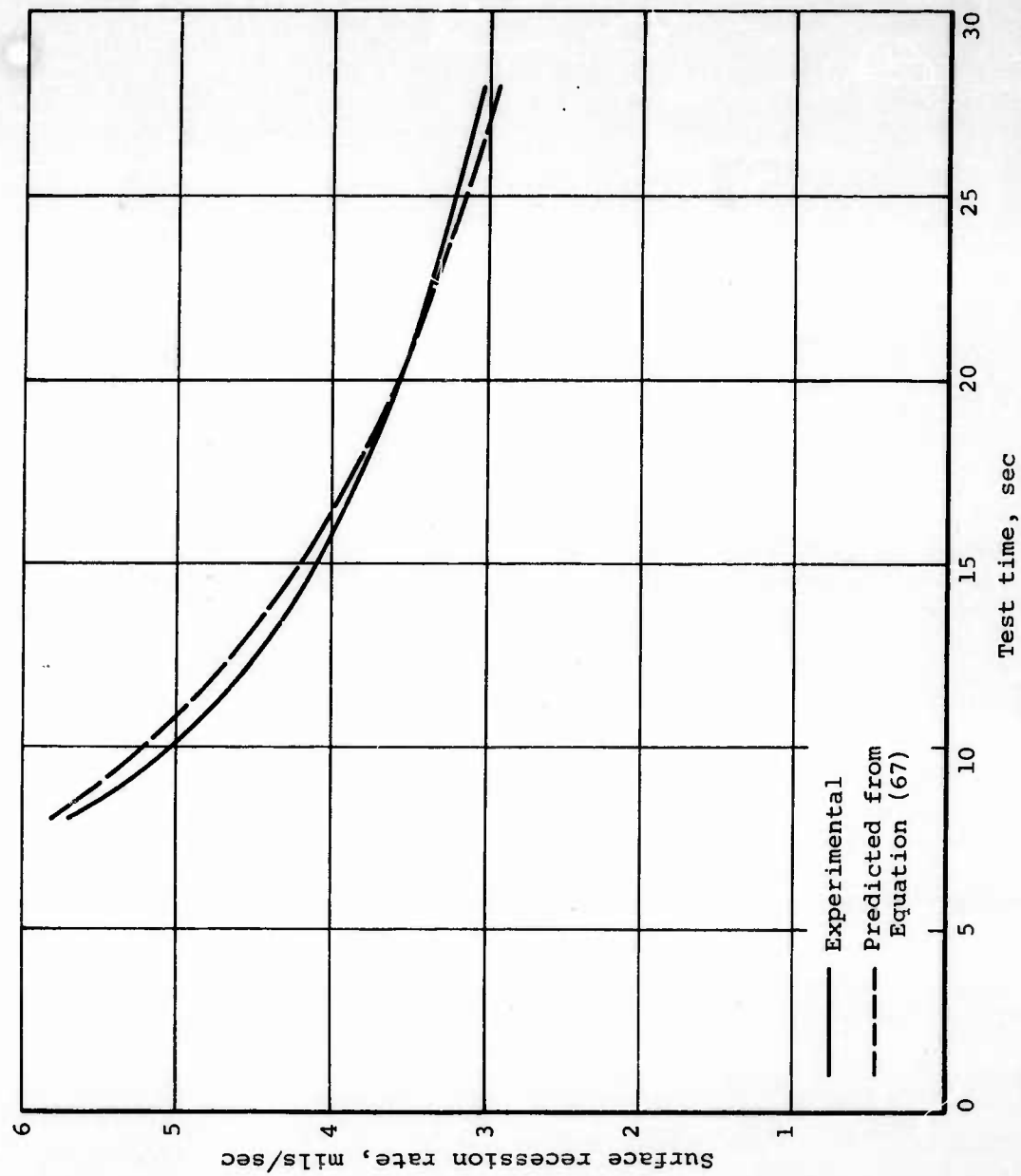
(a) Plenum pressure.

Figure 31.- Surface recession as determined from plenum pressure;  
 Test No. 795.



(b) Surface recession.

Figure 31.- Continued.



(c) Surface recession rate.

Figure 31.- Concluded.

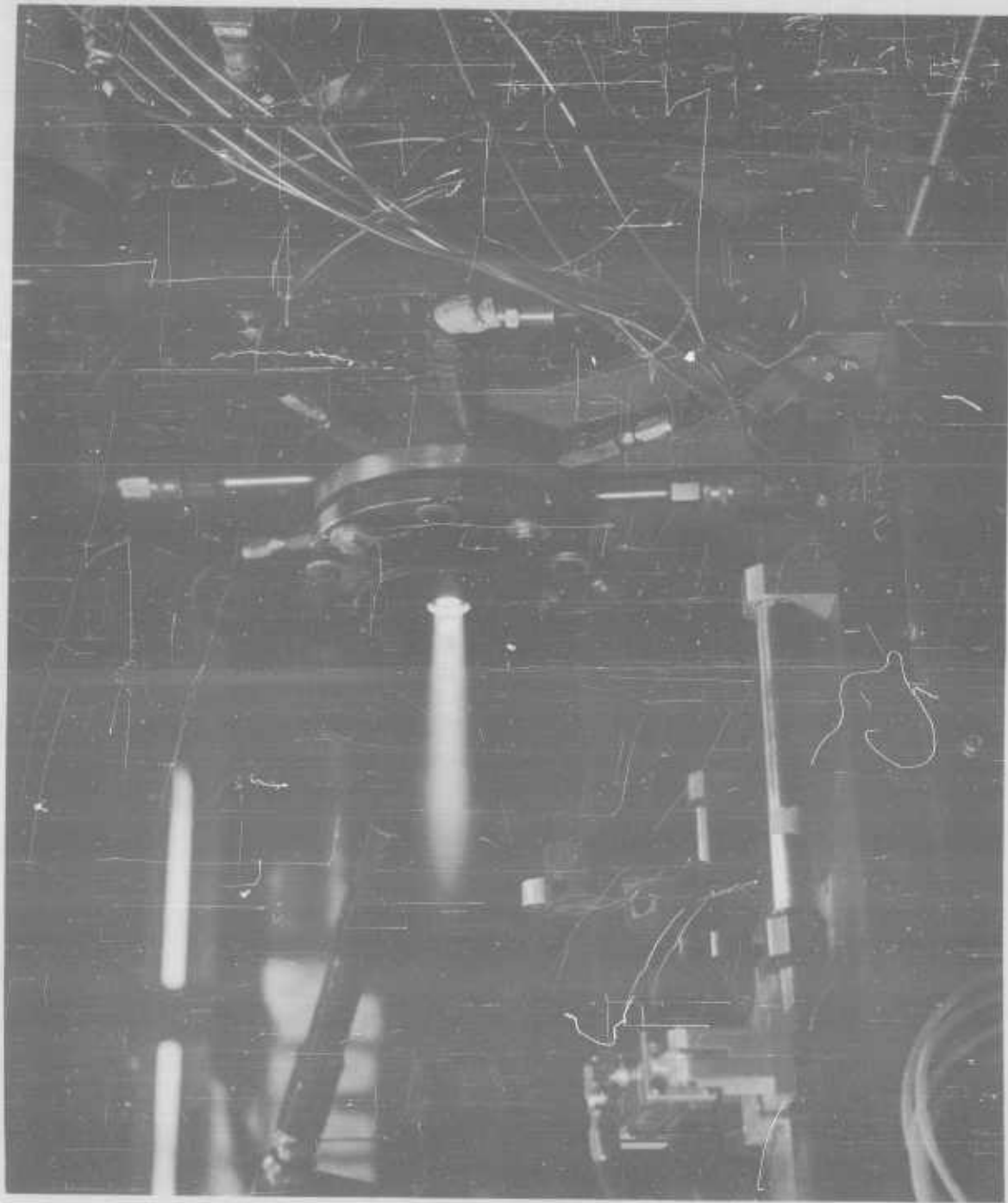


Figure 32.- Nozzle firing, ARJ graphite; Test No. 795.

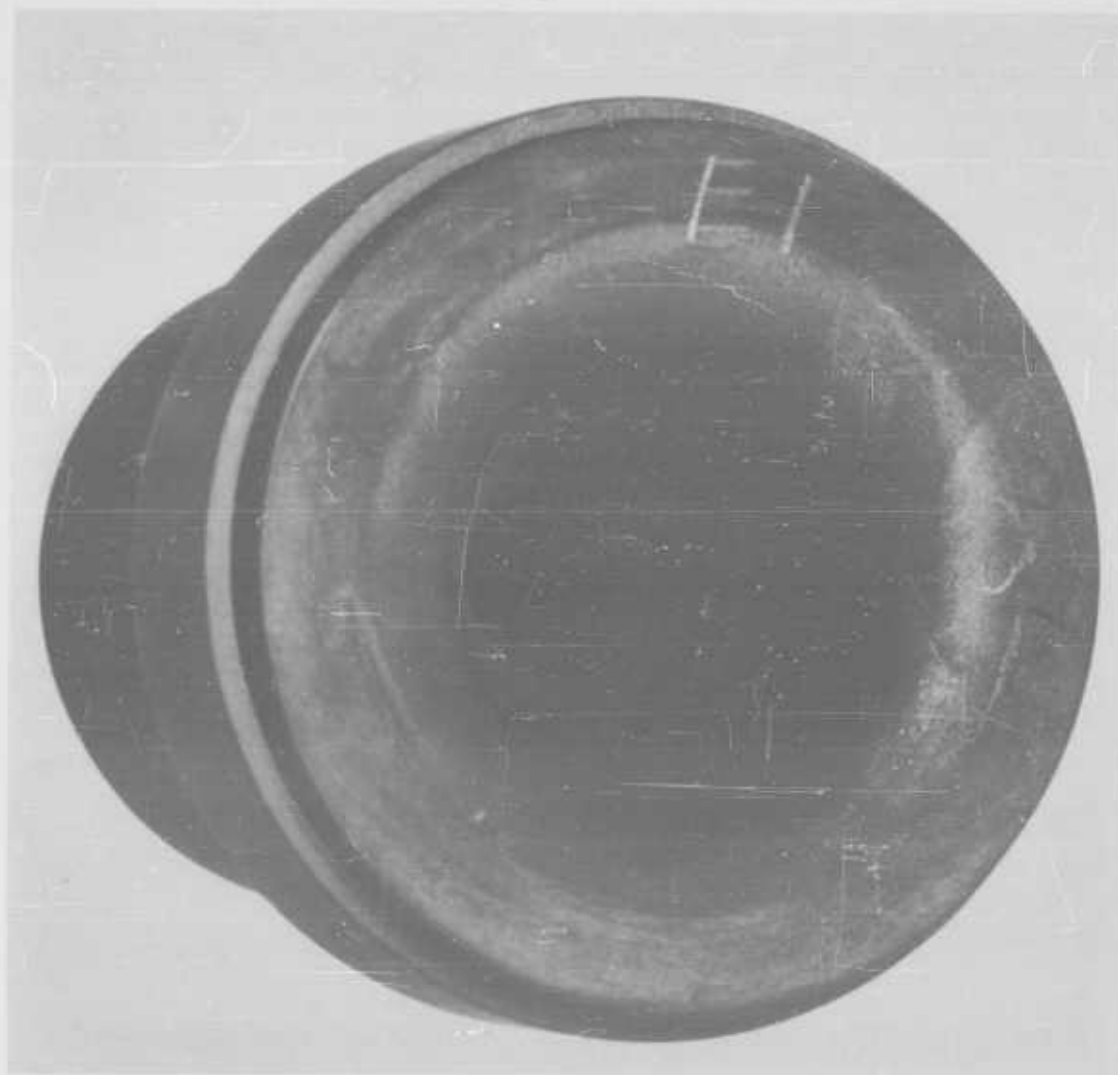


Figure 33.- Test nozzle after firing, ATJ graphite; Test No. 795.

## APPENDIX A

### DISCUSSION OF A STABILITY CRITERION FOR THE FINITE DIFFERENCE FORMULATION OF THE HEAT EQUATION

It is stated on page 35 that "the general condition of stability requires that the coefficient on  $T_1$  appearing in Equation (59a) be positive." This statement requires some discussion, and such is provided in this appendix. The general condition of stability to which reference is made applies to the explicit finite difference formulation of the heat equation. It is simply stated as follows: "The present temperature of any node must depend on the past temperature of that node in a non-negative sense." Thus, in Equation (59a), the coefficient of  $T_1$  must be positive (or zero).

The authors have seen no mathematical proof of this "general condition," but rather arrived at it by a heuristic argument made by Schneider (Ref. 18), and have developed confidence in it through successful application during the past several years.

It has been found extremely useful for determining allowable time increments for problems complicated by such things as geometry, chemical reactions, and convection (at the surface or in depth, as through a char). In the simple case of one-dimensional conduction, this requirement leads to the familiar criterion that

$$\frac{\alpha \Delta \theta}{(\Delta x)^2} \leq \frac{1}{2}$$

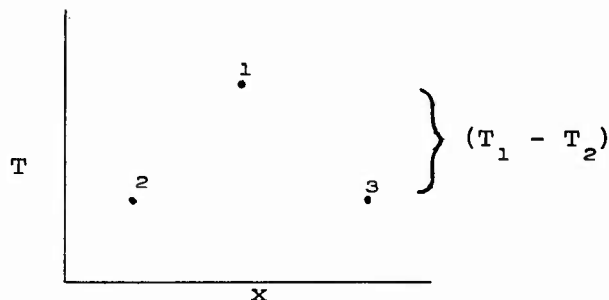
and this criterion has received mathematical proof (see Refs. 18 and 28).

A plausibility argument for the general condition of stability which the authors find of some satisfaction is presented below. Admittedly, it says nothing about convergence or stability of the finite difference solution per se, but rather is based on the criterion that the formulation satisfy the Second Law of Thermodynamics,



and thus, in this sense, be "reasonable." We can only defer to its successful use to relate the result to stability of the solution.

Consider a simple one-dimensional body with the temperature distribution shown in the sketch below at time  $\theta$ .



The customary explicit formulation expression for the temperature at node 1 at time  $\theta + \Delta\theta$  is

$$T_1' = m \left[ T_2 + T_3 + \left( \frac{1}{m} - 2 \right) T_1 \right] \quad (\text{A-1})$$

where

$$m \equiv \frac{\alpha \Delta\theta}{(\Delta x)^2}$$

For simplicity we have specified  $T_2 = T_3$ , so

$$T_1' = m \left[ 2T_2 + \left( \frac{1}{m} - 2 \right) T_1 \right] \quad (\text{A-2})$$

Rearranging,

$$T_1' = T_1 - 2m (T_1 - T_2) \quad (\text{A-3})$$

### A-3

Consider now the three possible cases for  $m$ .

$$(a) \quad \left( \frac{1}{m} - 2 \right) > 0$$

In this case,  $m < 1/2$ , and from Equation (A-3) and examination of the sketch we have:

$$T_1' < T_1 \quad \text{and} \quad T_1' > T_2$$

$$(b) \quad \left( \frac{1}{m} - 2 \right) = 0$$

Here,  $m = 1/2$ , and  $T_1' < T_1$ , and  $T_1' = T_2$

$$(c) \quad \left( \frac{1}{m} - 2 \right) < 0$$

Here,  $m > 1/2$ , and  $T_1' < T_1$  and  $T_1' < T_2$

Now for  $T_1' < T_2$ , energy must be transferred from node 1 to nodes 2 and 3 at a higher temperature. Since this violates the Second Law of Thermodynamics, we conclude that it is unreasonable to specify  $(1/m - 2) < 0$ . And in fact, in practice, such specification leads to large oscillations with time in the calculated temperature of node 1.

# ERRATA TO FIRST QUARTERLY PROGRESS REPORT

- Page 6, line 6            The number 0 should be replaced by the words "30 percent above". . .
- Page 16,                The first sentence beginning on that page should read: "In theory, any value of  $\eta$  could be used, although . . ."
- Page 31,                The last two equations on the page should be:

$$k_2' = \frac{k_2}{\rho_e u_e C_M}$$

$$k_1' = \frac{k_1 p_s M_s}{M_{H_2O} \rho_e u_e C_M}$$

- Page 32,                The sentence beginning the last paragraph on the page should read: "The limiting case of  $k_1' = k_2' = 0$  has been calculated."
- Page 35,                The last sentence on that page should read: "Assuming an Arrhenius extrapolation of the data, that is, plotting the log of the coefficients versus  $1/T$ , yields at  $3000^\circ K$

$$\dot{m}_c \cong 0.1 \text{ moles carbon/min-cm}^2$$

which is of comparable magnitude to observed rates."

- Page 38,                The second sentence on the page should read: "Patch (Ref. 40) has studied the . . ."
- Page 39,                Credit for the derivation of the equation at the top of the page should be given to Dr. R. M. Kendall of the Vidya Staff. To the authors' knowledge this does not appear elsewhere in the literature.
- Page 64,                The first sentence below Table 3.6 should indicate the molecular weight as "11.92".
- Page 66,                The R/M term in Equation (62) should read as:

$$\left( \frac{M}{R} \right)^{1/2}$$

Page 67,

The tabulation at the bottom should read:

	<u>Simulated</u>	<u>Actual</u>
D*	1/2 inch	1 foot
M	18.60	20
$\gamma$	1.17	1.17

Page 68,

The equation at the top should read:

$$\frac{p_{o_{sim}}}{p_{o_{act}}} = 0.510$$

The second line after that expression should indicate "153 psia".

Page 70,

The equation should read:

$$\frac{a_{*_{sim}}}{a_{*_{act}}} = 1.075$$

The sentence following should read:

"For this case, the shear stress will be some 7.5 percent higher in the laboratory simulation than in the actual rocket situation."

The omitted page number in the first sentence of 'Summary' is page 55.

Inadvertently Table I was omitted from the First Quarterly Progress Report. For completeness, it is included here.

TABLE I.- GRAPHITE WALL EROSION WITH IMPINGING  
 $\text{Al}_2\text{O}_3$

Fuel	Percent by Mass	Oxidizer	Percent by Mass
$\text{C}_{6.884}\text{H}_{10.089}\text{N}_{0.264}\text{O}_{0.278}$	39.667	$\text{NH}_4\text{ClO}_4$	100
$\text{C}_{21}\text{H}_{24}\text{O}_2$	7.000 53.333	$\frac{\text{Mass Oxidizer}}{\text{Mass Fuel}} = 2.333$	

P (atm)	T (°K)	$\dot{B}$	$\dot{B}^*$
10.2	3500	0.2431	0.3498
	3000	.2564	.4093
	2000	.1574	.1995
	1500	.1046	.001
	1000	.003	0
15.5	3000	.2536	.4131
	2000	.1506	.1303
	1500	.1045	.001
	1000	0	0
20.4	3000	.2536	.4136
	2000	.1463	.1177
	1500	.1044	.001
	1000	0	0

# DISTRIBUTION

This report was distributed to the following groups:

	<u>No. of Copies</u>
Rocket Research Laboratories Attn: DGSCH Edwards, California	3
ASD (ASRCEE-1) Wright-Patterson Air Force Base, Ohio	1
ASD (ASRCNC) Wright-Patterson Air Force Base, Ohio	1
ASD (ASRCMC) Wright-Patterson Air Force Base Ohio	1
SSD (SSTRE/Mr. G. Peterson) Air Force Unit Post Office Los Angeles 45, California	1
Copies distributed in accordance with Category II of the June 1963 Chemical Propulsion Information Agency Mailing List	183